Advances in Instrumentation for Dynamic Nuclear Polarization & Magic-Angle Spinning NMR

by

Daniel P. Banks

B. S. Chemistry
Pennsylvania State University, 2014

Submitted to the Department of Chemistry
in partial fulfillment of the requirements for the degree of
Doctor of Philosophy

at the

MASSACHUSETTS INSTITUTE OF TECHNOLOGY

June 2021

Author .....
Department of Chemistry
May 13, 2021

Certified by.....
Robert G. Griffin
Arthur Amos Noyes Professor of Chemistry
Thesis Supervisor

Accepted by.....
Adam P. Willard
Associate Professor of Chemistry
Graduate Officer

This doctoral thesis has been examined by a Committee of the
Department of Chemistry as follows:

Professor Moungi Bawendi .....
Chairman, Thesis Committee
Lester Wolfe Professor of Chemistry

Professor Robert Griffin.....
Thesis Supervisor
Arthur Amos Noyes Professor of Chemistry

Professor Keith Nelson .....
Member, Thesis Committee
Haslam and Dewey Professor of Chemistry

Advances in Instrumentation for Dynamic Nuclear Polarization & Magic-Angle Spinning NMR

by

Daniel P. Banks

Submitted to the Department of Chemistry
on May 13, 2021 in partial fulfillment of the
requirements for the degree of
Doctor of Philosophy in Chemistry

Abstract

Dynamic nuclear polarization (DNP) is an invaluable tool for increasing the sensitivity of magic angle spinning (MAS) nuclear magnetic resonance (NMR) experiments. Historically, one of the primary drawbacks of DNP has been limited spectral resolution. The resolution of DNP spectra can be substantially improved via data acquisition at higher magnetic fields as well as faster MAS and increased experiment dimensions. However, achieving the maximum possible sensitivity and resolution in MAS DNP experiments is significantly limited by the equipment that is currently available. In this thesis I discuss new designs and fabrication methods for constructing instrumentation for DNP and MAS NMR with an emphasis on designing and fabricating equipment to enable ultra-fast MAS DNP experiments.

This thesis covers several topics including 3D printing stators for MAS experiments, the design of a balanced transmission line DNP probe for ^{17}O experiments, the design of a helium recirculation system, and the fabrication of CVD diamond rotors for MAS DNP experiments. These projects are intended to increase the capabilities of MAS DNP equipment, leading to improved spectral sensitivity and resolution. The balanced transmission line probe design is compatible with a helium recirculation system and includes a new 1 mm stator design that should achieve MAS frequencies greater than 80 kHz at 100 K. At these spinning frequencies it will be possible to perform ^{1}H-detected DNP experiments that will not only provide access to an additional set of biological structural information, but also significantly improve the sensitivity of experiments over traditional ^{13}C detection. The development of diamond MAS rotors is expected to increase the sensitivity and resolution of MAS DNP experiments even further via higher DNP enhancements and faster MAS.

Additional studies are presented on the amyloidogenic peptide GNNQQNY, which is used as a model system for ^{17}O bound water studies and amyloid polymorphism. The aforementioned equipment will be used to perform ^{1}H-detected HON experiments on GNNQQNY to directly probe the hydrogen bonds present in the system. These studies will serve as a framework for future multidimensional ^{17}O studies on complex biological systems.

Thesis Supervisor: Robert G. Griffin
Title: Arthur Amos Noyes Professor of Chemistry

Acknowledgements

This thesis would not have been possible without the amazing support I've received from so many wonderful people. In this section I would like to take time to recognize those people that were especially instrumental in the completion of this work.

I would like to start by thanking the members of my thesis committee. To my thesis advisor, Bob Griffin, thank you for giving me the opportunity to work on so many interesting projects as well as all of the support you provided me with along the way. You always pushed me to be the best scientist I could be and for that I am forever grateful. To my thesis chair, Moungi Bawendi, I would like to say thank you for all the guidance and support you provided to me as well as the helpful career discussions we've had the last few years. Last but not least I'd like to thank Keith Nelson who, in addition to serving on my thesis committee, I had the privilege of teaching with as a 5.112 TA. Keith, I always enjoyed our discussions on science and your enthusiasm was always contagious.

To my fellow "Griffindors" I owe all of you a huge thank you. The support I have received from all of you gave me the strength to continue pushing forward no matter how daunting the challenge was. I'd especially like to thank a few of you that I've had the opportunity to work closely with during my time at MIT. To my fellow graduate students Brian Michael, Natalie Golota, Salima Bahri and Eric Keeler, thank you for the privilege of working alongside you and for the friendships we formed along the way. To my postdoc mentors Vlad Michaelis, Mike Colvin, Robert Silvers, Kong Tan, Christy George, Kevin Donovan, and Zhiwei Chang, thank you for all of the amazing guidance you provided me, both in science and in life. I would like to thank our technicians and research staff, Ajay Thakkar, Michael Mullins, Stephen Thomson, and David Ruben for all of their help maintaining the lab's equipment and for many helpful discussions. I would especially like to thank Ajay Thakkar, who taught me so much of what I know about NMR probes and electronics. To each member of the group, both former and present, I will never forget the amazing memories we've shared and the fellowship that we formed.

In addition to my colleagues in the Griffin Group I have also had the opportunity to work with many wonderful collaborators. I would like to start by thanking our PSFC colleagues, Rick Temkin and Sudheer Jawla, for all of their help operating and maintaining the DNP equipment and for many fruitful scientific discussions. Sudheer, I would especially like to thank you for all of your help with our collaborations the last few years. To my collaborators at the Center for Bits & Atoms, it has been a privilege to have had the opportunity to work with all of you. I want to say thank you to Neil Gershenfeld for opening up his lab to us and helping make the diamond rotor project a reality. To my fellow CBA collaborators Zach Fredin, Prashant Patil, Will Langford, and Camron Blackburn, thank you for everything you have put into the diamond project. A project that was once thought to be impossible becomes more of a reality every day thanks to your hard work.

None of this work would have been possible had it not been for my amazing family and friends. To Sam, Julia, Brian, Katie, Jay, Nathan, Seokjoon and Alex, thank you for your incredible support and the wonderful memories we have made. I would not have accomplished this without all of you. To my in-laws Dr. A. Randall Moody, Sharon Moody and Danielle, thank you for welcoming me into your family and for always showing me the meaning of southern hospitality. I

always love our visits to Texas and look forward to many more in the years to come. To my parents John and Robin, my brother Adam, and my sister Sarah, thank you for always supporting me and for always being there for me. I would especially like to thank my parents for encouraging my interest in science at an early age and for always pushing me to be the best I could be. From buying me books on space and dinosaurs when I was a kid to always encouraging me to purse my dreams, I am forever grateful for everything you have done for me. Mom and Dad, I love you both very much and I would not be where I am today if it were not for you.

Finally, I'd like to say thank you to my wife, Nicole. Nicole, I'm not even sure where to begin as I don't think I would be writing this thesis if it weren't for you. Throughout all my struggles you have always been there to love and support me, even during my most ridiculous moments. I never thought passing out 5.112 notes before class could be the highlight of my day and I certainly didn't think it would lead to the highlight of my life. Nicole, you are my rock, my best friend, and the motivation that always keeps me going. I love you so much and I am eternally grateful that you are part of my life. This thesis is dedicated to you.

Table of Contents

List of Figures

List of Tables

1 Introduction

1.1 Nuclear Magnetic Resonance

1.1.1 Historical Overview of NMR

Nuclear magnetic resonance (NMR) is a physical phenomenon that arises due to the interactions of a nuclear magnetic moment with an external magnetic field. The first experimental observation of this phenomenon was recorded by Isidor Rabi in 1938.[1] Using a modified version of the Stern-Gerlach experiment,[2] Rabi noticed a change in the orientation of the nuclear magnetic moment of Li atoms when a molecular beam of LiCl was subjected to an oscillating magnetic field. This change in orientation occurred when the oscillating magnetic field was applied perpendicular to a strong, constant magnetic field and was only observed when the frequency of the applied radiofrequency (RF) field approached the Larmor frequency of the Li atoms. Thus, the reorientation of the nucleus' magnetic moment occurred when the applied RF field was in resonance with the Larmor frequency of the nucleus. Using this method, Rabi was able to measure the magnetic moments of Li isotopes to a remarkable degree of accuracy.[3, 4] For his landmark discovery, Rabi received the Nobel Prize in Physics in 1944.

Rabi's work was soon followed by Felix Bloch and Edward Purcell, who in 1946 independently published the first NMR studies on condensed matter systems. Bloch was the first to observe an NMR signal in a liquid sample when he successfully recorded a ^{1}H signal on a sample of water.[5] Slightly earlier, Purcell performed the first solid-state NMR experiment when he observed a ^{1}H resonance in a sample of paraffin.[6] An interesting aspect of these two experiments is the different methods by which Bloch and Purcell detected the ^{1}H resonances. In Bloch's experiment, a receiver coil was used to measure the nuclear induction from the water sample after

RF irradiation at the ^{1}H Larmor frequency. In Purcell's experiment, he observed a sharp increase in the RF absorption of a resonator cavity when the ^{1}H Larmor frequency of the paraffin wax matched the resonant frequency of the cavity (~30 MHz). While both methods observe the interactions of ^{1}H nuclei with an external magnetic field, Bloch's observations follow a more classical description of NMR, while Purcell's observations are more indicative of a quantum mechanical observation. In 1952 Bloch and Purcell jointly shared the Nobel Prize in Physics for their efforts.

Prior to 1949, NMR experiments were performed using continuous wave methods. In continuous wave NMR (CW-NMR) experiments, the resonance condition is met by either 1) holding the RF field constant and sweeping the external magnetic field until the Larmor frequency of the given nucleus matches that of the constant RF field or 2) by holding the external magnetic field constant and sweeping the RF field until it matches the Larmor frequency of the given nucleus. In either case, this can be a slow process, and the resulting spectra often suffer from poor signal-to-noise. Modern NMR experiments utilize short RF pulses rather than continuous irradiation. In 1949 Erwin Hahn was the first to perform pulsed NMR experiments and to report the observation of a free-induction decay (FID).[7] Hahn quickly followed up this work by performing the first multiple pulse NMR experiment, discovering that a spin echo could be produced by applying a refocusing pulse after the initial excitation pulse.[8] These discoveries provided the building blocks for the pulsed NMR experiments that are used today.

Perhaps one of the most influential contributors to modern NMR is Richard Ernst. While working at Varian Associates in the 1960s, Ernst and Weston Anderson developed Fourier transform NMR (FT-NMR).[9] Rather than sweeping over a range of frequencies as would occur in CW-NMR, Ernst and Anderson utilized short, intense RF pulses to excite the entire NMR spectrum

at once. By using a computer to apply a Fourier transform to the resulting FID, Ernst and Anderson were able to acquire a full NMR spectrum in a fraction of the time of CW-NMR methods. The development of FT-NMR also allowed for more scans to be taken, which greatly increased the signal-to-noise of the NMR spectra. For his efforts Ernst was awarded the Nobel Prize in chemistry in 1991.

While Purcell may have been the first to perform solid-state NMR experiments, John Waugh was instrumental in transforming solid-state NMR into the high-resolution technique we know of today. While at MIT, Waugh and co-workers pioneered numerous techniques that would serve as the foundation for modern solid-state NMR experiments. Perhaps Waugh's most famous contribution to the field of magnetic resonance was the development of average Hamiltonian theory (AHT).[10] AHT is a form of time-dependent perturbation theory that can be used to evaluate time-dependent Hamiltonians for cases where the time dependence is periodic. This is especially useful for NMR methods such as magic angle spinning MAS, where the Hamiltonians exhibit a cyclical time dependence over the course of a given rotor period.

Over many decades, AHT has served as an indispensable tool for developing numerous NMR pulse sequences. In 1968, Waugh, Huber, and Haeberlen developed the famous homonuclear decoupling sequence WAHUHA, which they used to suppress the homonuclear dipolar couplings in a sample of CaF_2.[11] This was one of the first established techniques for obtaining high-resolution spectra in solid-state NMR. Utilizing the concepts from AHT, many other decoupling and recoupling sequences were also developed. This includes sequences such as REDOR,[12] MREV-8,[13] and TPPM decoupling[14] among countless others.[15, 16]

Waugh's influence does not extend to just AHT. In 1972, Pines, Gibby, and Waugh published a technique known as cross-polarization (CP).[17] CP is able to transfer the high spin

polarization of high-γ nuclei, such as ^{1}H, to lower-γ nuclei such as ^{13}C or ^{15}N. Using CP, the sensitivity of low-γ detected NMR experiments can be improved substantially. Furthermore, the acquisition time of these experiments can be reduced significantly by taking advantage of the shorter T_1 relaxation time of ^{1}H compared to many lower-γ nuclei. The CP pulse sequence was a groundbreaking development in the field of solid-state NMR and serves as a building block for many solid-state NMR pulse sequences today.

1.1.2 Background & Theory

NMR is an extremely powerful tool for studying the structure and dynamics of chemical systems. This section is provides a brief overview of the aspects of NMR that are most relevant for the topics discussed in this thesis. For a more comprehensive background on NMR techniques and theory, the reader is referred to other literature.[18-20]

1.1.2.1 The Zeeman Hamiltonian

For nuclei with non-zero spin (I≠0), there is a magnetic moment, μ, associated with the nucleus that is given by

$$\mu = \gamma I \tag{1.1}$$

where I is the nuclear spin and γ is the gyromagnetic ratio of the nucleus. In the absence of an external magnetic field, a nuclear state with spin I has 2I+1 degenerate energy levels. When nuclei with non-zero spin are placed in an external magnetic field, those energy levels are no longer degenerate and undergo Zeeman splitting. An example of Zeeman splitting for spin-1/2 nuclei is seen in Figure 1.1. In an external magnetic field, these nuclei will also process about the magnetic field at a frequency, ω_0, given by

$$\omega_0 = \gamma B_0 \tag{1.2}$$

where B_0 is the strength of the external magnetic field.

The Zeeman Hamiltonian, $\hat{H}$, is defined as

$$\hat{H} = -\gamma\hbar\hat{I}_z B_0 \quad \textbf{1.3}$$

where $\hbar$ is Planck's constant and $\hat{I}_z$ is the z-component of the spin angular momentum operator. The eigenfunctions of $\hat{H}$ and $\hat{I}_z$ are $|I,m\rangle$, where m is the spin quantum and can take on 2I+1 values: I, I-1, I-2,…,-I. Applying the operator $\hat{I}_z$ to the eigenfunction $|I,m\rangle$ returns the eigenvalue m

$$\hat{I}_z|I,m\rangle = m|I,m\rangle \quad \textbf{1.4}$$

where m is the spin quantum number. Therefore, the energy, $E_{I,m}$, of a given quantum state is given by

$$\hat{H}|I,m\rangle = -\gamma\hbar B_0 m|I,m\rangle \quad \textbf{1.5}$$

where

$$E_{I,m} = -\gamma\hbar B_0 m. \quad \textbf{1.6}$$

We can see that the energy difference between two energy states for the spin-1/2 case is thus

$$\Delta E = \gamma\hbar B_0 = \hbar\omega. \quad \textbf{1.7}$$

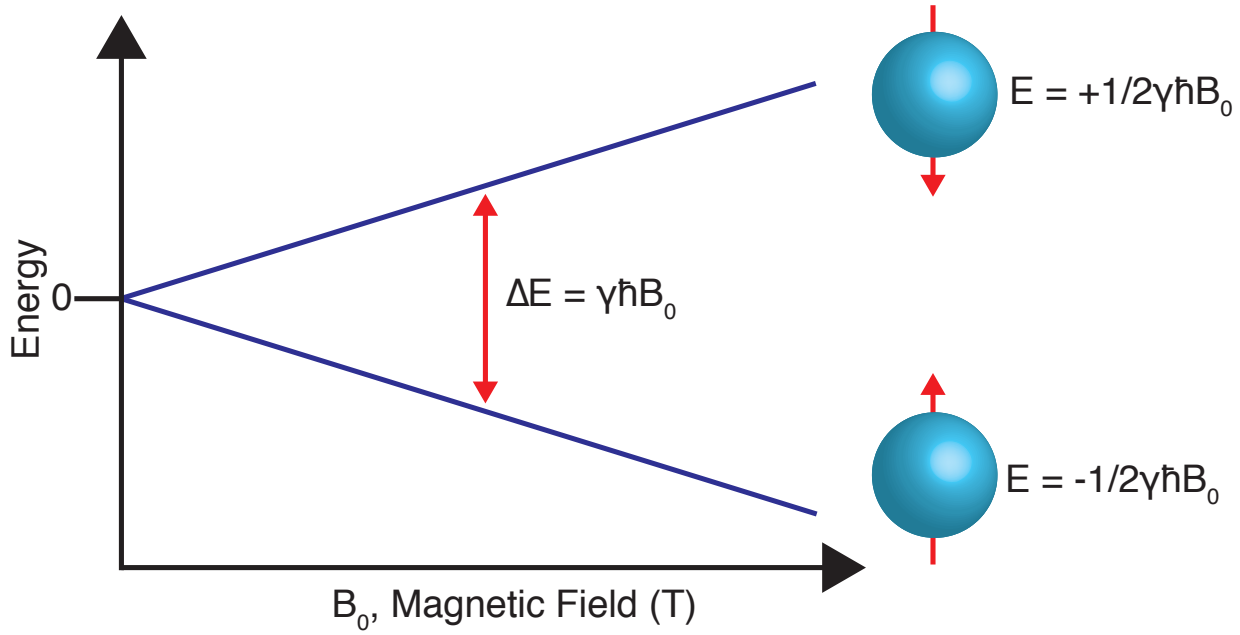

Figure 1.1: Energy level diagram for Zeeman splitting in a magnetic field for spin-1/2 nuclei.

The population difference between two energy levels is given by the Boltzmann factor

$$\frac{N_{-1/2}}{N_{+1/2}} = e^{(\Delta E/k_B T)} \qquad \textbf{1.8}$$

where $N_{-1/2}$ is the number of spins in the -1/2 state, $N_{+1/2}$ is the number of spins in the +1/2 state, k_B is the Boltzmann constant, and T is temperature. The polarization of the system is given by

$$P = \frac{N_{+1/2} - N_{-1/2}}{N_{+1/2} + N_{-1/2}} = \tanh\left(\frac{\gamma\hbar B_0}{2k_B T}\right) \qquad \textbf{1.9}$$

In the high temperature limit this can be approximated as

$$P = \frac{\gamma\hbar B_0}{2k_B T} \qquad \textbf{1.10}$$

At room temperature the excess of spins in the low energy state amounts to a few spins per million. Therein lies one of the biggest limitations with NMR: sensitivity.

1.1.2.2 The Chemical Shift Interaction

The electrons surrounding nuclei can react with an external magnetic field to produce a secondary field in the vicinity of the nucleus. This interaction is known as the chemical shielding interaction and causes a shift in the resonance frequency of the nucleus. The chemical shielding

interaction can give rise to chemical shift anisotropy (CSA) in solid-state NMR spectra. The chemical shielding Hamiltonian is given by

$$\hat{H}_{cs} = -\gamma\hbar\hat{I}\cdot\sigma\cdot B_0 \quad \textbf{1.11}$$

where σ is the chemical shielding tenor, given by

$$\sigma = \begin{bmatrix} \sigma_{xx} & \sigma_{xy} & \sigma_{xz} \\ \sigma_{yx} & \sigma_{yy} & \sigma_{yz} \\ \sigma_{zx} & \sigma_{zy} & \sigma_{zz} \end{bmatrix} \quad \textbf{1.12}$$

The chemical shift tensor can be expressed with respect to a principle axis frame (PAF) such that the chemical shielding tensor is diagonalized. In the PAF, the isotropic chemical shielding value σ_{iso}, anisotropy Δ, and asymmetry η are given as

$$\sigma_{iso} = \frac{1}{3}\left(\sigma_{xx}^{PAF} + \sigma_{yy}^{PAF} + \sigma_{zz}^{PAF}\right) \quad \textbf{1.13}$$

$$\Delta = \sigma_{zz}^{PAF} - \sigma_{iso} \quad \textbf{1.14}$$

$$\eta = \left(\sigma_{xx}^{PAF} + \sigma_{yy}^{PAF}\right)/\sigma_{zz}^{PAF} \quad \textbf{1.15}$$

1.1.2.3 The Dipolar Interaction

The dipolar interaction takes place between the magnetic moments of two different nuclear spins. The Hamiltonian describing the dipole coupling between two spins, I and S, is given by

$$\hat{H} = -\left(\frac{\mu_0}{4\pi}\right)\gamma_I\gamma_S\hbar\left(\frac{I\cdot S}{d^3} - 3\frac{(I\cdot r)(S\cdot r)}{d^5}\right) \quad \textbf{1.16}$$

where μ_0 is the permeability constant, **r** is the vector between the spin pair, and d is the distance between the pair. Expressing the Hamiltonian in spherical coordinates, the dipolar Hamiltonian can be rewritten as

$$\hat{H} = -\left(\frac{\mu_0}{4\pi}\right)\frac{\gamma_I\gamma_S\hbar}{d^3}[A + B + C + D + E + F] \quad \textbf{1.17}$$

where

$$A = \hat{I}_z\hat{S}_z(3cos^2\theta - 1)$$
$$B = -\frac{1}{4}\left[\hat{I}_+\hat{S}_- + \hat{I}_-\hat{S}_+\right](3cos^2\theta - 1) \quad \textbf{1.18}$$

$$C = -\frac{3}{2}\left[\hat{I}_z\hat{S}_+ + \hat{I}_+\hat{S}_z\right]\sin\theta\cos\theta e^{-i\emptyset}$$

$$D = -\frac{3}{2}\left[\hat{I}_z\hat{S}_- + \hat{I}_-\hat{S}_z\right]\sin\theta\cos\theta e^{+i\emptyset}$$

$$E = -\frac{3}{4}\left[\hat{I}_+\hat{S}_+\right]\sin^2\theta e^{-2i\emptyset}$$

$$F = -\frac{3}{4}\left[\hat{I}_-\hat{S}_-\right]\sin^2\theta e^{+2i\emptyset}$$

and $I_\pm$ and $S_\pm$ represent the raising and lowering operators for spins I and S. Using the secular approximation, we find that terms A and B are dominant. Therefore, the dipolar interaction Hamiltonian for homonuclear and heteronuclear couplings is given by

$$\widehat{H}_{homo} = -\left(\frac{\mu_0}{4\pi}\right)\frac{\gamma_I\gamma_S\hbar}{d^3}(3cos^2\theta - 1)\left[\hat{I}_z\hat{S}_z - \frac{1}{2}\left(\hat{I}_x\hat{S}_x + \hat{I}_y\hat{S}_y\right)\right] \quad \textbf{1.19}$$

$$\widehat{H}_{hetero} = -\left(\frac{\mu_0}{4\pi}\right)\frac{\gamma_I\gamma_S\hbar}{d^3}(3cos^2\theta - 1)\hat{I}_z\hat{S}_z \quad \textbf{1.20}$$

respectively. Dipolar couplings are especially important for MAS NMR, as precise measurement of the dipolar couplings can be used to obtain accurate distance constraints.

1.1.3 Magic Angle Spinning NMR

In solution NMR experiments, anisotropic interactions such as chemical shifts and dipolar couplings are isotropically averaged due to rapid molecular tumbling of the molecules in solution. While this significantly improves the sensitivity and resolution of the resulting NMR spectra, the structural information that is contained in these anisotropies may be lost. A further drawback of solution NMR is that larger protein systems become more difficult to study due to slower tumbling rates.

In contrast to solution NMR, in solid-state NMR, isotropic averaging is accomplished via a technique known as magic angle spinning (MAS). For an interaction tensor at an angle θ, the average of the term $(3\cos^2\theta\text{-}1)$ over time is shown to be

$$\langle 3cos^2\theta - 1\rangle = \frac{1}{2}(3cos^2\theta_R - 1)(3cos^2\beta - 1) \quad \textbf{1.21}$$

where θ_R is angle between the axis of rotation and the magnetic field and β is the angle between the principle z-axis of the tensor and the axis of rotation. When θ_R is set to 54.74°, otherwise known as the "magic angle", the term ($3\cos^2\theta$-1) equals zero. Thus, assuming the sample is being spun fast enough, magic angle spinning offers the ability to average these anisotropic terms to zero.

1.1.3.1 MAS & Quadrupoles

Approximately 74% of NMR-active nuclei, including ^{17}O, are quadrupolar nuclei (I > 1/2). While spin-1/2 nuclei have a spherical charge distribution surrounding the nucleus, quadrupolar nuclei have an asymmetrical charge distribution. This asymmetrical charge distribution gives rise to a nuclear quadrupole moment that can interact with electric field gradients (EFG). The quadrupole interaction affects the nuclear spin energy levels of the system and can lead to substantial broadening of NMR line shapes.

The Hamiltonian for the quadrupolar interaction is given by

$$\hat{H}_Q = \frac{eQ}{2I(2I-1)\hbar} I \cdot V \cdot I \quad \textbf{1.22}$$

where e is the proton charge, Q is the electric quadrupole moment, and **V** is the EFG tensor given as

$$V = \begin{bmatrix} V_{xx} & V_{xy} & V_{xz} \\ V_{yx} & V_{yy} & V_{yz} \\ V_{zx} & V_{zy} & V_{zz} \end{bmatrix} \quad \textbf{1.23}$$

The quadrupole coupling constant is defined as

$$C_Q = \frac{eQV_{zz}}{h} \quad \textbf{1.24}$$

and the asymmetry of the interaction is given as

$$\eta_Q = \frac{(V_{xx} - V_{yy})}{V_{zz}} \qquad \textbf{1.25}$$

Although the quadrupole coupling constant may be on the order of tens of kHz to MHz, it is generally still much smaller than the Zeeman interaction. The Hamiltonian for the quadrupolar interaction can thus be treated as a perturbation of the Zeeman Hamiltonian. An energy diagram showing the change in energy levels due to the first and second order quadrupole interaction can be seen in Figure 1.2.

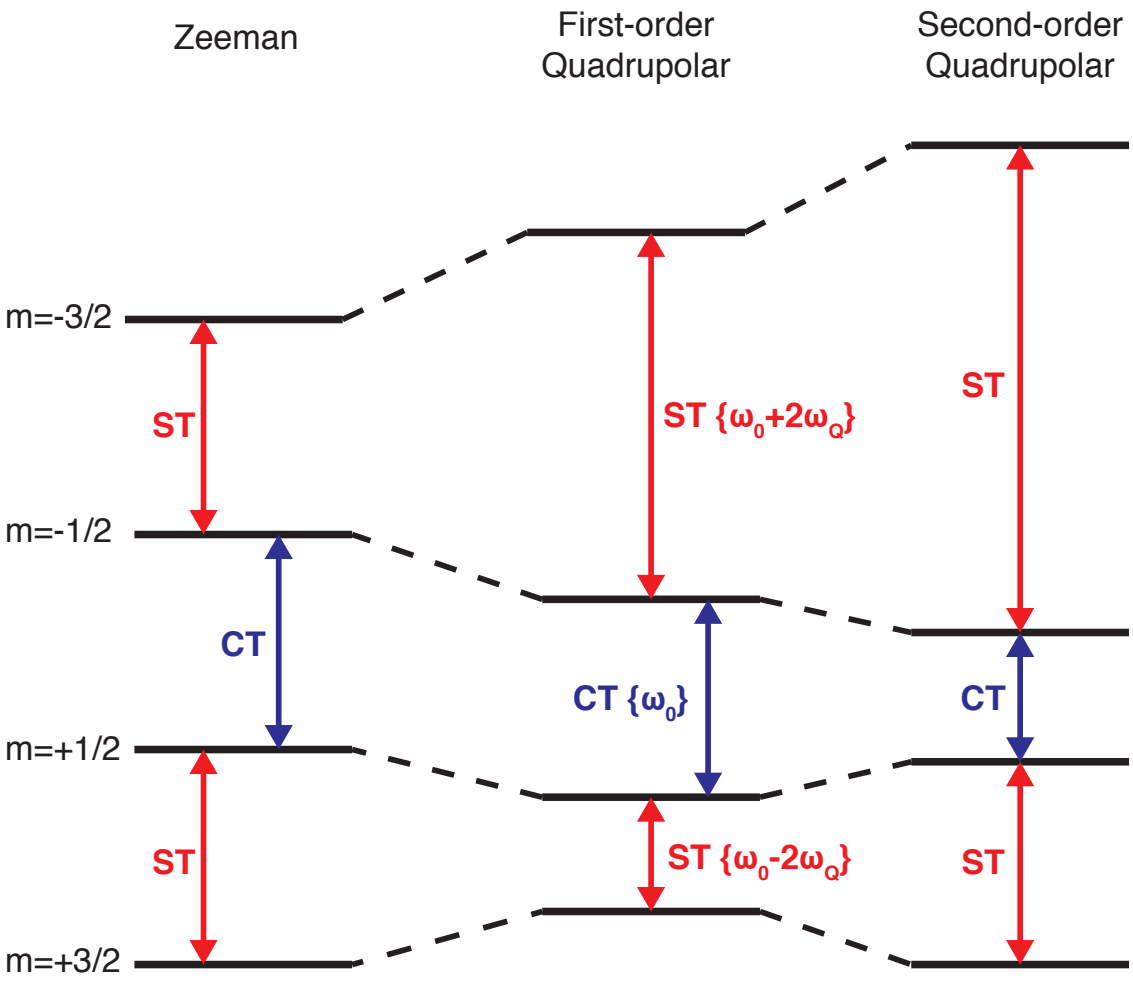

Figure 1.2: Energy level diagram of a spin-3/2 system with first and second-order quadrupole coupling.

The first-order quadrupole interaction has a second-rank tensor that can be averaged to zero under MAS. In contrast, the second-order quadrupole interaction has both second and fourth rank

tensors, so the second-order quadrupole interaction is only partially averaged by MAS. The fact that the second-order quadrupole interaction is only partially averaged my MAS is problematic, as this interaction can be a significant source of line broadening. The second-order quadrupole interaction has a B_0^{-1} dependence, meaning that one of the most straightforward means of reducing this broadening is to perform quadrupole NMR experiments at high fields.

For cases in which the second-order quadrupolar broadening is large, there are methods for obtaining high resolution spectra. One experiment that yields high resolution quadrupole spectra is the MQMAS experiment, a 2D experiment in which the isotropic and anisotropic contributions to the line shape can be displayed in separate dimensions.[21] This experiment has been shown to yield high-resolution spectra in the isotropic dimension.[22] Other experiments such as the STMAS experiment have also been shown to yield high resolution spectra of quadrupolar nuclei, however, the STMAS experiment is far more sensitive to offsets in the magic angle and spinning frequency.[23, 24]

1.2 Dynamic Nuclear Polarization

1.2.1 Introduction

The primary limitation of NMR compared to other spectroscopic techniques is its inherently low sensitivity. One method for significantly improving the sensitivity of NMR experiments is Dynamic Nuclear Polarization (DNP). The concept of DNP was first proposed by Albert Overhauser in 1953, who suggested that nuclei could be polarized by saturating the electron paramagnetic resonance (EPR) transitions of nearby electrons.[25] At the time, this effect was proposed to be applicable only to metals. Later that same year, Overhauser's theory was experimentally verified by Thomas Carver and Charles Slichter, who observed an approximately

100-fold signal enhancement of lithium metal suspended in glycerin.[26] A short time later, Carver and Slichter reported observing a ^{1}H DNP enhancement on a sample of Na^{+} in liquid NH_3.[27]

DNP is able to substantially increase the nuclear polarization of an NMR sample by transferring spin polarization from unpaired electrons to the nuclei of interest. In theory, the resulting enhancement (ε) is proportional to the gyromagnetic ratios of the unpaired electron (γ_e) and the nuclei of interest (γ_n). Correspondingly, the savings in acquisition time scales as ε^2. A plot of the relative polarization of electrons and common NMR nuclei as a function of temperature can be seen in Figure 1.3. In practice, the actual enhancement is dependent on several additional parameters, including the strength of the static magnetic field, the available microwave power, the unpaired electron concentration, and the electron (T_{1e}) and nuclear (T_{1n}) relaxation times. These parameters can be affected by factors such as instrumentation and sample preparation, which will be discussed in the following sections.

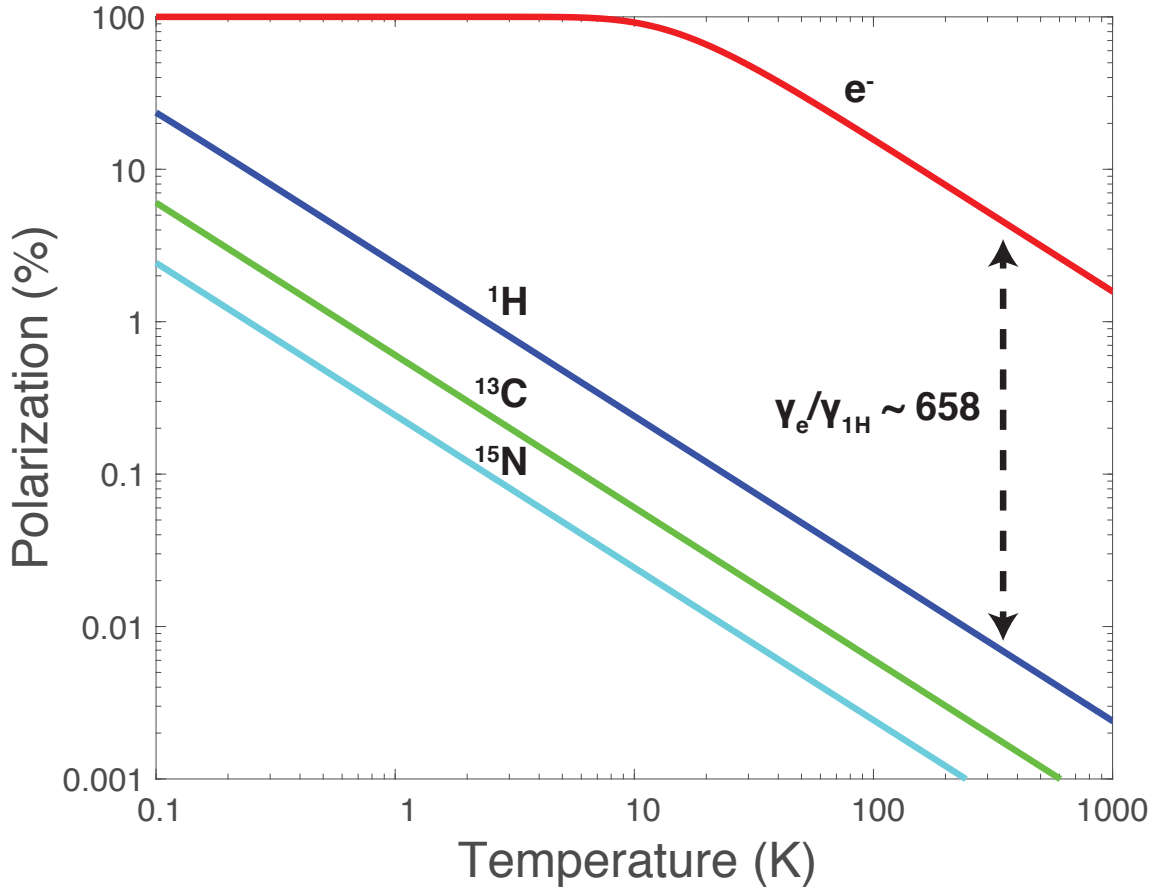

Figure 1.3: Polarization plot of electrons and common NMR nuclei a function of temperature. In this plot the external magnetic field strength is $\omega_{0H}/2\pi$ = 1GHz. Polarization transfer most commonly occurs between electrons and ^{1}H, which has a maximum theoretical enhancement of 658.

1.2.2 DNP Mechanisms

The transfer of polarization from electrons to nuclei can be accomplished via several different DNP mechanisms. The dominant DNP mechanism is determined by many different factors, including the inhomogeneous width (Δ) of the EPR spectrum, the homogenous EPR linewidth (δ), and the nuclear Larmor frequency (ω_0). DNP mechanisms can be broken into two categories: continuous-wave DNP and time domain DNP. The DNP mechanisms discussed in this chapter concern continuous-wave DNP mechanisms.

1.2.2.1 Solid Effect

The solid effect (SE) was the first reported DNP mechanism for insulating solids.[28-30] This DNP mechanism is applicable for polarizing agents where $\delta,\Delta<\omega_0$. The SE is a two-spin DNP mechanism between an electron spin and a hyperfine-coupled nucleus. Nuclear polarization is achieved by microwave irradiation at either the zero quantum (ZQ) or double quantum (DQ) transitions. These "forbidden transitions" become partially allowed due to mixing of the nuclear spin states, however, they generally require higher microwave power levels to achieve appreciable polarization transfer.[31] As a result of the state mixing, the SE scales with B_0^{-2} making it less efficient at higher magnetic fields. The energy level diagram that describes SE polarization transfer can be seen in Figure 1.4.

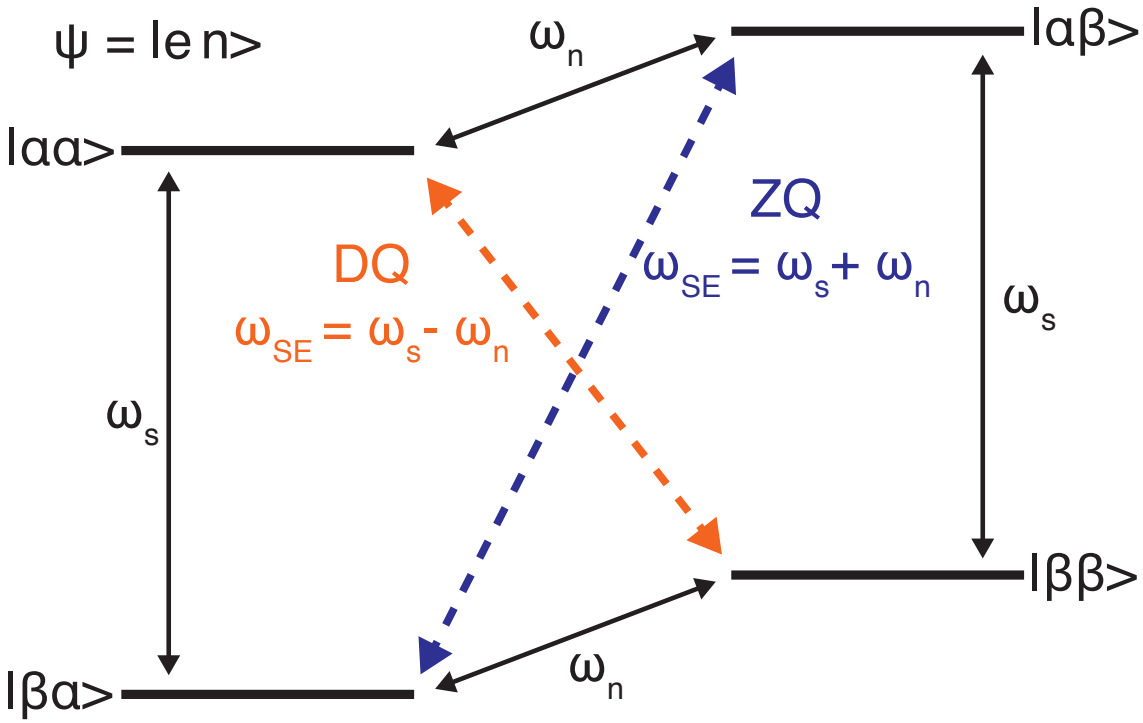

Figure 1.4: Four-level energy diagram describing polarization transfer via the solid effect. Microwave irradiation at the DQ transition frequency results in positive DNP enhancements, while irradiation at the ZQ transition frequency results in negative DNP enhancements.

1.2.2.2 Cross Effect

The cross effect (CE) was first discovered by Kessinkh et. al. in 1963[32] and was further investigated a short time later by Hwang and Hill.[33] Unlike the SE, the CE is a three-spin DNP mechanism in which two dipolar-coupled electrons are hyperfine coupled to a nucleus. The CE condition is met when $\delta<\omega_0<\Delta$ and can be described by an eight-level energy diagram as seen in Figure 1.5. To transfer polarization to a given nucleus via the CE, microwave irradiation occurs at the EPR transition of one of the dipolar-coupled electrons. This causes an excitation in the second dipolar-coupled electron spin via a DQ or ZQ transition. If $|\omega_{e1} - \omega_{e2}| = \omega_0$ a third transition can occur where the hyperfine-coupled nuclear spin is then excited as well. Due to broadening of the EPR spectrum at higher fields, the CE scales as B_0^{-1}, which indicates that it scales more favorably than the SE with respect to increasing magnetic fields. A more detailed analysis of the CE mechanism can be found in other literature.[34, 35]

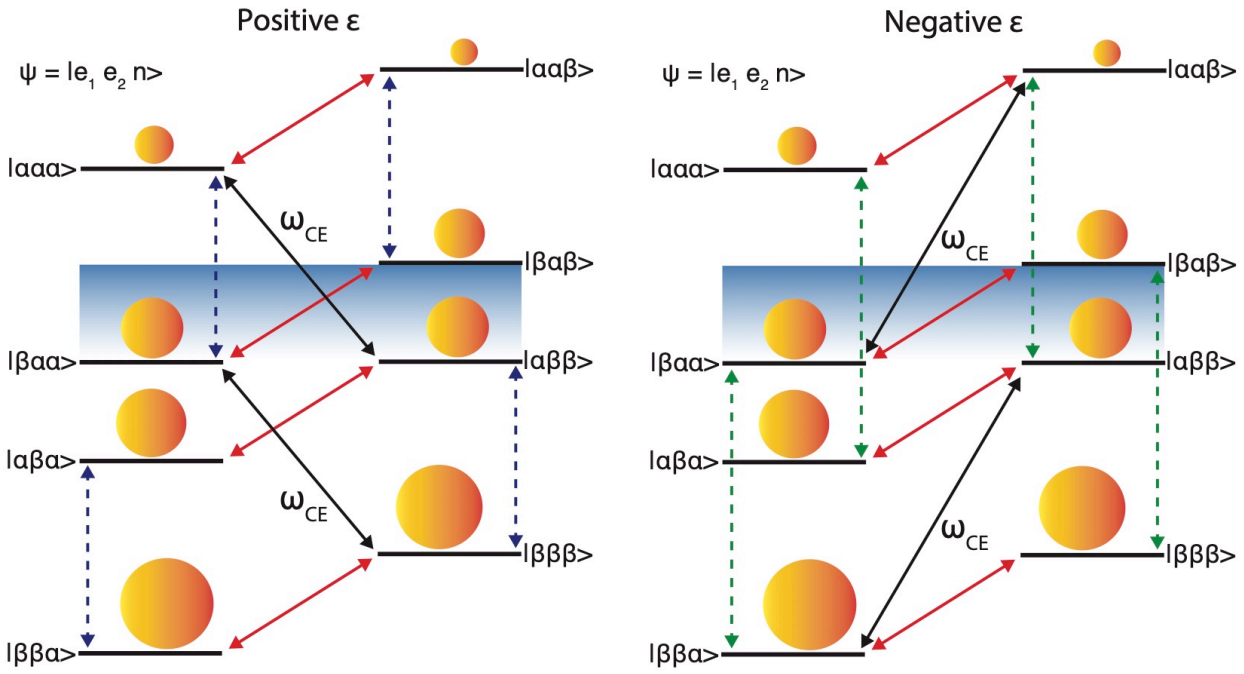

Figure 1.5: Eight-level energy diagrams describing CE polarization mechanism. Blue and green dashed lines represent EPR transitions for e_1 and e_2, respectively. Solid red lines indicate NMR transitions, and solid black lines indicate CE transitions. The determination of whether the resulting DNP enhancement is positive or negative depends on whether the EPR transition of e_1 or e_2 is saturated.

1.2.2.3 Overhauser Effect

Historically, it was believed that the Overhauser effect (OE) was only seen in systems with mobile electrons such as metals and liquids.[26, 27] However, the OE has recently been observed for the case of insulating solids as well.[36] Like the SE, the OE is a two-spin DNP mechanism. Hyperpolarization via the OE is not achieved by microwave irradiation at the DQ or ZQ transitions but rather by DQ and ZQ relaxation mechanisms. Microwave irradiation in OE experiments takes place at the single-quantum (SQ) transition frequency and thus is capable of being saturated at much lower power levels than the SE. The sign and magnitude of the resulting enhancement is determined by the difference in the DQ and ZQ relaxation rates. Unlike the SE and CE, OE enhancements in insulating solids appear to increase with respect to increasing magnetic field, perhaps making it the DNP mechanism of choice for high-field experiments.

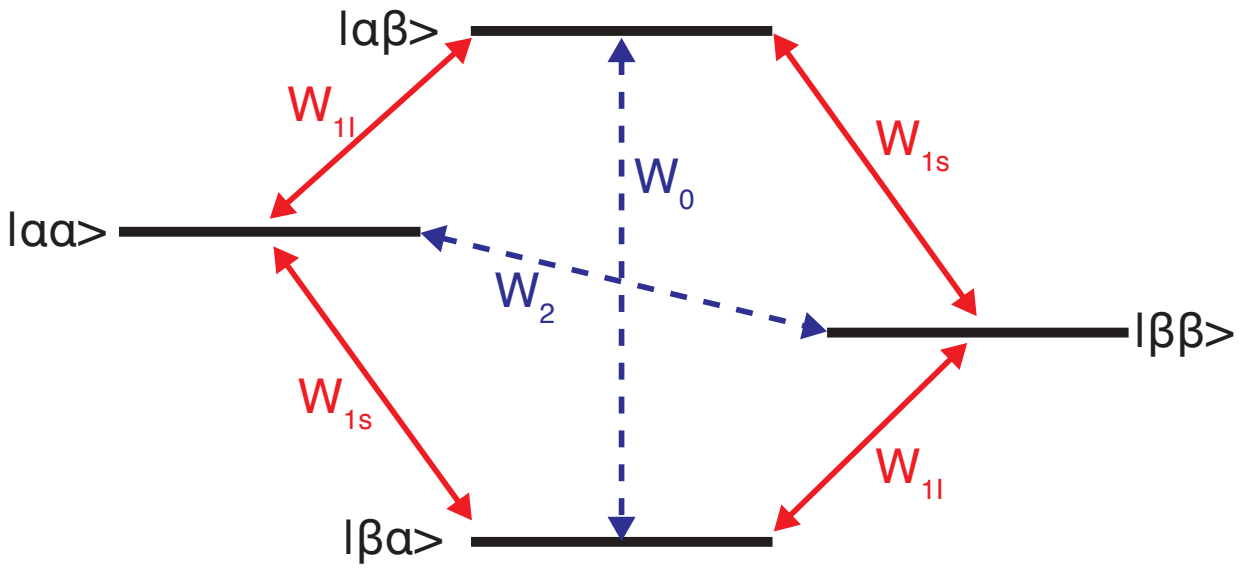

Figure 1.6: Overhauser effect energy level diagram. Electron and nuclear SQ transitions are indicated in red. DQ and ZQ transitions are indicated in blue.

1.2.3 Solvents & Polarizing Agents

DNP solvents typically form a glassy matrix that serves as both a cryoprotectant for the sample as well as a means to homogenously distribute the radical throughout the sample. The exact matrix used depends on the solubility of the sample and radical. Standard solvents for DNP include "DNP juice" (d_8-glycerol/D_2O/H_2O, 60/30/10 v/v/v), d_8-DMSO/D_2O/H_2O, tetrachloroethane (TCE)/methanol, and ortho-terphenyl (OTP) among others. Typically, a significant portion of the DNP matrix is deuterated to better facilitate spin diffusion between ^1H in the solvent and the sample of interest.

As mentioned previously, the dominant DNP mechanism is dependent on the inhomogeneous width of the EPR spectrum, Δ, as well as the homogenous EPR linewidth, δ. For the SE and OE, the radical linewidth must be $\delta,\Delta<\omega_0$ while the CE requires that $\delta<\omega_0<\Delta$. To date the only radicals that have shown an OE in insulating solids are the narrow-line radicals BDPA and SA-BDPA. SA-BDPA is advantageously water-soluble, however it appears to give lower OE

enhancements than BDPA.[36] For CE DNP experiments, bis-nitroxide radicals are commonly used. To facilitate matching of the CE condition, radicals such as TOTAPOL[37] and AMUPol[38] contain a chemical linker used to optimize the g-tensor orientation of the electron radicals for CE DNP. Commonly used DNP radicals can be seen in Figure 1.7.

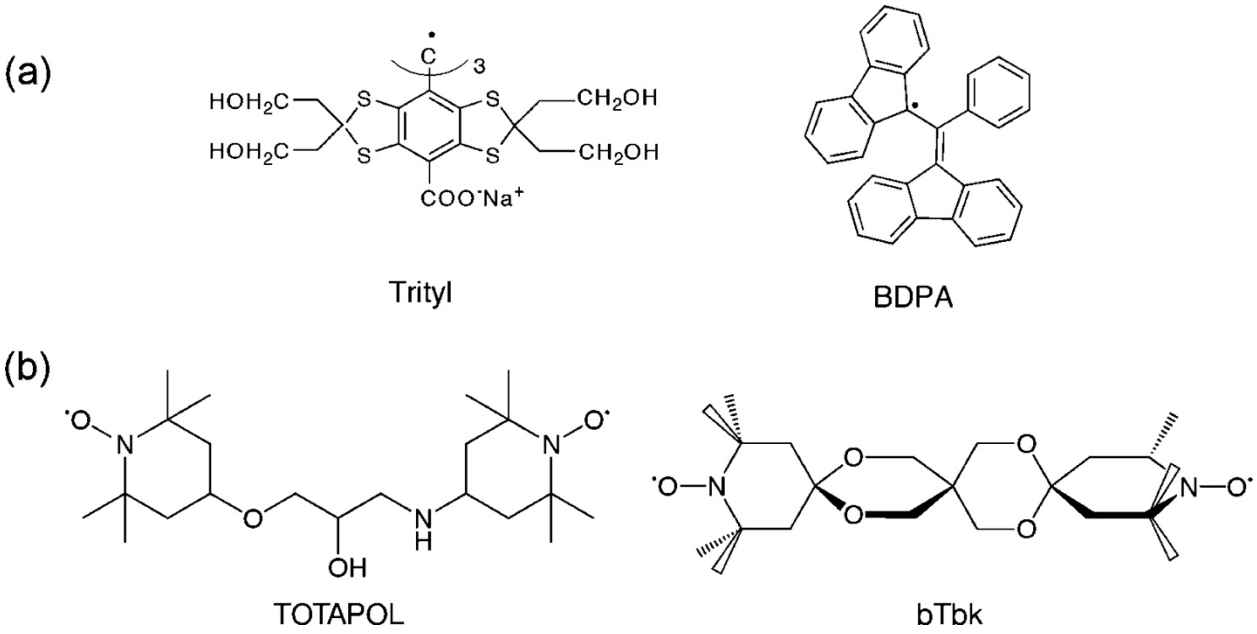

Figure 1.7: Common DNP radicals. (a) Narrow-line radicals Trityl and BDPA. (b) Bis-nitroxide radicals TOTAPOL and bTbk. Reprinted with permission.[39]

1.2.4 DNP Instrumentation

There are four essential pieces of instrumentation for MAS DNP: a microwave source for irradiating electrons, a low-loss waveguide to transmit microwaves from the source to the sample, a cryogenic setup to cool the sample, and a MAS DNP probe to perform NMR experiments. Each of these components plays a unique but critical role in determining the efficiency of DNP experiments.

1.2.4.1 Microwave Sources

When performing DNP experiments, it is important to use a microwave source with the capabilities necessary to achieve the required results. Generally, microwave sources for DNP can

be divided into two classes: solid-state devices and vacuum electronic devices (VEDs). The latter class includes devices such as gyrotrons, klystrons and traveling-wave tubes (TWT), which are some of the more commonly used microwave sources for DNP experiments. VEDs can be further divided into fast-wave (gyrotrons) or slow-wave (klystrons, TWT) structures depending on whether the phase velocity of the electromagnetic wave is faster or slower than the speed of light. These microwave sources vary significantly in terms of their available frequency output, power output, cost, and operational lifetime. A summary of the various microwave sources available for DNP can be seen in Figure 1.8.[40]

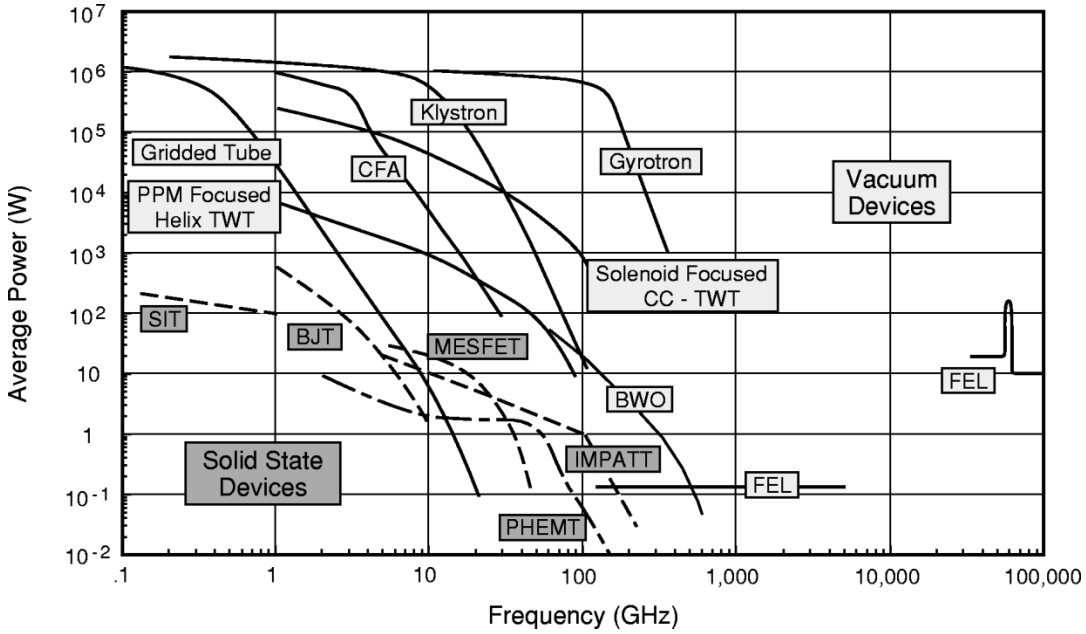

Figure 1.8: Power vs. frequency plot for various VED and solid-state devices. Reprinted with permission.[40]

The most commonly used microwave source for DNP is gyrotrons. Gyrotrons offer significant advantages over their slow-wave counterparts including higher microwave power output and longer operational lifetimes. Furthermore, gyrotrons remain the optimal choice for performing DNP experiments at high magnetic fields (>10 T). The development of gyrotrons for DNP was pioneered by Griffin, Temkin, and co-workers in the 1990s with the development of a

140 GHz gyrotron operating at 5 T.[41] Since then, the frequency output of gyrotrons for DNP has increased substantially, with commercial gyrotrons now available at 593 GHz.[42]

The primary components of a gyrotron include an electron gun, superconducting magnet, open cavity waveguide, mode converter with mirrors, optical window, and a collector. Gyrotrons operate based on the phenomenon of electron cyclotron resonance. The frequency of the cyclotron resonance is given by

$$\omega_c = \frac{eB_0}{m_0\gamma} \qquad \textbf{1.26}$$

where e is the electron charge B_0 is the main magnetic field, m_0 is the rest mass of the electron, and $\gamma = 1/\sqrt{v^2 - c^2}$ is a relativistic correction factor. An electron gun used to generate an annular electron beam is accelerated through a vacuum by a high-voltage source. The electrons pass through an interaction cavity where their cyclotron resonance generates coherent microwave radiation at the designated gyrotron frequency. The microwave radiation is converted from a TE_{mn} mode to a Gaussian mode by a quasi-optical mode converter before exiting the gyrotron through an optical window. The spent electron beam is then dumped into a collector. A schematic of a gyrotron can be seen in Figure 1.9.[43]

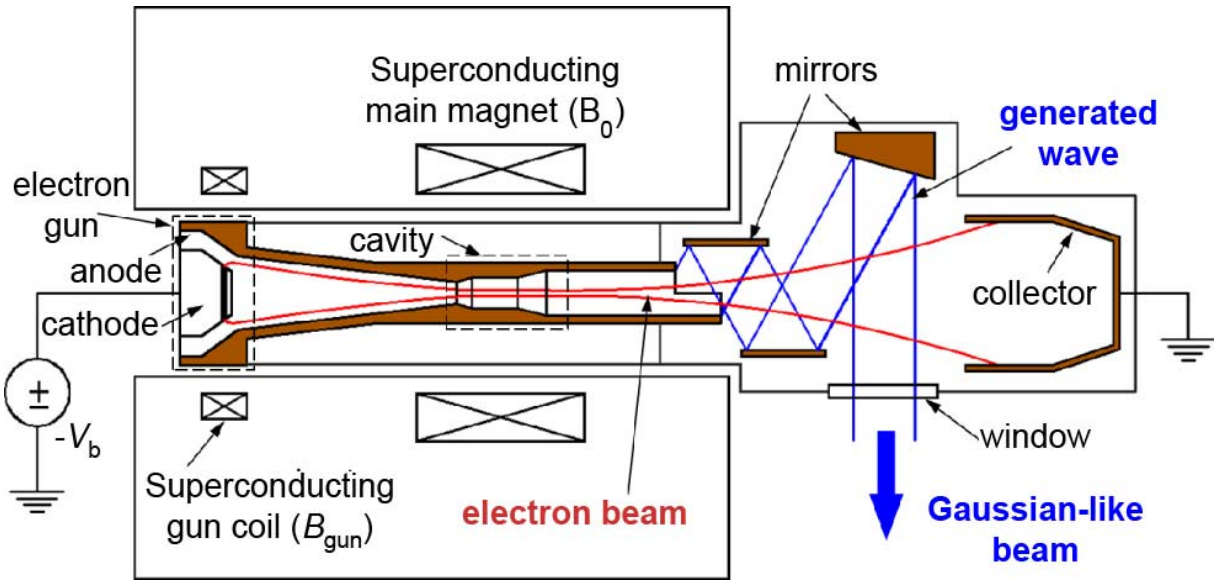

Figure 1.9: Schematic of a gyrotron. Reprinted with permission.[43]

Klystron and solid-state sources are lower cost alternatives to gyrotrons. Unlike gyrotrons, these microwave sources do not require superconducting magnets for operation, which makes them more economical and reduces space constraints. The limitation of these devices is the lower power output, particularly at higher magnetic fields. Due to power limitations, the range of frequencies that klystrons and solid-state diodes are able to achieve is limited to the sub-THz region (<300 GHz). Nevertheless, with proper microwave coupling designs, klystrons and solid-state diodes have been able to achieve enhancements greater than 100 on DNP samples.[44, 45]

1.2.4.2 Waveguides

To prevent interference between the NMR magnet and microwave source, metallic waveguides are typically used to transfer microwave radiation from the source to the probe.[46] In order to maximize power transfer to the sample, power losses along the length of the waveguide must be kept to a minimum. This can be accomplished via overmoded corrugated waveguides as seen in Figure 1.10. The dimensions of the corrugated waveguide can be optimized to minimize power losses. This occurs when the corrugation groove depth is $d \approx \lambda/4$, the period of the grooves

is p ≈ λ/3, and the groove width is w < p/2.[47] Ohmic losses in these corrugated waveguides are generally less than 0.1 dB/m. Changes in the direction of propagation along the waveguide is achieved via metallic miter bends. Most power loss that occurs in waveguides is typically due to power losses at the miter bends and misalignment of the waveguide.

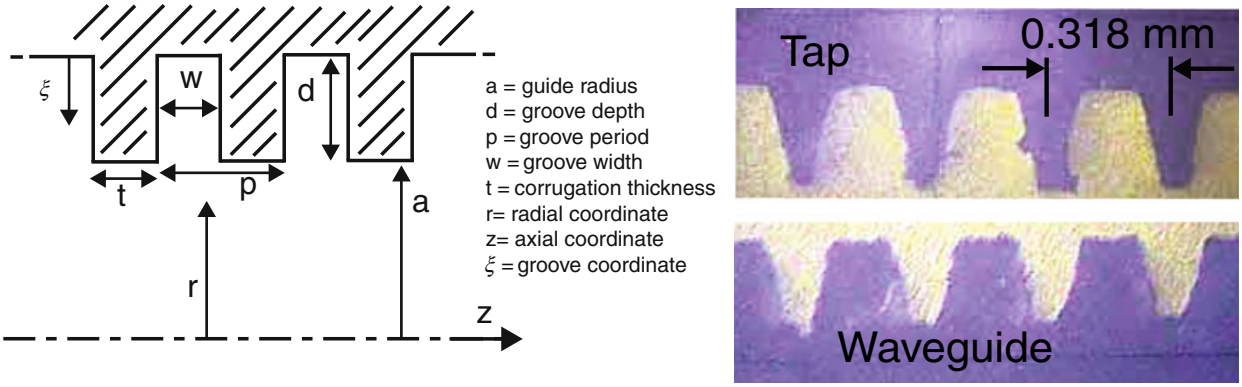

Figure 1.10: Schematic of corrugated waveguide. (Left) Corrugated waveguide parameters. (Right) Picture of tap used to make corrugations in waveguide. Reprinted with permission.[47]

Due to space constraints in the probe, at a certain point, the diameter of the overmoded waveguide must be reduced in order to propagate along the small waveguide in the probe. This can be accomplished via a waveguide taper.[48, 49] While parabolic waveguide tapers may result in lower power loss,[50] due to ease of fabrication linear tapers are generally preferred. For a linear waveguide taper of length L, power losses in the waveguide taper are minimized when

$$L \approx 3.198 \frac{r_1 r_2}{\lambda} \qquad \textbf{1.27}$$

where r_1 is the reduced waveguide diameter, r_2 is the larger waveguide diameter, and λ is the wavelength of the radiation.[51]

1.2.4.3 Cryogenics

DNP works best when the electron EPR transitions can be saturated. For this reason, DNP experiments are generally performed at low temperatures (20-180 K) to maximize the T_1 relaxation of electron spin transitions. Low temperature MAS DNP experiments are generally performed

using either nitrogen or helium gas. Although helium gas is required to perform MAS DNP experiments below 77 K, nitrogen gas is generally preferred due to the high costs associated with helium spinning. For a more detailed overview of helium MAS please see Chapter 5.

A general setup for MAS at cryogenic temperatures is seen in Figure 1.11. Compressed air is first passed through a series of filters to remove compressor contaminants such as oil. Next, the air is passed through a dryer to remove any water vapor from the air. This is important, as excess water vapor may freeze at low temperatures, resulting in ice blocks in the cooling components of the system. A nitrogen generator is then used to generate >99% purity nitrogen gas. The removal of oxygen is particularly important, as its condensation point (~90 K) is within the temperature range of DNP experiments. Condensed oxygen in the system is a significant safety hazard, particularly when dealing with high voltage components in the probe that may be prone to arcing.

Once the nitrogen is purified, it is routed through a MAS control unit before proceeding to a set of Polycold refrigerators where it is cooled to 150-180 K. From there the gas is passed through a triple-can heat exchanger[52, 53] where it is further cooled to temperatures as low as 77 K before being transferred to the probe for MAS. The gas can then be exhausted from the probe via a vacuum-jacketed exhaust line. From the Polycolds onwards, all gas transfer lines are vacuum-jacketed to minimize heat loss to their surroundings.

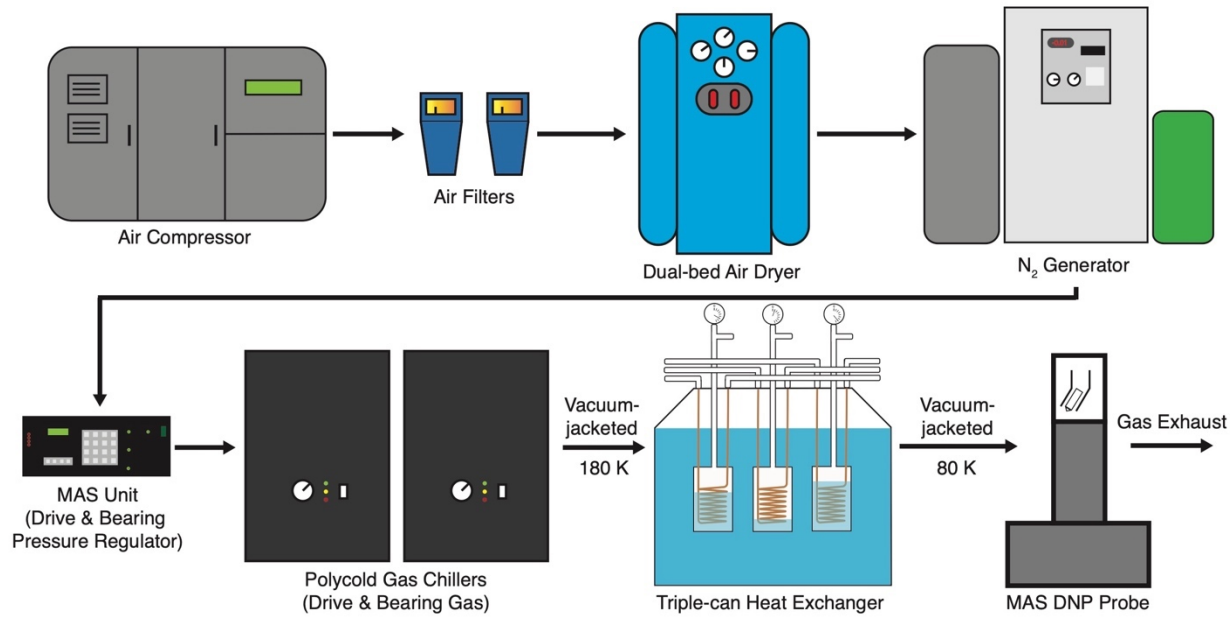

Figure 1.11: Schematic of a DNP setup with a nitrogen generator. First, room temperature air from a compressor is passed through a series of filters and dryers to remove dirt and moisture. The dry air is then sent to a nitrogen generator where pure (>99%) nitrogen gas is generated. From there, the purified nitrogen gas is sent to a pressure regulation unit before flowing through a pre-cooling refrigerator (optional) and heat exchanger to cool down to low temperatures before entering the probe.

1.2.4.4 MAS DNP Probes

The first DNP experiments to incorporate magic angle spinning were performed by Wind et. al.[54] Since then MAS DNP probe technology has developed substantially.[55-57] Generally, MAS DNP probes all have the same basic components: a stator for spinning the sample, cryogenic gas lines for cooling the probe and sample, and a waveguide for delivering microwaves to the sample. These components are normally housed within a low temperature oven to minimize heat loss to the surroundings and keep the sample cold. For MAS DNP probes, the waveguide is usually terminated by a miter bend at the supplementary angle (125.26°) of the magic angle. To ensure that the DNP sample forms a uniform glass, cryogenic sample exchangers are typically used for inserting and ejecting the sample.[58] The section of the DNP probe that is inserted into the bore of the magnet is generally housed within a vacuum-jacketed cryostat.[59] A schematic of a MAS DNP

probe and its components can be seen in Figure 1.12. For a more detailed overview of MAS DNP probes see Chapter 4.

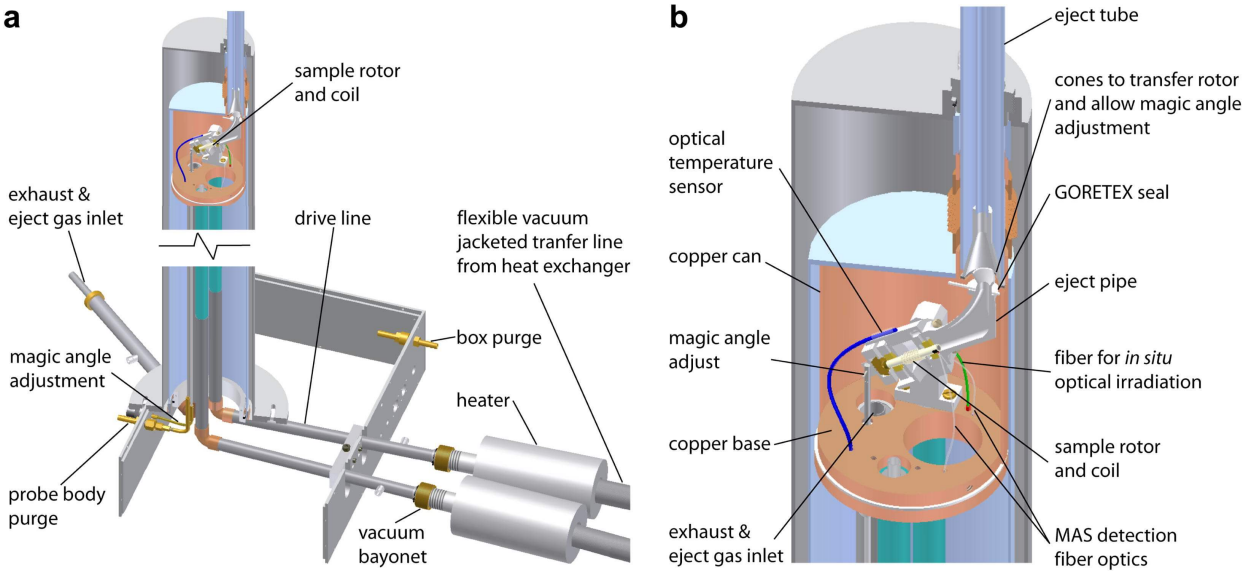

Figure 1.12: Schematic of DNP probe with cryostat. Reprinted with permission.[58]

1.3 Thesis Overview

This thesis focuses primarily on new developments in instrumentation for DNP and MAS NMR with emphasis on construction of novel equipment for ultra-fast MAS DNP.

Chapter 2 discusses applications of additive manufacturing technology for fabricating 3D printed components for MAS experiments. In particular, we demonstrate that a combination of ceramic and plastic 3D printing can be used to fabricate robust MAS stators and drive caps. We show that the performance of these stators and drive caps is comparable to commercial systems and that they can be manufactured at a fraction of the cost.

Chapter 3 describes experiments on the amyloidogenic peptide GNNQQNY. GNNQQNY is a short seven-residue peptide found in the prion-forming domain of the protein Sup35. The GNNQQNY system is unique in that it can form both amyloid fibrils and amyloid-like microcrystals. Due to its favorable DNP properties, GNNQQNY microcrystals are of great interest for performing ^{17}O DNP studies of bound water. Likewise, GNNQQNY amyloid fibrils display

polymorphism with a high degree of reproducibility. This makes the GNNQQNY system an ideal model system for studying amyloid polymorphism.

Chapter 4 gives a detailed overview of the design of a balanced transmission line DNP probe for ^{17}O NMR studies. This probe is designed to be equipped with a 1 mm stator and is compatible with a helium recirculation system. Using helium gas, we anticipate that this probe will spin MAS rotors at frequencies ≥ 80 kHz, allowing performance ^{1}H-detected DNP experiments on biological samples.

Chapter 5 provides a detailed overview of the design of a helium recirculation system for MAS DNP experiments. The helium recirculation system will be used to spin MAS rotors at frequencies up to three times what is achievable using nitrogen gas as the spinning medium. Furthermore, the cryogenic properties of helium gas will result in improved sensitivity in MAS DNP experiments. The chapter gives and in-depth analysis of the components needed to construct a helium recirculation system.

Chapter 6 discusses the fabrication of diamond MAS rotors for ultra-fast MAS and DNP experiments. A detailed analysis of the benefits of diamond rotor for MAS DNP as well as a thorough description of the machining apparatus and parameters are provided. The chapter also shows initial MAS tests with diamond rotors.

2 3D Printing MAS Stators & Drive Caps

This chapter is adapted from a manuscript by Daniel Banks, Brian Michael, Natalie Golota and Robert Griffin. (In prep)

2.1 Abstract

3D printing has evolved into an invaluable tool for rapid and cost-effective production of intricate parts. We employed 3D printing and other rapid prototyping methods to fabricate 3.2 mm MAS stators and drive caps for use in solid-state NMR experiments. These components can be fabricated with the assistance of computer-aided design (CAD) software and at a fraction of the cost of commercial parts. Additionally, we show that the performance of these 3D printed stators and drive caps is comparable to commercially available systems and that they have significant advantages over their machined counterparts.

2.2 Introduction

Solid-state magic-angle spinning (MAS) nuclear magnetic resonance (NMR) is a powerful method for studying a diverse range of chemical systems including biomolecules,[60-63] polymers,[64] and inorganic materials.[65-67] In solution NMR experiments, anisotropic interactions such as chemical shift anisotropies and dipolar couplings are isotropically averaged via rapid molecular tumbling in solution, leading to sharp lines and highly resolved spectra. In solid samples, isotropic averaging is achieved by rotating the sample rapidly about an axis oriented at the magic angle (54.74°) relative to the external magnetic field.[68, 69] This rotation is typically generated by packing the sample in a cylindrical rotor and pneumatically spinning it in a stator oriented at the magic angle.

The spinning stability of a rotor can play a critical role in MAS NMR experiments. Many MAS NMR pulse sequences require rotor-synchronized RF pulses,[12, 70, 71] making them sensitive to fluctuations in the sample rotation frequency. Furthermore, significant instability at high spinning frequencies can result in catastrophic rotor failure, otherwise known as a "rotor crash". The destruction from a rotor crash often results in irreparable damage to the rotor and sample while also causing significant damage to the MAS stator. In order to mitigate the damage and wear that may occur to MAS stators, it is advantageous to fabricate stator components from robust materials such as high-strength plastics or ceramics; however, the fabrications costs associated with these materials can be prohibitively expensive.

One possible solution to reduce the overall cost of fabricating MAS stators is to utilize additive manufacturing methods. Additive manufacturing, also known as 3D printing, has become an increasingly popular method for simple, rapid, and low-cost fabrication of parts. Additionally, the nature of additive manufacturing enables fabrication of parts with more complex shapes than traditional subtractive manufacturing methods such as machining can achieve. As such, 3D printing has become more prevalent for producing probe components in both solution and MAS NMR. Examples of this include stators for MAS spheres,[72, 73] dissolvable coil inserts,[74] and cryogenic sample exchangers[58] among others.[75, 76]

In this article, we demonstrate how 3D printing may be used to produce low-cost MAS stators for use in NMR experiments. While high-strength ceramics such as zirconia are commonly used for manufacturing MAS rotors, the difficulty and high costs associated with machining large zirconia parts make it less attractive for fabricating MAS stators. We utilize zirconia 3D printing, supplemented by machining, to produce high-strength zirconia stators in a cost-efficient manner. Zirconia is an ideal choice for 3D printing MAS stators given that: 1) zirconia is one of the few

ceramics readily capable of being 3D printed, 2) its high strength significantly decreases structural damage to the stator in the event of a rotor crash, and 3) unlike most of its plastic counterparts, zirconia stator components are not at risk of carbon tracking from electrical arcing. Where practical, we supplement our 3D printed zirconia stators with plastic 3D printed components to further reduce the production cost compared to traditional machining methods. Furthermore, we find that 3D printing drive caps can reduce the cost to consumers by nearly an order of magnitude relative to commercial prices while maintaining comparable spinning performance. This article focuses on the design and fabrication of a 3.2 mm MAS system.

2.3 Methods

2.3.1 Stator Design & Fabrication

The 3.2 mm MAS stator and rotor assemblies (Figure 2.1) were designed using Autodesk Inventor. The body of the MAS stator (Figure 2.1h) was 3D printed from zirconia by 3DCeram Sinto (Limoges, FR) while all ceramic machining for the MAS stator components and rotors was completed by O'Keefe Ceramics (Woodland Park, US). The alignment of the stator's radial air bearings requires a total indicated runout (TIR) on the order of less than 10 microns between the set to achieve optimal spinning. Additionally, the diameter of the radial air bearing air holes is small (0.25 mm) relative to the tolerances that can be achieved with ceramic 3D printing (±0.1 mm). For these reasons, the radial air bearings for the MAS assembly were machined out of zirconia rather than printed. To further satisfy the TIR constraint for the radial air bearings, the counterbores for the radial bearings were also machined rather than incorporated into the design of the 3D printed stator body.

Most plastic components of the MAS assembly, including the gas inlet bushings (Figure 2.1g), coil block (Figure 2.1i), bottom plate (Figure 2.1j), and fiber optic block (Figure 2.1n) were 3D printed in-house using clear resin on a Formlabs (Somerville, US) Form 3 printer at a resolution setting of 25 microns. The Form 3 printer was not capable of producing the drive caps (Figure 2.1a) and drive plate (Figure 2.1d) due to the very fine detail required by these components. Therefore, they were 3D printed out of microfine green resin by Protolabs (Maple Plain, MN) instead.

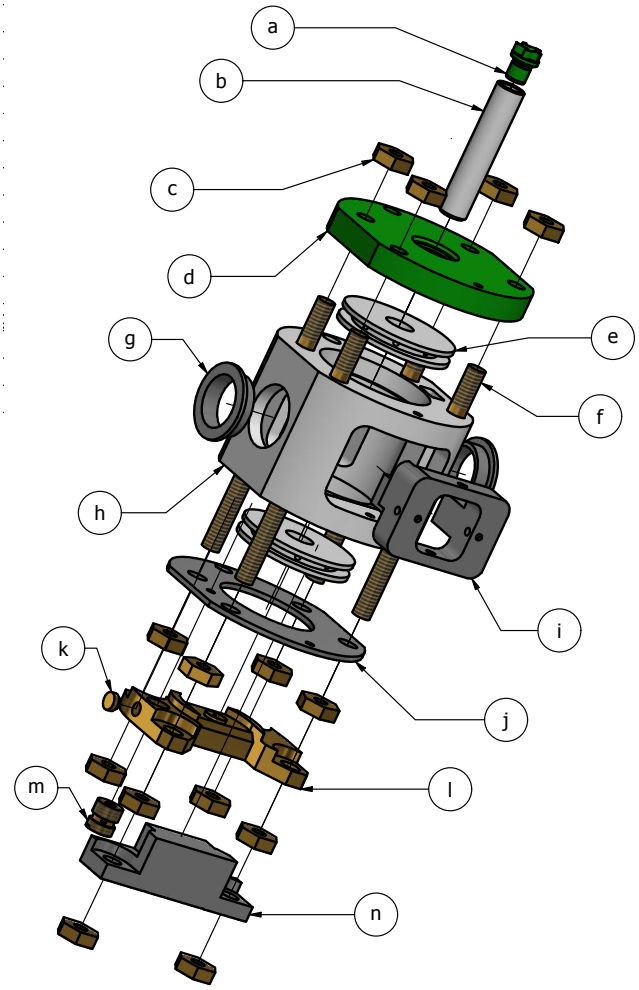

Figure 2.1: Exploded view of the 3.2 mm MAS stator assembly. The components of the stator assembly are: (a) drive cap, (b) MAS rotor, (c) brass nut, (d) drive plate, (e) radial bearing, (f) threaded rod, (g) gas inlet bushing, (h) stator body, (i) coil block, (j) bottom plate, (k) axial bearing plate cap, (l) axial bearing plate, (m) Bernoulli valve, and (n) fiber optic block.

The axial bearing plate cap (Figure 2.1k) and the Bernoulli valve (Figure 2.1m) were CNC machined out of 360 brass by 3DHubs (Amsterdam, NL). The axial bearing plate (Figure 2.1l) was machined from 260 brass by Protolabs and required some additional in-house machining, including machining the exit hole for the axial bearing gas. The cap for the axial bearing plate was sealed to the plate with epoxy. During assembly of all the stator components, a precision gauge pin was used to assist with alignment of the bearings, drive plate, and RF coil. A thin coating of epoxy was used to adhere the drive plate, bottom plate, and gas inlet bushings to the zirconia stator in order to create a hermetic seal at these interfaces. For stator repairs, disassembly is simple, usually requiring only a 30-60 minute soak in acetone or other epoxy dissolving solvent to remove the damaged piece.

2.3.2 Stator & Rotor Testing Setup

A dedicated station was constructed for testing the 3.2 mm MAS system without the risk of damaging other probe components. Using the test station, the position of the Bernoulli valve in the axial bearing plate was manually adjusted via an iterative process. The purpose of the Bernoulli valve is to regulate air flow to the axial bearing plate, which simultaneously levitates the rotor on a bed of air and generates a Bernoulli effect at its base to prevent the rotor from ejecting from the stator.

Two separate but functionally identical stators were independently used to test spinning and experimental performance. The first stator was mounted on the test station (Figure 2.2a,b) and was used to perform spin tests to observe the long-term stability of the MAS stator and drive caps. For all spin tests, the rotor was fully packed with finely ground KBr powder and equipped with a 3D printed drive cap. Seven different drive caps were spin tested for a period of at least one week over a range of spinning frequencies. Since the primary objective of these tests was to determine

how robust the stator and drive caps were over an extended period of time, the choice was made to perform these tests in the absence of an RF coil. Spinning regulation was performed using a Bruker (Billerica, MA) MAS I spin controller, and spinning data was recorded using a custom Python program designed to record the spinning frequency approximately once per second.

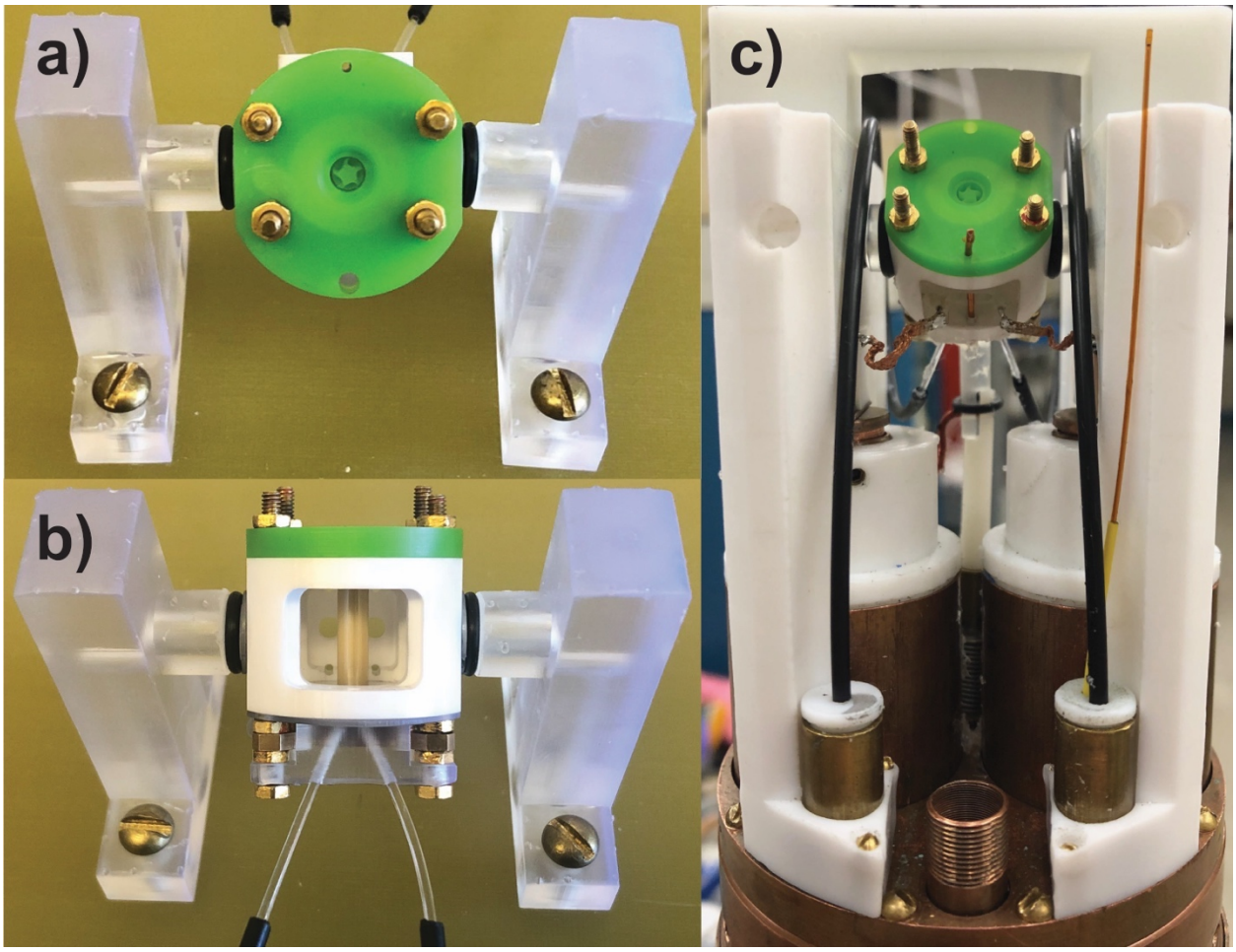

Figure 2.2: (a) Top and (b) front view of assembled stator and rotor on home-built spinning test station. (c) Assembled stator mounted on a triple-resonance $^{1}H/^{13}C/^{15}N$ NMR probe.

The second stator was retrofitted to a $\omega_{0H}/2\pi$ = 500 MHz $^{1}H/^{13}C/^{15}N$ triple-resonance NMR probe (Figure 2.2c)[77] to measure the performance of the stator during MAS NMR experiments. A series of 2D ^{13}C-^{13}C correlation spectra were recorded on a sample of U-$^{13}C/^{15}N$ aspartic acid, demonstrating sufficient system stability over the duration of the experiments. Spinning regulation for the probe-mounted stator was controlled with a Bruker MAS I controller.

2.4 Results & Discussion

Additive manufacturing is a convenient, quick, and low-cost method that enables both rapid in-house replacement of damaged stator components following rotor crash events as well as customization of MAS stator assemblies for specific laboratory needs. During testing of our 3D printed parts, we found that our MAS stators and drive caps proved to be durable and comparable to commercially available components. A summary of the performance of the 3D printed drive caps can be found in Table 2.1. For every drive cap tested, the standard deviation in the spinning frequency was observed to be less than 2 Hz. Furthermore, the stability of the tested drive caps was remarkably consistent over the entire set. For a batch of 20 3D printed drive caps, the cost per drive cap was ~$20, making them very affordable for most NMR researchers.

Table 2.1: Summary of 3D Printed Drive Cap Performance

Drive Cap	Test Duration	ν_r (Hz)	μ (Hz)[a]	σ (Hz)
1	3 Months	15000	15000.03	1.6979
2	1 Week	18000	18000.04	1.4907
3	1 Week	18000	18000.03	1.5258
4	1 Week	18000	18000.05	1.4575
5	1 Week	20000	20000.02	1.6818
6	1 Week	20000	20000.02	1.4662
7	1 Month	20000	20000.04	1.6379

[a] Mean MAS frequency values are reported to first non-zero digit.

Experimental performance of the 3D printed stator components and drive tips was verified during acquisition of a 2D ^{13}C-^{13}C Dipolar-Assisted Rotational Resonance (DARR)[78] spectrum recorded on a sample of U-^{13}C/^{15}N aspartic acid as seen in Figure 2.3. Notably, magnetic field

homogeneity was preserved in the presence of previously mentioned stator components, as evidenced by observable peak splitting from J-couplings.

While prices will vary depending on quantity and design, a conservative estimate of the total production cost for a few MAS stators is less than $2,500 per stator. This number does not include the capital costs of purchasing a 3D printer, however user access to quality 3D printers has become more prevalent, especially at academic research institutions. Due to the small size of the parts, the cost associated with 3D printing stator components on the Form 3 printer was negligible. An estimate of the total cost to machine all the brass components as well as 3D print the drive plate and zirconia stator body is less than $1,000. Therefore, the largest cost associated with fabricating these stators is the unavoidable machining costs for the zirconia bearings and bearing counterbores.

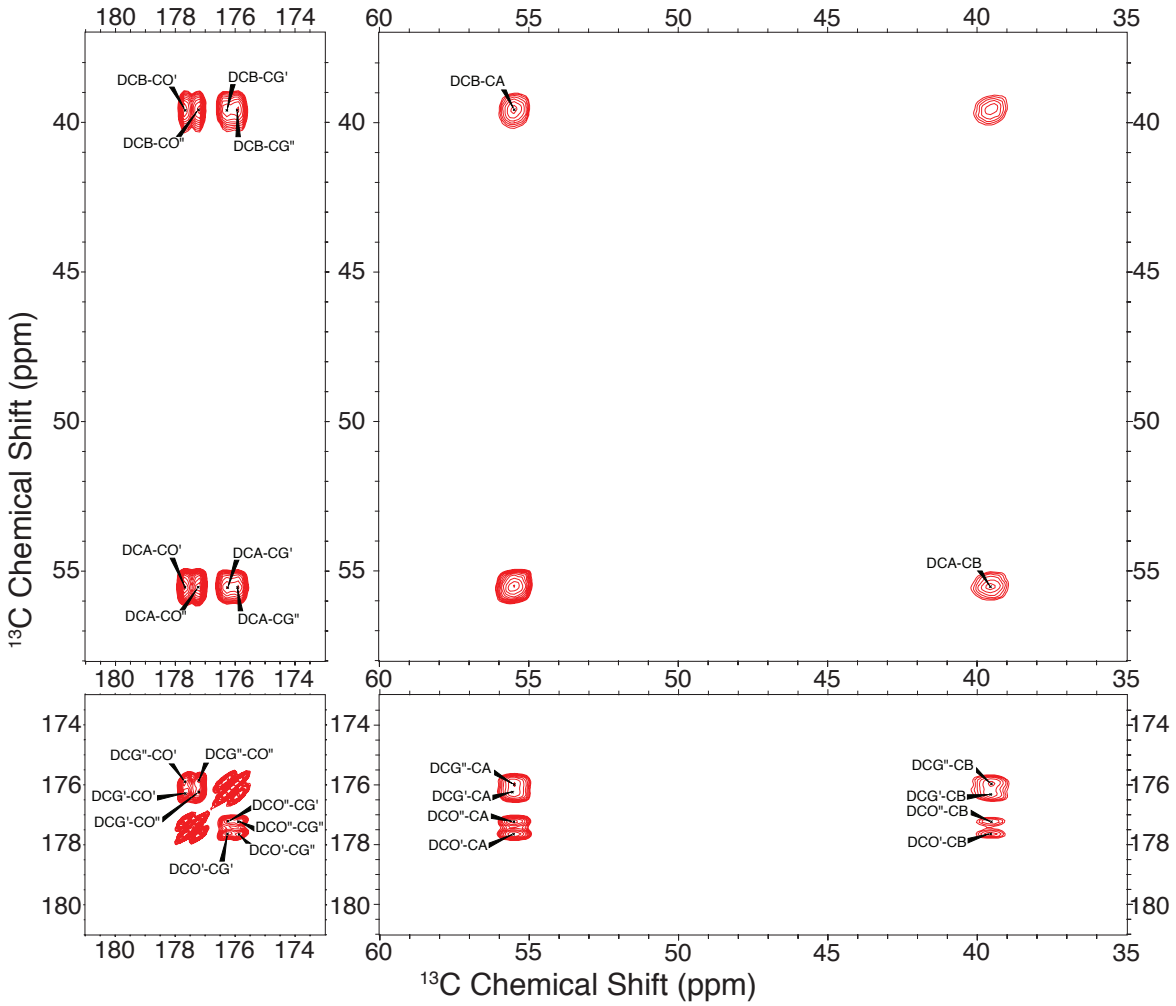

Figure 2.3: 2D ^{13}C-^{13}C DARR (τ_{mix} = 100 ms) spectrum of U-^{13}C,^{15}N aspartic acid recorded at $\omega_{0H}/2\pi$ = 500 MHz and $\omega_r/2\pi$ = 20 kHz ± 5 Hz. The DARR spectrum was recorded in two separate blocks of 8 scans per FID and the spectra were added for a total of 16 scans per FID. The total experimental time was ~27 hrs. Spectrum was referenced to the downfield peak of adamantane relative to DSS. Prime (′) and double prime (″) notation in peak labels indicates peak splitting due to J-couplings.

2.5 Conclusions

We have developed novel methods for fabricating 3D printed MAS stators and demonstrated that the performance of these stators is reproducibly comparable to commercially available stator systems. These methods are a reliable and inexpensive approach for researchers to produce components for MAS NMR probes. As additive manufacturing technology continues to develop, the range of NMR components that can be 3D printed will continue to expand and may provide researchers with the opportunity to explore new designs for MAS components that were

previously considered impractical. Future additive manufacturing studies include scaling these methods for smaller rotor systems and observing the performance of these stators under harsher experimental conditions such as the cryogenic temperatures used in dynamic nuclear polarization experiments.

2.6 Chapter-Specific Acknowledgements

We would like to thank Peter Gor'kov for providing us with helpful preliminary stator drawings as well as David Lewis for helpful correspondence in troubleshooting the stators' performance. Additionally, we would like to thank Ajay Thakkar, Michael Mullins, and Stephen Thomson for their help with machining components for this study and for helpful discussions regarding troubleshooting the stators' performance. This work was supported by grants from the National Institutes of Health, NIGMS under grants GM132079 and GM132997. Natalie Golota is supported by the National Science Foundation Graduate Research Fellowship under Grant No.1745302.

3 Bound Water & Polymorphism Studies on the Amyloid-Forming Peptide GNNQQNY

3.1 Abstract

GNNQQNY, a seven residue peptide found in the prion-forming domain of the protein Sup35, is an ideal model system for the study of amyloid polymorphism. Its short size allows for excellent sensitivity and resolution in MAS NMR experiments, and by varying the aggregation conditions, the peptide can be directed to reproducibly form amyloid-like fibrils or microcrystals. In this chapter, we discuss procedures for synthesizing U-^{13}C,^{15}N GNNQQNY microcrystals and fibrils and present preliminary NMR data on both systems. These studies hew a foundation for future insight into interactions and interfaces in critical and complex biological systems.

3.2 Introduction & Motivation

3.2.1 ^{17}O Experiments on Bound Water

Water plays a key role in numerous biological processes including protein folding and dynamics, but it remains difficult to study via NMR. This can be attributed to the fact that ^{17}O is a quadrupolar nucleus with low natural abundance (~0.037%) and a low gyromagnetic ratio ($0.14\gamma_H$). Recent work has shown that high-resolution structural information can be obtained on ^{17}O water in both organic and inorganic crystals.[22, 79, 80] An example of this can be seen in Figure 3.1 in which an MQMAS experiment was used to resolve all four water sites in a crystal of lanthanum magnesium nitrate hydrate (LMN).[22] Although tremendous progress has been made in the development of techniques for studying ^{17}O in bound water, a measured effort has not yet been made to extend these techniques to larger peptide systems.

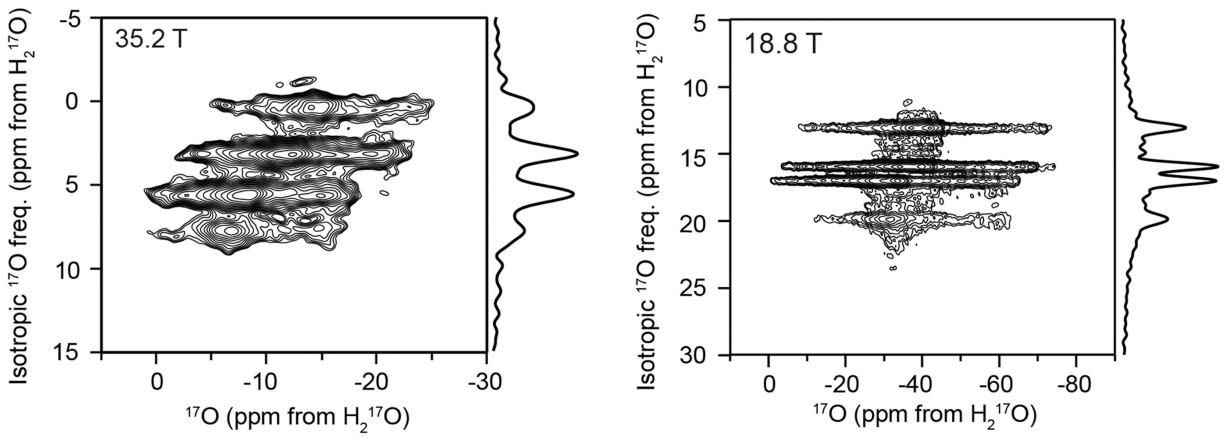

Figure 3.1: ^{17}O MQMAS spectra of LMN recorded at (left) 35.2 T and (right) 18.8 T. All four water sites in the LMN crystal can be clearly resolved. Reprinted with permission.[22]

3.2.2 Amyloids & Polymorphism

Amyloid fibrils have been linked to a range of debilitating diseases including Alzheimer's disease,[81, 82] Parkinson's disease,[83, 84] and dialysis-related amyloidosis[85, 86] among others. Generally, amyloid fibrils have similar structural characteristics including a "cross-β" pattern that is observable in X-ray fiber diffraction studies. This cross-β pattern indicates an inter-strand spacing of 4.7 Å between the strands of β-sheets along the fibril axis and a 10 Å inter-sheet distance between the β-sheets in a protofilament. Amyloid fibrils are typically composed of several protofilaments and are resistant to degradation. Because amyloid fibrils are heterogeneous and insoluble, techniques such as MAS NMR and cryogenic electron microscopy (Cryo-EM) are best suited for their study.

Despite the similar characteristics that amyloid fibrils share, structural polymorphism is present in numerous amyloid fibril systems.[87, 88] Generally, polymorphism in amyloid fibrils can occur at three different levels. First, the substructure of the protofilament may vary between different polymorphs. Second, the number of individual protofilaments present in the mature fibril could impact the structure of the fibril. Finally, the arrangement of individual protofilaments may

also affect the structure of the fibril. Determining structural differences between fibril polymorphs is vital, as even small structural variations can greatly impact the effectiveness of drugs and other therapeutic agents used to treat the underlying diseases associated with these amyloids.

3.2.3 Overview of GNNQQNY

GNNQQNY is short peptide fragment located in the prion-forming domain of the protein Sup35. A unique aspect of GNNQQNY is that, despite its short length, it is able to form fibril structures that exhibit similar characteristics to amyloid fibrils including a cross-β diffraction pattern, binding of Congo red, and excellent structural stability. Additionally, Nelson et. al. demonstrated that under the right conditions GNNQQNNY can form amyloid-like microcrystals.[89] X-ray diffraction data reveal that these microcrystals exhibit a parallel, in-register β-sheet conformation along the entire length of the elongated crystal. Between the β-sheets are alternating wet and dry interfaces that are defined by the presence or absence of water molecules.

MAS NMR has been used to study the structure of both the microcrystals and fibrils.[90-92] An interesting finding of MAS NMR studies of GNNQQNY amyloid fibrils is the apparent presence of three distinct polymorphs. This is indicated in Figure 3.2, as the cross peaks of the crystal 2D spectra split into three separate sets of cross peaks in the fibril spectra. Integration of the 2D cross peaks reveals that the polymorphs appear to be present in an approximately 1:1:1 ratio, and the formation of these fibrils has been shown to be reproducible. The observation of three distinct sets of chemical shifts implies that there are also three unique structures for the amyloid fibrils.

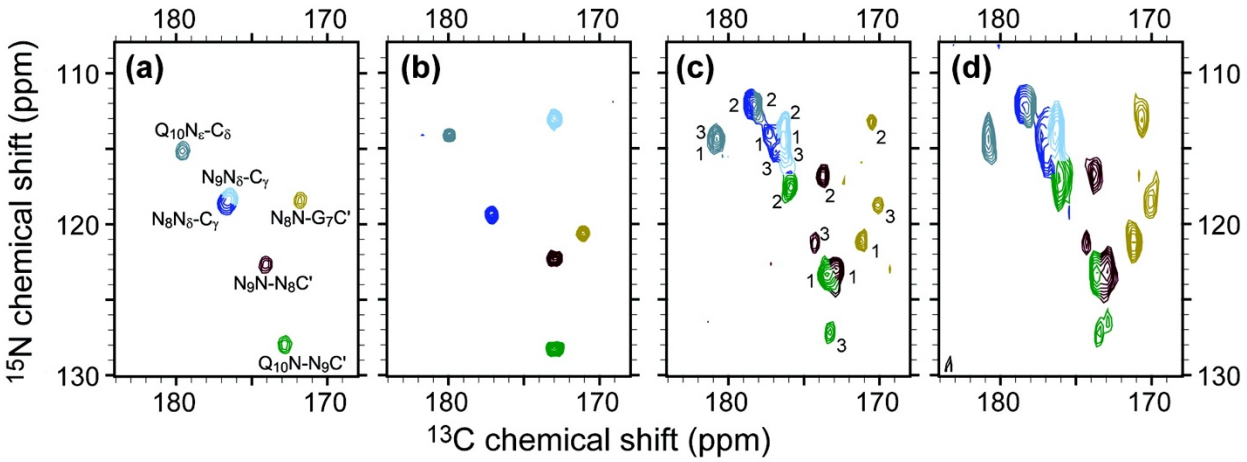

Figure 3.2: 2D ^{13}C-^{15}N spectra of various [U-^{13}C,^{15}N-GNNQ]QNY morphologies. (a) Monoclinic crystals, (b) orthorhombic crystals, (c) 100%-labeled amyloid fibrils at 20 mg/ml and (d) 25%-labeled amyloid fibrils at 25 mg/ml. Spectra were recorded at (a) $\omega_{0H}/2\pi$ = 500 MHz and (c-d) $\omega_{0H}/2\pi$ = 700 MHz, respectively. Reprinted with permission.[90]

DNP experiments have also been performed on both the GNNQQNY microcrystals and amyloid fibrils.[93, 94] GNNQQNY crystals are a model system for DNP experiments for a variety reasons. First, the crystals are extremely stable and difficult to dissolve, so the GNNQQNY microcrystals can therefore be easily dispersed in most DNP matrices including DNP juice. Second, GNNQQNY is a relatively rigid system. There are very few functional groups that undergo motion (i.e. methyl hopping) that could lead to fast relaxation in GNNQQNY microcrystals and thus decreased DNP enhancements. This is especially true for the monoclinic crystals, where the tyrosine ring remains rigid, compared to the orthorhombic crystals, where the ring undergoes flipping. Finally, the water pores of the microcrystals are too small for most radicals to penetrate. This limits paramagnetic broadening to the nuclei present near the surface of the crystal and significantly improves the resolution of DNP spectra. Furthermore, high DNP enhancements are still achievable via ^{1}H-^{1}H spin diffusion between nuclei on the surface of the crystal and those in the bulk.

3.2.4 Motivation for Current Study

This chapter focuses on the use of GNNQQNY as a model system for the study of bound water in biological systems and polymorphism in amyloid fibrils. The unit cell structure of monoclinic GNNQQNY crystals is seen in Figure 3.3. From X-ray diffraction data, it is known that there are seven chemically distinct bound water sites in the monoclinic crystal structure.[89] Based on previous work by Keeler et. al.,[22] adding additional dimensions to MAS experiments such as MQMAS may enable the resolution of all seven water molecules in the crystal structure. The inefficiency of MQMAS experiments coupled with the low sensitivity of ^{17}O and the need for higher-dimensional experiments requires gains in sensitivity that can only be achieved with novel DNP techniques. The excellent sensitivity and resolution observed on GNNQQNY crystals under DNP conditions make this system an ideal candidate for method development. The techniques developed on GNNQQNY will serve as a foundation for future high-resolution ^{17}O-^{13}C, ^{17}O-^{15}N, and ^{17}O-^{1}H correlation experiments on more complex biological systems.

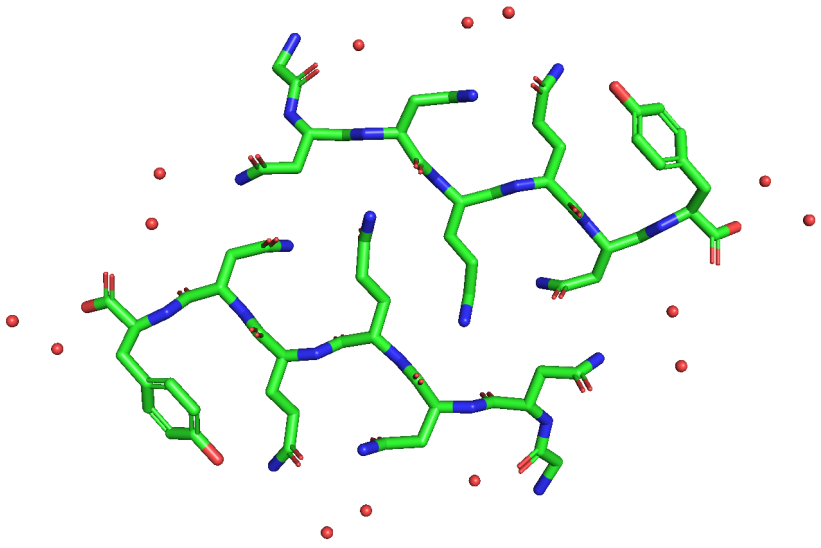

Figure 3.3: Unit cell of monoclinic GNNQQNY crystals. There are seven chemically distinct water molecules in the crystal structure. Structure taken from Protein Data Bank (PDB ID:1YJP).[89]

Given the impact that amyloid polymorphism has on the development of drugs and other therapeutic agents, gaining a better understanding the structural differences between amyloid polymorphs is of vital importance. Polymorphism is often observed in NMR spectra, but it is often difficult to determine how observed spectroscopic differences translate to structural differences in polymorphs. The study of polymorphism in most amyloid fibril systems is additionally challenging due to the variability in observed polymorphs from sample to sample, and poor resolution and sensitivity in polymorphic systems makes spectral analysis an onerous task.

Using GNNQQNY as a model system for studying polymorphism in amyloid fibrils circumvents several of these challenges. GNNQQNY is a small peptide and thus has excellent sensitivity in MAS NMR experiments; the formation of three distinct fibril forms can be observed in approximately equal ratios, and the formation of these three forms is highly reproducible; and despite the degeneracy in the peptide sequence, the GNNQQNY polymorphs have excellent resolution in the nitrogen dimension, making it easier to assign and analyze NMR spectra. While it was previously cost-prohibitive to synthesize U-^{13}C,^{15}N GNNQQNY, using a uniformly labeled sample, it is now possible to perform a full structure calculation of the three GNNQQNY fibril forms. This calculation can then be used to gain insight into polymorphism in other amyloid fibril systems as well.

3.3 Methods

3.3.1 GNNQQNY Expression via Recombinant Methods

Initial explorations into synthesizing U-^{13}C,^{15}N GNNQQNY via peptide synthesis were discouraging. Most peptide synthesis companies required a five times molar excess of the amino acids that were to be coupled via solid-phase peptide synthesis. For U-^{13}C,^{15}N labeled amino acids with protecting groups, this amount of starting material is prohibitively expensive given the overall

yield of the synthesis after purification. Instead, attempts were made to express U-^{13}C,^{15}N GNNQQNY recombinantly.

A convenient way to recombinantly express and purify proteins is via a fusion partner. In this case, a mutant version of the autoproteolytic protein N^{pro} was used as a fusion partner for synthesis of U-^{13}C,^{15}N GNNQQNY. The mutant of the N^{pro} protein used in this case is known as the EDDIE mutant.[95, 96] One of the benefits of the N^{pro} fusion partner is that when it refolds, it cleaves itself from the peptide of interest and generates peptides with authentic N-termini. An example of this can be seen in Figure 3.4. The amino acid sequence for GNNQQNY with the N^{pro}(EDDIE) fusion partner is:

MELNHFELLY	KTSKQKPVGV	EEPVYDTAGR	PLFGNPSEVH	PQSTLKLPHD	50
RGEDDIETTL	RDLPRKGDCR	SGNHLGPVSG	IYIKPGPVYY	QDYTGPVYHR	100
APLEFFDETQ	FEETTKRIGR	VTGSDGKLYH	IYVEVDGEIL	LKQAKRGTPR	150
TLKWTRNTTN	CPLWVTSCGN	NNQQNY	176		

Cleavage of the N^{pro}(EDDIE) fusion partner and GNNQQNY occurs between Cys168 and Gly169.

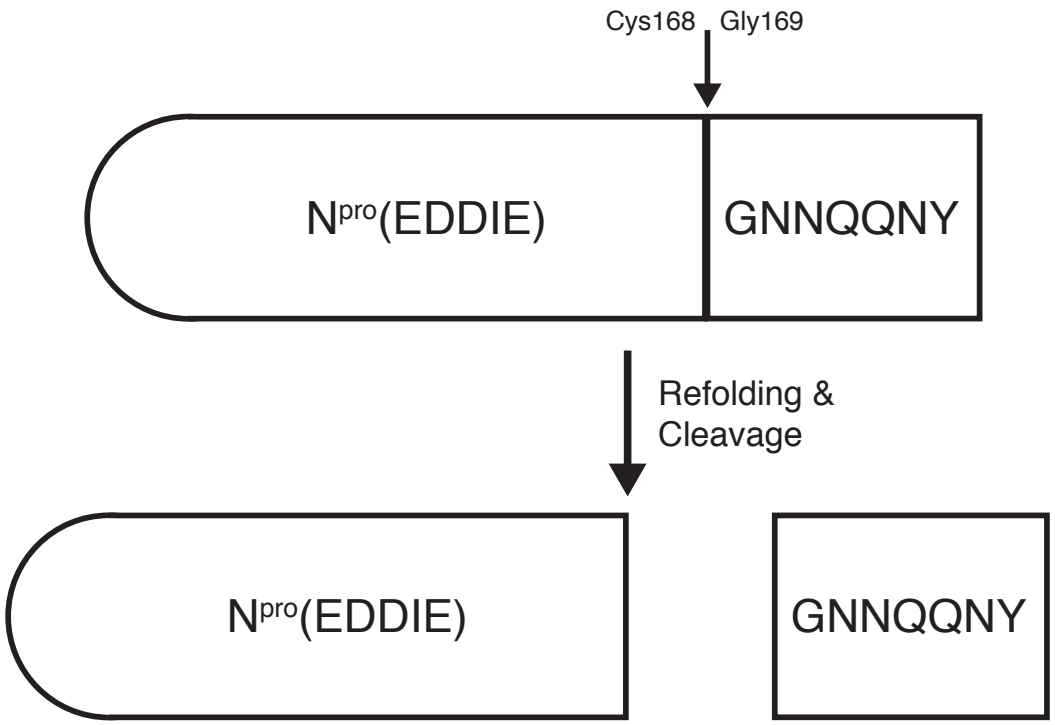

Figure 3.4: Schematic representation of GNNQQNY cleavage from N^{pro} fusion partner.

A vector containing the gene for the N^{pro}(EDDIE) fusion protein with GNNQQNY was inserted into a plasmid of *E. coli* BL21(DE3) cells. This plasmid also contained a gene for ampicillin resistance. For the purpose of troubleshooting the synthesis all materials used for protein expression were natural abundance. A pre-culture of the *E. coli* cells was grown overnight in Lysogeny broth (LB) containing ampicillin. The pre-culture was then divided evenly among 6 larger, 1 L flasks containing LB and ampicillin for the main growth. Both the pre-culture and main culture were grown in autoclaved flasks using an incubator shaker at 37°C. At an OD_{600} of 0.6-0.8, the cells were induced with 1 mM IPTG to begin protein production. The cells were harvested after a period of 3-4 hours.

The inclusion bodies were purified by repeated sonication in a buffer containing Triton-X100 followed by centrifugation. The N^{pro}(EDDIE) protein was then prepped and purified via FPLC using anion-exchange columns. The eluted protein was centrifugally concentrated and then

diluted dropwise by a factor of 1:20 in an appropriate refolding buffer. By concentrating the protein prior to refolding, the volume of the refolding buffer can be significantly decreased. The refolding buffer consisted of 1M Tris-HCl, 500 mM NaCl, 1 mM EDTA, and 3 mM DTT at pH 8.5. Confirmation of the GNNQQNY cleavage was performed via SDS-PAGE analysis.

The refolding buffer containing the cleaved GNNQQNY as well as the N^{pro}(EDDIE) was then concentrated in a rotary evaporator and prepped for dialysis to decrease the concentration of buffer components in solution. After a few rounds of dialysis, the N^{pro}(EDDIE) and GNNQQNY were lyophilized and prepped for RP-HPLC purification. During dialysis, there appeared to be signs of protein aggregation, as white clumps formed within the dialysis tubing. In order to perform RP-HPLC, a suitable solvent needed to be identified that would both dissolve aggregated GNNQQNY and be compatible with HPLC purification. The solubility of lyophilized GNNQQNY was tested for a variety of solvents. A summary of these results is seen in Table 3.1.

Table 3.1: Summary of GNNQQNY Solvents

Solvent	Soluble?	Notes
10 M NaOH	Yes	-
Water	Yes	Dissolves under high heat. Recrystallizes upon cooling down.
DMSO	No	-
DMSO & Triethylamine (TEA) or DMSO & Trimethylamine (TMA)	Yes	Dissolves at pH ~9-10 at room temperature.
DMSO & TFA	Yes	Dissolves at pH = 4 at room temperature.
Acetonitrile & TFA	Yes	Appeared to dissolve at room temperature after a few hours.

Although suitable solvents for HPLC capable of dissolving GNNQQNY were successfully identified, purification of the recombinant GNNQQNY via HPLC was unsuccessful. Several analytical HPLC runs were performed in which the lyophilized recombinant material was

compared to a GNNQQNY standard, and in each case, elution of the standard was clearly observable while elution of GNNQQNY from the recombinant material was undetectable. At this time, it is unclear why HPLC purification remains ineffective.

3.3.2 Peptide Synthesis of GNNQQNY

Because of the poor purification results with the N^{pro}(EDDIE) fusion tag, the use of solid-phase peptide synthesis was revisited. For natural abundance GNNQQNY material, Genscript (Piscataway, US) was able to synthesize large quantity (~1 g) batches at reasonable costs. For U-^{13}C,^{15}N GNNQQNY material, a synthesis was attempted using a smaller quantity of U-^{13}C,^{15}N protected amino acids. Using a manual coupling procedure and solvents such as NMP rather than DMF, the coupling yields were greatly improved. Solid-phase peptide synthesis of U-^{13}C,^{15}N GNNQQNY was performed on a 0.1 mmol scale. The manual coupling method required only a two-fold excess (0.2 mmol) of all amino acids except tyrosine, which required only 0.1 mmol of pre-loaded resin. Typically, a yield of 30-40 mg of U-^{13}C,^{15}N GNNQQNY was achieved after final HPLC purification.

3.3.3 Crystallization Procedure

GNNQQNY will form crystals at concentrations below 10 mg/ml. Provided that the concentration remains below 10 mg/ml, the only effect that concentration appears to have on the formation of crystals is the speed at which crystallization takes place. The procedure used to produce monoclinic crystals of GNNQQNY is straightforward and similar to procedures laid out in previous work.[90] First, high-purity (>98%), lyophilized GNNQQNY is dissolved in hot (>90°C) Milli-Q water at the desired concentration. Once the peptide is fully dissolved, it is drawn into a small volume syringe and then rapidly filtered through a ≤0.22 μm syringe filter to assist with removal of fibrilization sources. Due to the high concentration of peptide in solution, back pressure

would often build up in the syringe during filtration of the sample. This would occasionally result in leakage of the sample through the syringe plunger. This issue was eliminated by switching to a gas-tight syringe. Volume loss due to retention by the syringe filter was accounted for by adding water to achieve to the original solution volume.

After filtration, the peptide solution was chilled in a refrigerator at 4°C for a period of at least 24 hours to allow the sample to crystallize. The solution can be seeded with a dilute concentration of monoclinic GNNQQNY crystals to reduce crystallization time and promote the formation of the desired crystal form. At concentrations close to 10 mg/ml, the formation of crystals was often observable within a few hours.

3.3.4 Fibrillization Procedure

Excluding the filtration step, the procedure for synthesizing GNNQQNY fibrils is nearly identical to the procedure used to form GNNQQNY crystals. To produce GNNQQNY fibrils, the lyophilized peptide was dissolved at very high concentrations (≥25 mg/ml) in hot (>90°C) Milli-Q water. Once the peptide appeared to dissolve fully, the solution was placed in a refrigerator at 4°C overnight. Formation of fibrils is rapid, due at least in part to the high solution concentration. The resulting solution after fibrilization was viscous with a gel-like appearance. Given the difficulty in dissolving the peptide at such high concentrations, it was common to also observe the formation of a few very small crystals as well. The formation of crystals in the fibril solution could be reduced by seeding the solution with a small amount of pre-made fibril solution.

3.3.5 Distillation Apparatus for Recovery of ^{17}O Water

Many methods for the ^{17}O-labeling of biomolecules require the use of ^{17}O-enriched water as a precursor.[97] Because of the many challenges associated with synthesizing ^{17}O-enriched water,

such labeling procedures can be exorbitantly expensive and difficult to scale. As an example, the cost of 90%-^{17}O water from Cambridge Isotope Laboratories (Andover, US) is $1,700/ml. The concentration limits for formation of GNNQQNY crystals require the concentration to be kept below 10 mg/ml, so producing ~30 mg of GNNQQNY crystals containing ^{17}O-enriched water would cost >$5,000. It is therefore highly advantageous to recover ^{17}O water after GNNQQNY crystallization so that it can be reused for subsequent crystallizations.

To recover ^{17}O-enriched water after crystallization, the distillation apparatus depicted in Figure 3.5 was constructed. After producing GNNQQNY crystals, the crystals may be spun down in a centrifuge, and the excess water can be drawn off. This water contains GNNQQNY that was unable to crystallize as well as small GNNQQNY crystals that were not fully spun down by the centrifuge. In order to make a pure solution of GNNQQNY crystals, both the peptide and solvent must also have high purity. Therefore, in order to reuse the ^{17}O-enriched water for additional crystallizations, the water had to be purified to a high level by the distillation apparatus.

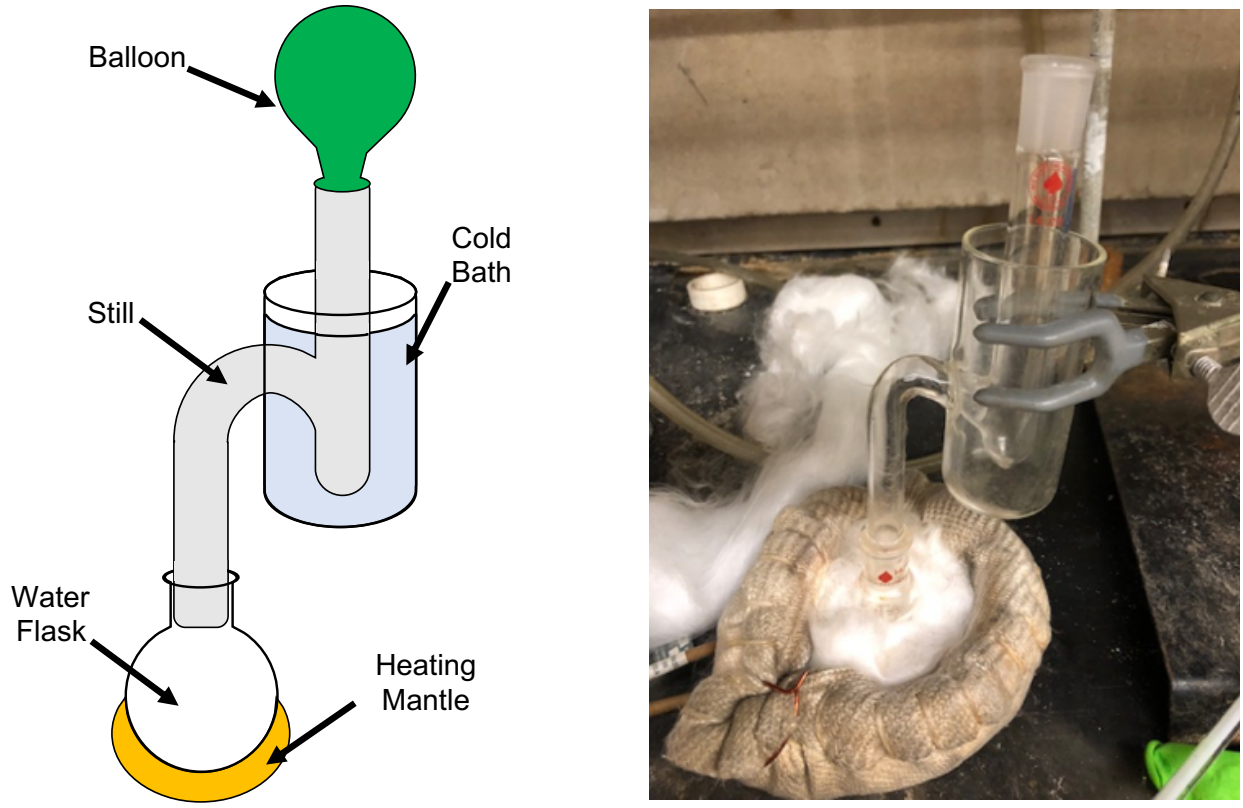

Figure 3.5: (Left) Schematic representation of water distillation apparatus. (Right) Picture of water distillation apparatus.

The distillation apparatus seen in Figure 3.5 consisted of a pear-shaped flask attached to a miniature still purchased from Ace Glass (Vineland, US). The flask contained the drawn off water following centrifugation of the GNNQQNY crystals. The flask was placed in a heating mantle and wrapped in glass wool to thermally insulate it from the rest of the still. The heating mantle was heated to ~100°C to slowly evaporate the water in the flask. Condensation of the water in the still was accomplished using a bath of dry ice and acetone. Throughout the distillation, dry ice was added in regular intervals to keep the still at low temperature. A balloon was added to the top of the still to minimize evaporation of distilled water as well as the exchange of ^{17}O-enriched water with water vapor in the atmosphere.

The best distillation results were achieved by taking a "low and slow" approach. The lower the temperature was kept during distillation, the purer the recovered water was at the end. Towards

the end of the distillation, a butane torch was used to gradually heat the still's stem to evaporate any remaining water. Additional crystallization attempts using the distilled water demonstrated that the recovered water was of high enough purity to successfully produce additional GNNQQNY crystals without the need to purchase additional ^{17}O-enriched water.

3.3.6 NMR Experiments

A suite of NMR experiments was performed on both monoclinic GNNQQNY crystals and fibrils. The procedure for synthesizing monoclinic GNNQQNY crystals and GNNQQNY fibrils can be found in Sections 3.3.3 and 3.3.4, respectively. All room temperature samples were packed into Bruker 3.2 mm rotors using an SW-60 ultracentrifuge rotor and custom centrifugal packing tool. DNP samples were packed in 3.2 mm RevNMR rotors using a tabletop centrifuge. Prior to packing, the DNP samples were resuspended in a mixture of DNP juice (60/30/10 v/v/v, glycerol-d_8/D_2O/H_2O) with 10 mM AMUPol.

3.4 Results & Discussion

3.4.1 Monoclinic Crystals

Before crystallizing uniformly labeled samples, confirmation was required that the GNNQQNY crystals were the correct form and that the resolution was comparable to previously obtained crystals.[90] A natural abundance ^{13}C spectrum of GNNQQNY crystals was recorded and compared to previously recorded natural abundance spectra of monoclinic and orthorhombic crystals. Figure 3.2 reveals that the recorded 1D ^{13}C spectrum overlays directly with a previous monoclinic natural abundance spectrum. Furthermore, no indications of orthorhombic crystals were present in the spectra, confirming that the GNNQQNY crystals were not only the correct form, but also of high purity.

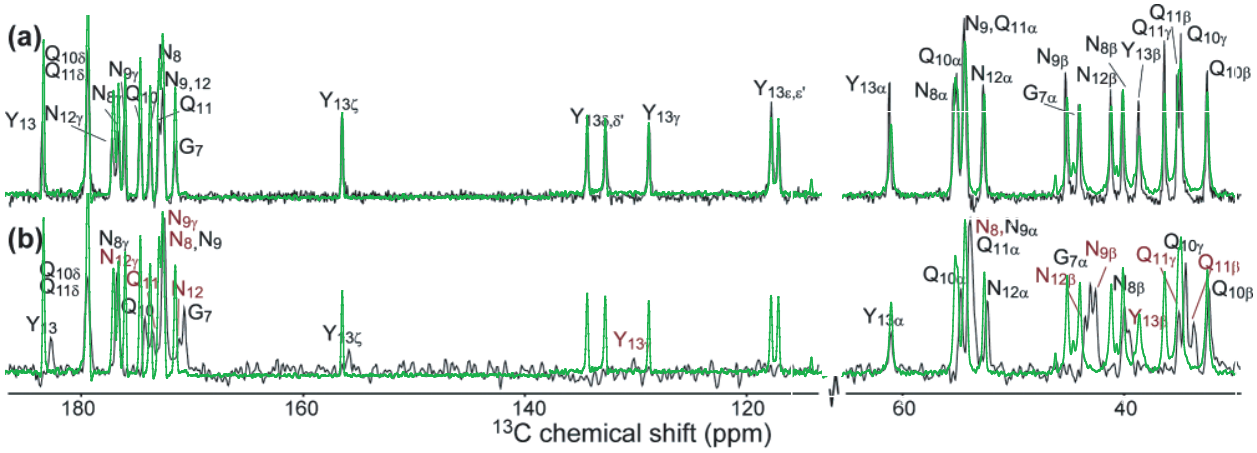

Figure 3.6: ^{13}C spectrum of GNNQQNY microcrystals recorded at $\omega_{0H}/2\pi = 900$ MHz (green) overlaid with (a) monoclinic and (b) orthorhombic ^{13}C spectra (black). Figure modified from reference.[90]

After confirming that the correct form of the GNNQQNY crystals was obtainable, three successive batches of U-^{13}C,^{15}N monoclinic crystals were synthesized. Due to a faulty power supply and MAS controller, batch one and two were unintentionally frozen during a MAS experiment. While the crystals were observed to be highly robust against heating, they were destroyed when frozen. The power supply and MAS controller were repaired, but as an additional precaution against freezing, batch three was resuspended in DNP juice without any radical. The DNP juice was intended to act as a cryoprotectant for the crystals as well as serve as a room temperature comparison for future DNP samples.

Something peculiar was observed in the 1D ^{13}C spectrum of batch three. While batch one and two produced seemingly identical spectra, batch three differed. A comparison of the 1D ^{13}C spectra is seen in Figure 3.7. Differences in batch three compared to the previous batches can clearly be seen at 170 ppm and the region between 35 and 45 ppm. The peak at 170 ppm corresponds to the glycine CO peak, while the region between 35 and 45 ppm corresponds to the glycine Cα peak as well as the Cβ peaks for all residues except glutamine. These differences in the 1D ^{13}C spectra imply that the addition of DNP juice to the crystals had an effect on their structure.

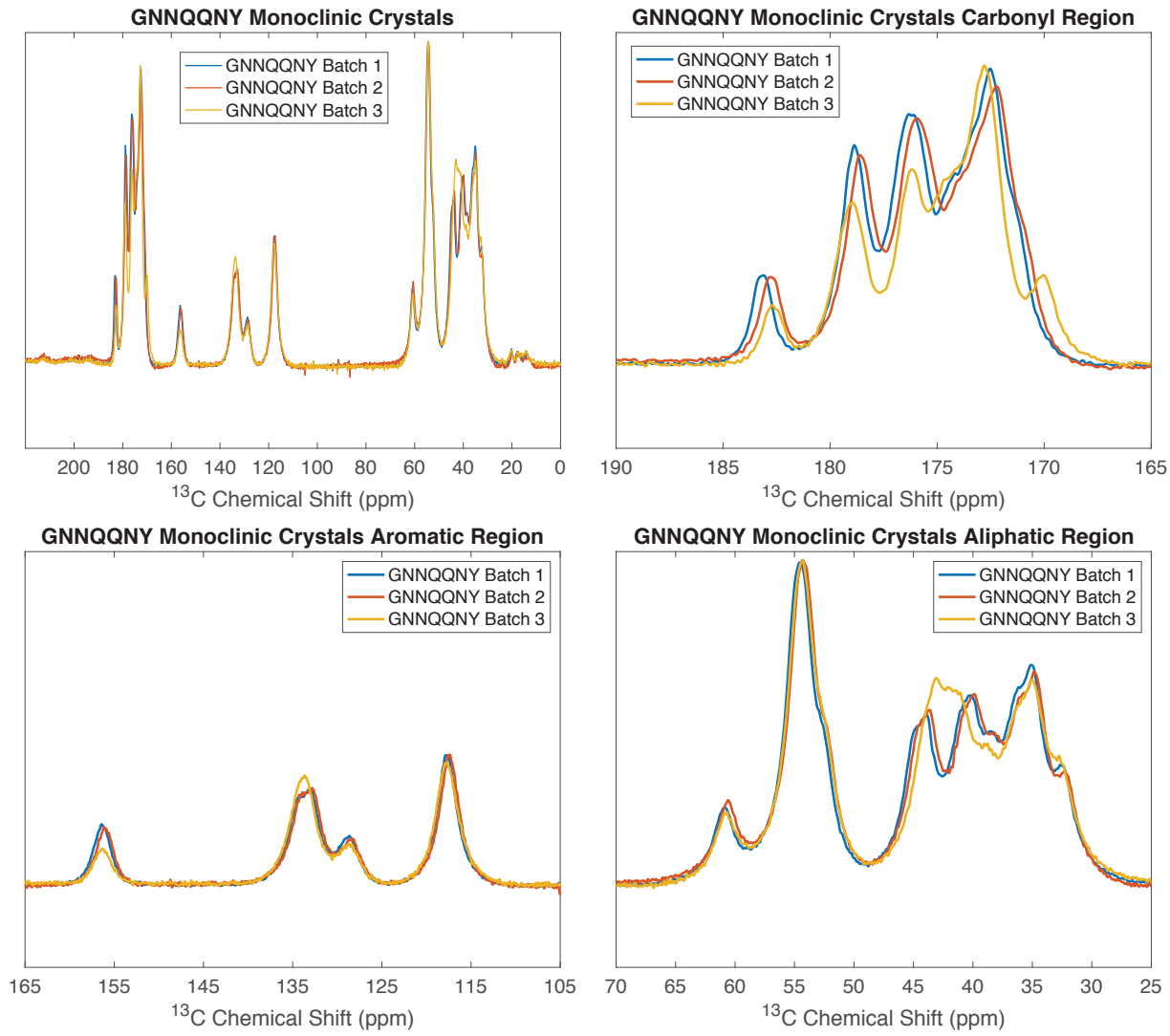

Figure 3.7: 1D ^{13}C spectra of different U-^{13}C,^{15}N GNNQQNY microcrystal batches.

Given the interesting effects that the addition of DNP juice appeared to have on the sample, DNP spectra of the crystals were recorded. A sample of U-^{13}C,^{15}N GNNQQNY crystals were packed into a rotor with DNP juice and 10 mM AMUPol. At a field of $\omega_{0H}/2\pi$ = 500 MHz, an enhancement of ε = 110 at 90 K was obtained. Furthermore, the resolution obtained on the DNP sample was comparable to the resolution obtained at room temperature at the same field. This confirms that excellent sensitivity and resolution can be achieved on GNNQQNY crystals using DNP. A 1D ^{13}C DNP spectrum can be seen in Figure 3.8.

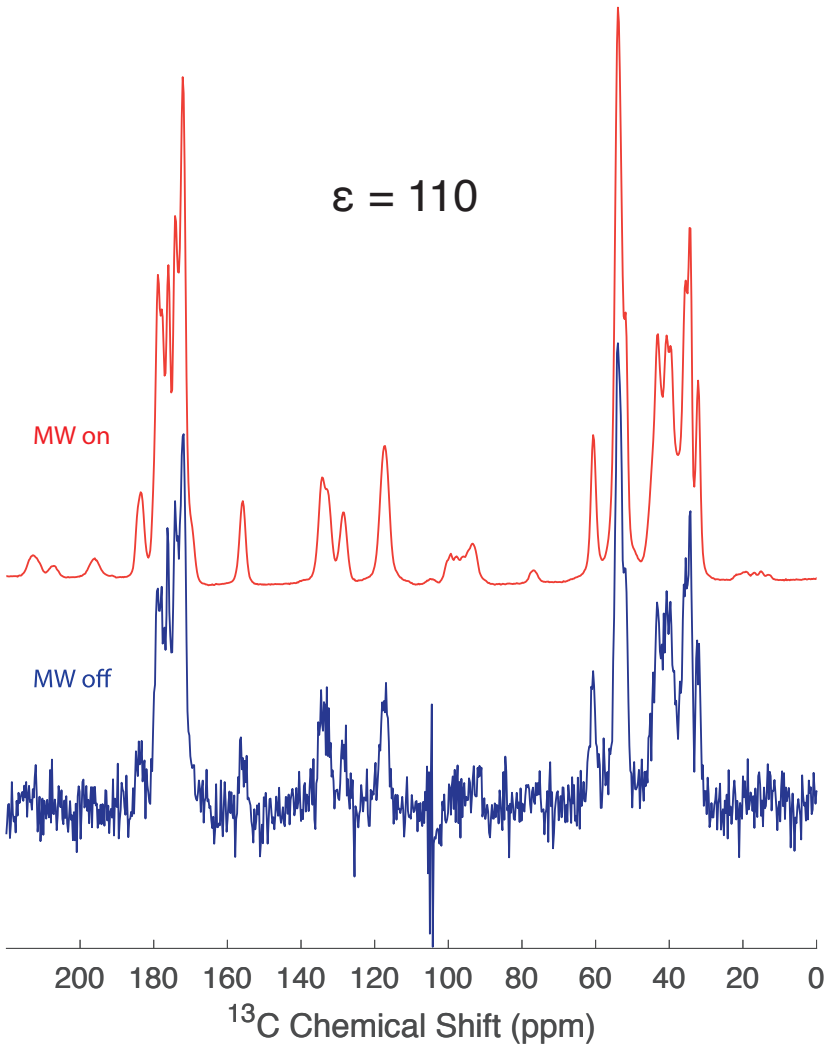

Figure 3.8: ^{13}C DNP spectrum of U-^{13}C,^{15}N GNNQQNY microcrystals recorded at $\omega_{0H}/2\pi$ = 500 MHz. The measured DNP enhancement was ε = 110 at 90 K and ν_r = 8 kHz.

Curiously, despite resuspension of the sample in DNP juice, the changes in the 1D ^{13}C spectra previously observed between the different batches at room temperature were not observed for this DNP experiment. There are two potential explanations for this. First, it is possible that DNP juice has no effect on the structure of the crystals, and batch three was altered by another external factor. Alternatively, it is also possible that DNP juice does alter the crystal structure but over a longer time scale. To avoid degradation of the radical, the DNP sample was rapidly packed using a centrifuge and then kept frozen at all times other than the insertion and ejection the rotor into the stator. It is conceivable that, as long as the sample is kept frozen, changes in the structure

of the crystal from the addition of DNP juice can be avoided. Further analysis will be needed to confirm this hypothesis.

Additional 2D spectra were recorded on batch three of the uniformly labeled crystals. One-bond RFDR[71] and ZF-TEDOR[98] spectra can be seen in Figure 3.9 and Figure 3.10, respectively. The sensitivity and resolution of the experiments were excellent. With aggressive processing, J-couplings could be resolved in the carbonyl region, indicating that the crystals are well-ordered and of high purity. Using previous assignments as a guide, preliminary assignments were performed for virtually all cross peaks in the spectra. Complete tables of assignments can be seen in Table 3.2 and Table 3.3. 3D NCOCX and NCACX spectra are required to unambiguously confirm the assignments.

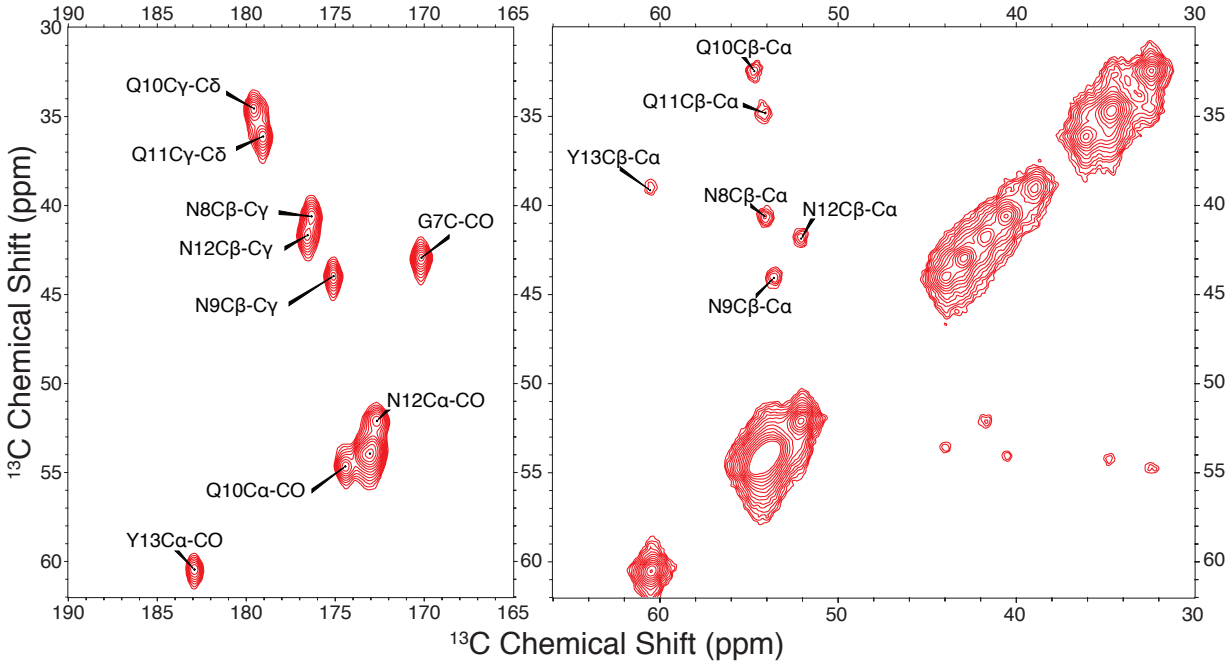

Figure 3.9: RFDR spectrum (τ_{mix} = 1.73 ms) of U-^{13}C,^{15}N GNNQQNY microcrystals recorded at $\omega_{0H}/2\pi$ = 700 MHz, T = 280 K, and ν_r = 18.5 kHz.

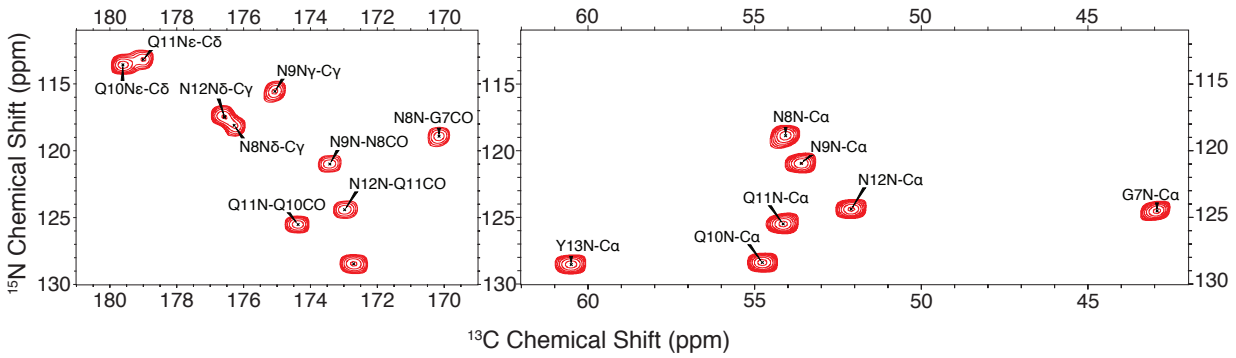

Figure 3.10: TEDOR spectrum (τ_{mix} = 1.73 ms) of U-^{13}C,^{15}N GNNQQNY microcrystals recorded at $\omega_{0H}/2\pi$ = 700 MHz, T = 280 K, and ν_r = 18.5 kHz.

Table 3.2: GNNQQNY Monoclinic Crystal ^{13}C Assignments

	Cα	Cβ	Cγ	Cδ	Cδ′	Cε	Cε′	Cξ	C
G7	42.93								170.16
N8	54.04	40.59	176.26						173.38
N9	53.61	44.08	175.10						172.83
Q10	54.69	32.46	34.54	179.58					174.44
Q11	54.16	34.79	36.12	179.06					173.01
N12	52.10	41.86	176.59						172.59
Y13	60.56	39.14	128.40	134.4	133.3	117.97	117.55	156.22	182.92

Table 3.3: GNNQQNY Monoclinic Crystal ^{15}N Assignments

	N	Nδ	Nε
G7	124.5		
N8	118.9	118.1	
N9	120.9	115.6	
Q10	128.4		113.6
Q11	125.5		113.2
N12	124.4	117.5	
Y13	128.5		

3.4.2 Amyloid Fibrils

Given the reduced sensitivity of the fibril samples and the high cost of synthesis, a 20%-dilute U-^{13}C,^{15}N fibril sample was synthesized to confirm the presence of multiple fibril forms before synthesizing a 100%-labeled fibril sample. Resolution of the different GNNQQNY fibril forms occurs primarily in the nitrogen dimension. For this reason, a one-bond ZF-TEDOR spectrum was recorded to determine the fibril forms present. Based on the ZF-TEDOR spectrum,

there appear to be at least three fibril forms present in the sample, and early observations indicate that there may be a fourth. The cross peaks around 170 ppm in the carbon dimension are indicative of glycine carbonyl peaks. The apparent peak at ~111.5 ppm in the nitrogen dimension indicates that a fourth fibril form may be present. A fourth fibril form has been observed previously, but its sensitivity was often too weak to perform any in-depth studies.[90] Further analysis on a 100%-labeled fibril sample may be need to definitively confirm the presence of this fourth form.

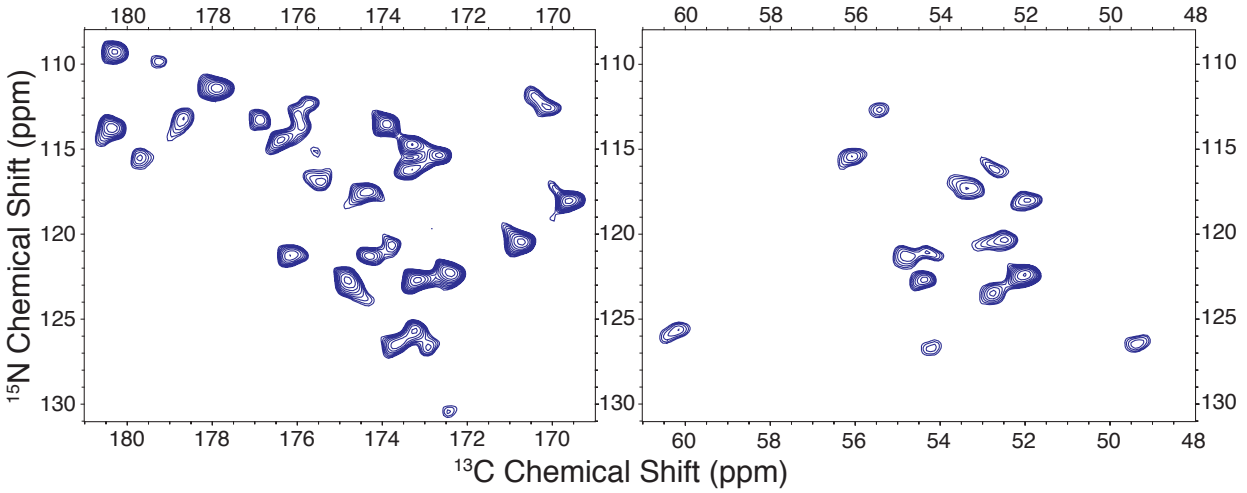

Figure 3.11: TEDOR spectrum (τ_{mix} = 1.73 ms) of 20%-U-^{13}C,^{15}N GNNQQNY fibrils recorded at $\omega_{0H}/2\pi$ = 700 MHz, T = 280 K, and ν_r = 18.5 kHz.

3.5 Future Work

Additional work must performed to achieve full structure calculations on both the GNNQQNY crystals and fibrils. In addition to confirming the assignments, the torsion angle constraints as well as distance constraints must be obtained. Due to the small size of the peptide, accurate distance constraints are especially important. To obtain these constraints, experiments such as 3D ZF-TEDOR,[98] FS-REDOR[99] and rotational resonance (R^2W)[100] experiments may be used. The fibril samples may also benefit from DNP, as higher-dimensional experiments may help resolve overlapping cross peaks.

^{17}O experiments will require crystallization of U-^{13}C,^{15}N GNNQQNY in ^{17}O water, followed by washing with non-^{17}O labeled water in preparation for DNP. Based on our previous findings regarding DNP juice, it may be essential to keep the sample frozen at all times to avoid alterations in the crystal structure. It would be beneficial to perform an experiment that tracks any potential changes in the crystal structure as a function of time to determine whether DNP juice has a perturbing effect on the structure. This is especially critical for ^{17}O experiments, as exchange of bound ^{17}O water with the surrounding solvent would result in losses in signal intensity.

3.6 Chapter-Specific Acknowledgements

There are many people I would like to thank that helped make this project possible. First, I would like to thank my predecessors who worked on this system, including Patrick van der Wel, Galia Debelouchina, and co-workers, for the wonderful work they did laying the groundwork for this study. Eric Keeler's work on ^{17}O and bound water was the inspiration for pursuing the ^{17}O experiments discussed in this chapter. I'd also like to thank Robert Silvers, who was instrumental in troubleshooting the procedure for recombinant expression and purification of GNNQQNY and working out the crystallization procedure.

I'd like to thank many people at the Koch Institute at MIT, including Richard Cook, Heather Amoroso, and Alex Austin, for their help troubleshooting the synthesis and HPLC purification of GNNQQNY. I would especially like to thank Alex Austin, whose procedure for synthesizing U-^{13}C,^{15}N GNNQQNY from a two-fold molar excess of starting material made this project financially feasible. This project would not have been possible without him. Finally, I'd like to thank my colleagues Natalie Golota and Edward Saliba for their assistance with acquiring and analyzing data presented in this chapter.

4 Design of Balanced Transmission Line Probe for ^{17}O DNP Experiments

4.1 Abstract

Oxygen and hydrogen are ubiquitous in biomolecules, yet they remain challenging to study via MAS NMR. The ability to directly probe hydrogen bonds via ^{1}H-^{17}O distance measurements could provide access to improved, previously unattainable biological structure data, and the ability to perform ^{1}H-detected DNP experiments on ^{17}O samples would be instrumental in achieving such measurements. This chapter outlines the design of a balanced transmission line DNP probe capable of studying ^{17}O biomolecules. The probe is designed to be equipped with a 1 mm MAS stator and is compatible with a helium recirculation system which should be able to achieve MAS frequencies >80 kHz at 100 K. An in-depth description of the probe design is provided.

4.2 Introduction & Motivation

Oxygen is one of the most common elements found in biomolecules yet remains somewhat challenging to observe via MAS NMR for several reasons. First, ^{17}O has a nuclear quadrupole moment which leads to substantial quadrupolar line broadening and poor spectral resolution. This broadening can be attenuated at high-magnetic fields which reduce the second-order nuclear quadrupole interaction.[101, 102] Additionally, ^{17}O has low natural abundance (0.037%) and a low gyromagnetic ratio ($0.14\gamma_H$) which results in low NMR sensitivity. Despite these limitations, the chemical shift range of ^{17}O is large (>1000 ppm overall, ~400 ppm for biomolecules) and there is a wealth of structural information that be obtained by studying the quadrupolar interaction.[103, 104]

Unlike ^{17}O, ^{1}H-detection results in very high NMR sensitivity. This can be attributed to the high gyromagnetic ratio of ^{1}H as well as its high natural abundance (99.99%). However, like ^{17}O,

^{1}H-detected spectra can result in broad linewidths and poor resolution. This a result of a limited chemical shift range and strong ^{1}H-^{1}H homonuclear dipolar couplings that are difficult to average out without fast MAS. The resolution of ^{1}H detected spectra can be improved by deuterating the sample; however, this can be expensive and will reduce the overall sensitivity of the experiment.[105, 106]

Fundamentally, some of the most interesting biological interactions take place between hydrogen and oxygen. For example, hydrogen bonding plays a critical role in the structure of biomolecules. This is especially true for water, which is perhaps the most critical molecule for sustaining life. Figure 4.1 is an example of how water and hydrogen bonding plays a role in the structure of proteins and other biomolecules. Having methodology to directly probe these interactions and obtain useful information from them would be invaluable for studying the structure and function of numerous biological systems, but advancements in instrumentation and equipment are needed to make this possible.

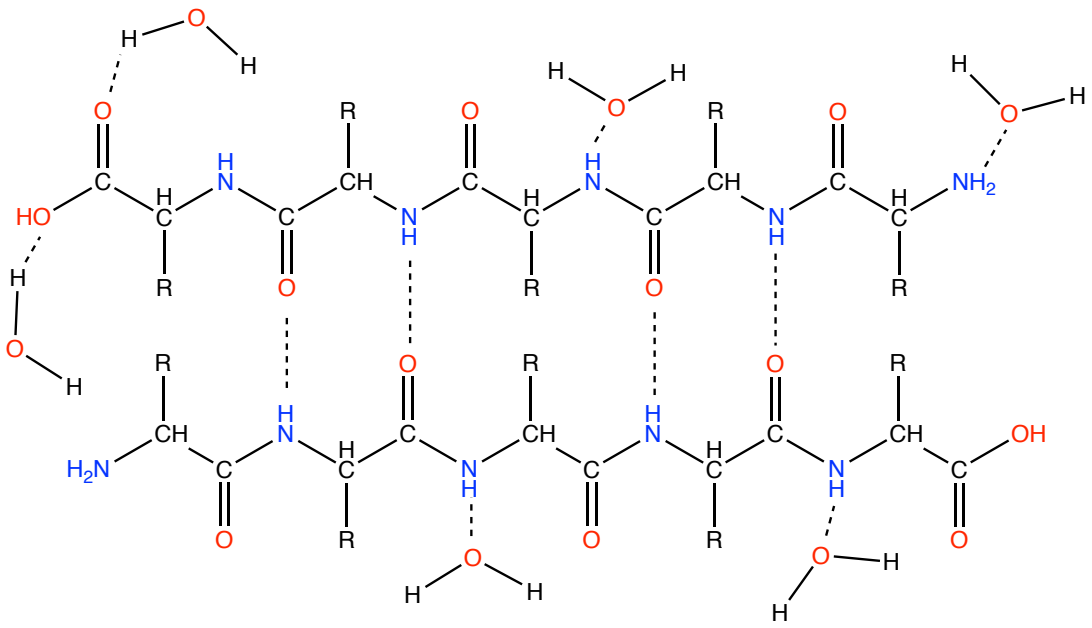

Figure 4.1: Schematic representation of hydrogen bonding in a protein system.

4.3 Overview of Balanced Transmissions Line Probe Designs

There are generally two types of RF circuits utilized in NMR probes: locally-tuned circuits and remotely-tuned circuits. In locally-tuned RF circuits, the tuning and matching components are located in close proximity to the RF coil. Probes with locally tuned circuits are advantageous due to their lightweight and compact circuits, but are less capable of handling high power loads than probes with remotely-tuned circuits. This is because the tuning and matching elements are located near the RF coil, in the bore of the magnet where space constraints are tighter than outside the bore. Smaller RF elements with lower power handling capabilities are typically used due to these space constraints. For DNP applications, having the tuning and matching elements located in close proximity to the coil has both advantages and disadvantages. The ability to cool the RF components reduces the thermal noise in the system and improves signal-to-noise, but when these electronics are cooled, their properties may change, making it more difficult to tune and isolate the probe.

In remotely-tuned circuits, the tuning and matching RF elements are located further away from the RF coil, typically outside the bore of the magnet. As a result, larger, more robust components may be used. This is particularly useful for solid-state NMR probes where the required RF power levels are substantially higher than in solution NMR probes. Transmission line circuits are an example of a remotely-tuned circuit. This section provides an overview of transmission line probe theory and introduces the concept of a balanced, stepped transmission line probe.

4.3.1 Transmission Line Theory

A transmission line in its simplest form is a pair of conductors separated by a dielectric material. Fundamentally, the function of a transmission line is to transmit a signal from one point to another with minimal reflection and loss in power. Transmission lines have a characteristic impedance (Z_0) which is defined by the ratio of the voltage and current of a wave propagating

through the line and is dependent on the geometry of the line. The most commonly encountered transmission line geometry in NMR probes is a coaxial line, which consists of two concentric conductors. The characteristic impedance of a coaxial transmission line is given by

$$Z_0 = \frac{138 \log(d/D)}{\sqrt{\varepsilon_r}} \quad \textbf{4.1}$$

where d is the outer diameter of the inner conductor, D is the inner diameter of the outer conductor, and ε_r is the dielectric constant of the insulation between the two conductors.

An important feature of transmission lines is their ability to act as impedance transformers. The input impedance for a lossless transmission line is given by

$$Z_{in} = Z_0 \frac{Z_L + jZ_0 \tan(\beta l)}{Z_0 + jZ_L \tan(\beta l)} \quad \textbf{4.2}$$

where Z_{in} is the input impedance of the transmission line, Z_L is the load impedance on the opposite end of the transmission line, Z_0 is the characteristic impedance of the line, l is the length of the transmission line, and β is the propagation constant, defined as $\beta=2\pi/\lambda$ where λ is the wavelength of the propagating wave. For a given load impedance, the input impedance of the transmission line can be adjusted simply by varying the length of the line. The impedance transformation properties of transmission lines are extremely useful for matching the impedance of a given load to the impedance of a given source. For a more detailed review of transmission line theory, the reader is referred to other literature.[107]

4.3.2 Balanced Transmission Line Probes

The DNP probe described in this chapter utilizes a balanced transmission line design that builds upon the work of previously published designs.[77, 108] The probe circuit consists of two sections: the "top probe" and "bottom probe". This balanced circuit design has many advantages with respect to improved probe performance and isolations. Fundamentally, by balancing the RF circuit in the probe, a common impedance node is generated at the center of the RF coil for all the

NMR frequencies in the circuit. The impedance node in the center of the coil maximizes the voltage difference across the coil and by extension also maximizes the current in the coil. The advantage of this is two-fold. First, balancing the RF coil leads to better homogeneity across the coil, which is especially important at high magnetic fields (≥500 MHz). Second, maximizing the voltage difference across the coil not only leads to more efficient power excitation, it also reduces the probability that arcing will occur to grounded components in the system.

In addition to the impedance node generated in the RF coil, a unique aspect of this probe design is its use of impedance nodes to achieve isolation between individual channels in the circuit. Typically, probe isolations are achieved via the implementation of lossy LC traps. It is advantageous to instead use transmissions lines for isolation purposes, as this will result in lower power losses in the system. At the impedance nodes in the bottom probe circuit, a common impedance minimum is generated at every NMR frequency in the circuit. This impedance node is located at the center of a transmission line junction in the bottom probe. Isolation of the channels is achieved by choosing a length of transmission line for each channel that can properly match the impedance node at the junction to the input impedance (typically 50 Ω) of the probe at one of the NMR frequencies, while at the same time generating a much higher impedance at the other frequencies in the circuit. In this sense, each channel has a very narrow range of frequencies capable of propagating along that specific path. A generic schematic of the probe circuit can be seen in Figure 4.2. The impedance nodes in the circuit are represented by black dots (•) in the diagram.

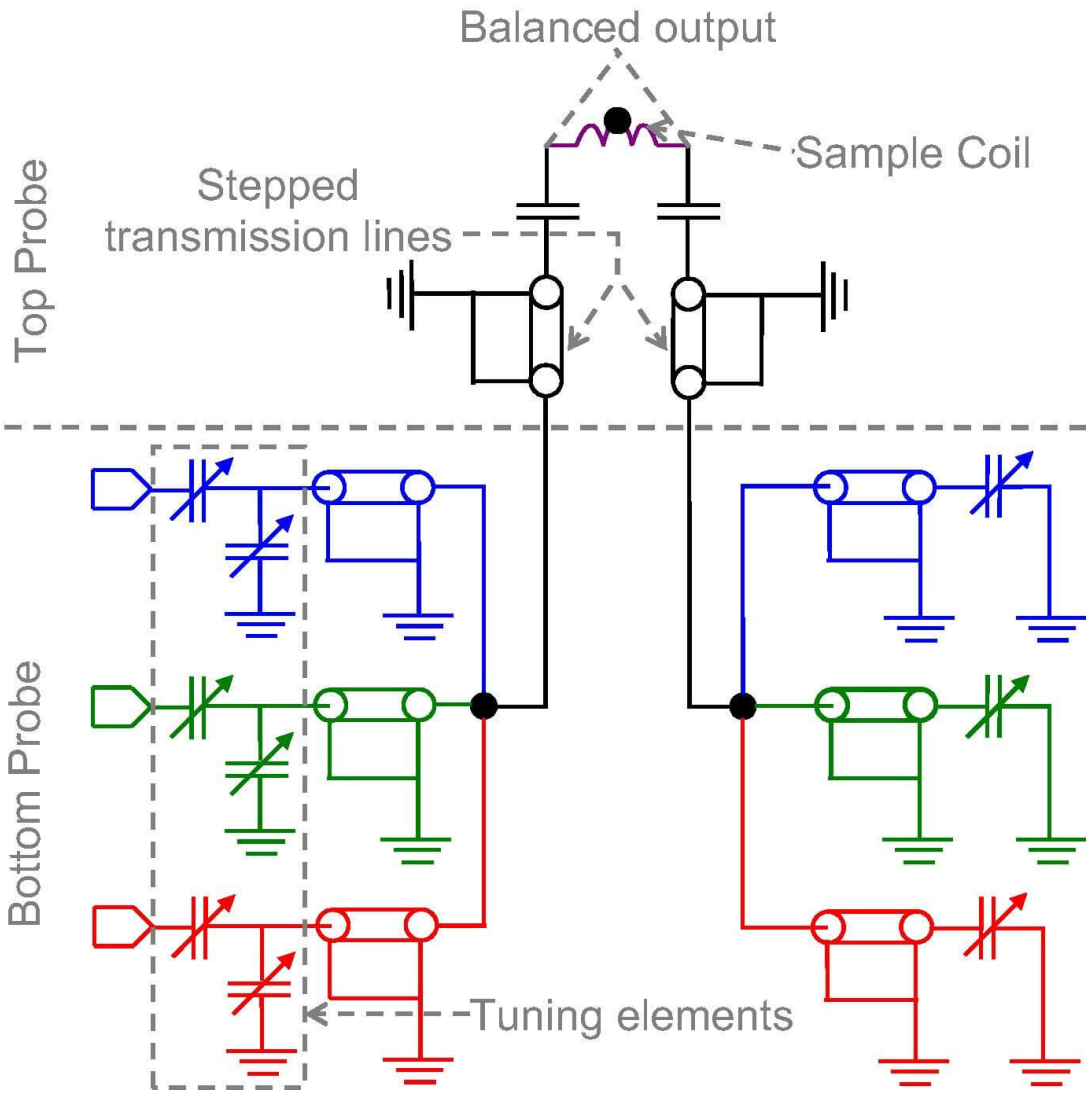

Figure 4.2: Circuit schematic of a balanced transmission line probe. Reprinted with permission.[77]

4.3.3 Impedance Matching with Stepped Transmission Line

Using a stepped transmission line, it is possible to perform impedance matching over a broad range of frequencies. The theory outlined in Section 4.3.1 can be extended to transmission lines without a uniform characteristic impedance over the entire length of the line. Figure 4.3 shows an example of a stepped transmission line in which the characteristic impedance changes as the wave propagates along the line. Equation 4.2 can be modified for a stepped transmission line such that the input impedance at any segment along the line is given by

$$Z_{i+1} = Z_{0,i}\frac{Z_i + jZ_{0,i}\tan(\beta l)}{Z_{0,i} + jZ_i\tan(\beta l)} \quad \textbf{4.3}$$

where i is an index representing a specific segment of the stepped transmission line. This is extremely useful in the balanced probe design, as for a given set of frequencies, there exists a stepped transmission line design that will transform impedances at the load to an impedance minimum at the node of the four-way tee. Rather than requiring three separate lines, all the NMR frequencies in the circuit can instead propagate along a single stepped transmission line.

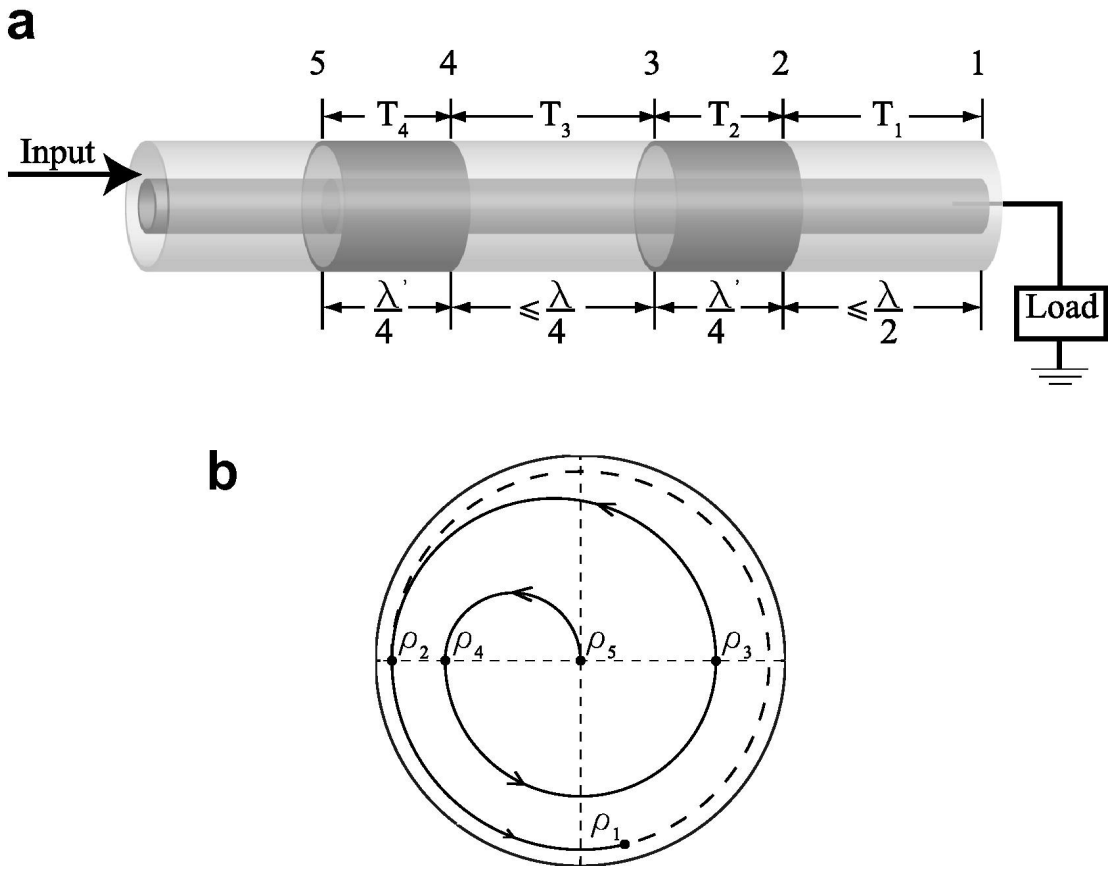

Figure 4.3: Example of stepped transmission line design. (a) Stepped transmission line in which the characteristic impedance varies along the length of the line. (b) Polar plot representing use of a stepped transmission line to impedance match a load. Reprinted with permission.[109]

4.4 DNP Probe Design

Using the concepts from balanced transmission line probe theory, a balanced transmission line DNP probe was designed to operate at a magnetic field of $\omega_{0H}/2\pi$ = 700 MHz. The probe is designed with a triple-resonance circuit and will be used to perform ^{1}H-detected ^{17}O experiments.

In this section, a detailed overview of the probe design is provided. All probe parts were manufactured via a combination of 3DHubs (Amsterdam, NL), MIT's Central Machine shop, and in-house fabrication.

4.4.1 Top Probe

4.4.1.1 Sample Chamber

The sample chamber houses the MAS stator among many other components. One of the challenging aspects of designing DNP probes is space constraints. The sample chamber must house many different components, all within a diameter of 2.35". This chamber must include space for two transmission lines, four gas lines, two capacitor arrays, two tubes for fiber optics and temperature sensors, the stator and its supports, a waveguide, magic angle adjust, and eject horn. Squeezing all of these components into such a small space requires a very carefully laid out design. Furthermore, because of the balanced probe design, the sample chamber ideally should be designed to be as symmetric as possible. Drawings of the sample chamber can be seen in Figure 4.4. All of the sample chamber components are housed in a low-temperature copper oven.

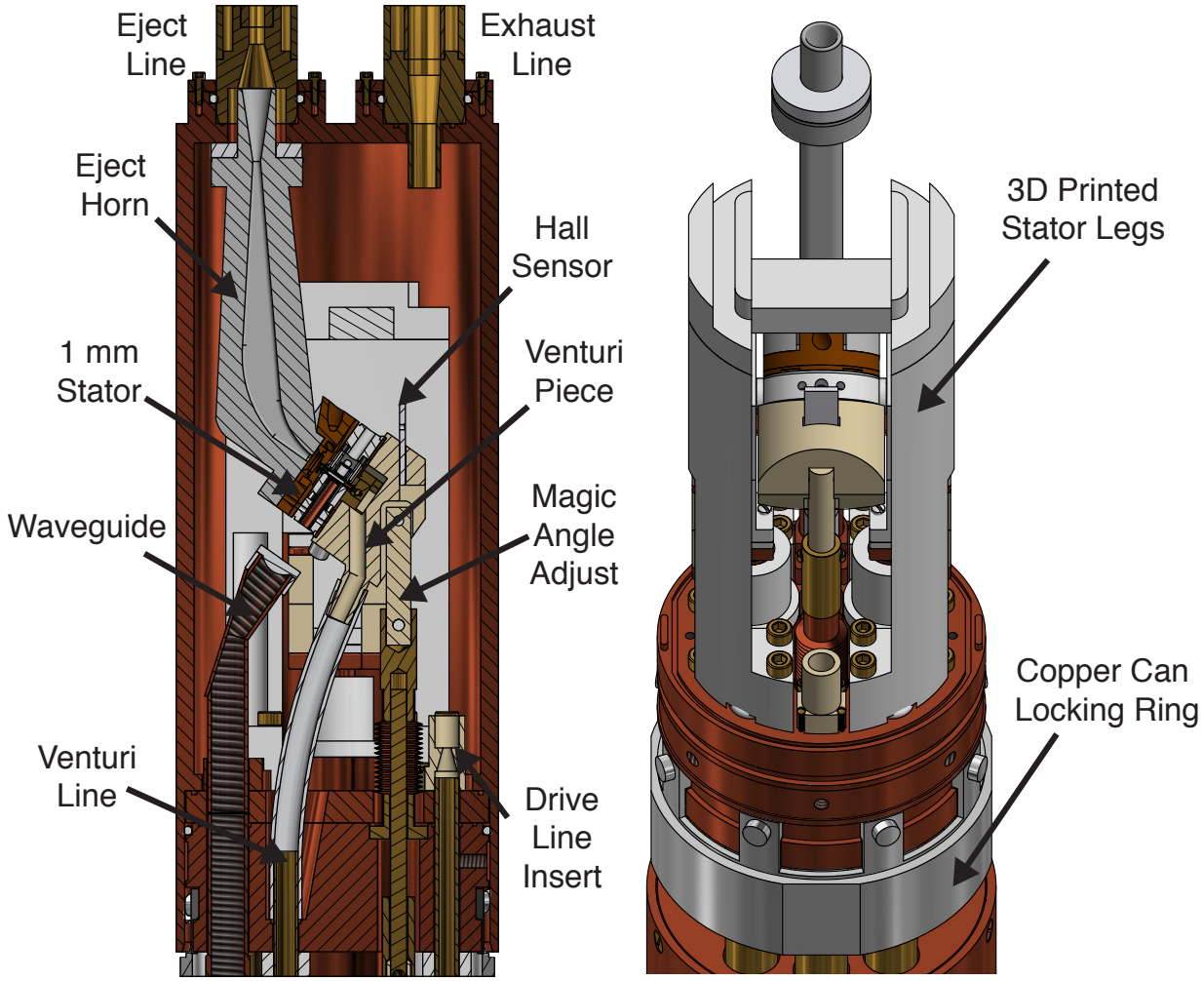

Figure 4.4: Diagram of cryogenic sample chamber.

The sample chamber contains a 1 mm stator, which is discussed in further detail in Section 4.6. On top of the stator assembly sits an eject horn, which is used to guide the rotor in and out of the stator during insertion and ejection of the sample. On the back of the stator is a Venturi piece designed to seal the back of the stator so a small vacuum can be pulled. To create a tight seal and allow for magic angle adjustment of the stator, the Venturi piece should be epoxied to the back of the stator. The eject horn, Venturi piece, and stator legs were all designed to be fabricated via 3D printing. This provided more flexibility when designing these components, particularly with the stator legs. The Venturi piece has space to include a cryogenic hall sensor, which can be used for accurate magic angle adjustments for sensitive quadrupole experiments such as STMAS.

The vertical waveguide is composed of copper with an inner diameter of 6.5 mm. At 460 GHz, the inner diameter of the waveguide is approximately ten times the wavelength of the microwave radiation. This should help minimize power losses in the waveguide assembly. To machine the waveguide corrugations, a custom tap was ordered that closely follows the recommended corrugation dimensions discussed in Section 1.2.4.2. The waveguide is capped with a TPX or PTFE lens that focuses the microwave beam from 6.5 mm down to < 2 mm so that it can propagate inside the waveguide of the coil block. To improve the machinability of the corrugated waveguide, the waveguide assembly was machined in short sections (≤ 3 in.) and soldered together.

The sample chamber is designed to allow different stator modules to be swapped in and out. Figure 4.5 depicts the stator module removed from the probe. Because of this modular design, a single probe can be used for many different kinds of experiments. For example, if more sample volume is required, the 1 mm stator module could be swapped out for a larger stator module such as a 3.2 mm module. The only additional change required during the stator swap is the insertion of a new stepped inner conductor, which would properly impedance match the balancing impedances of the stator module to an impedance node. In this sense, each stator module used on the probe will have its own unique stepped inner conductor.

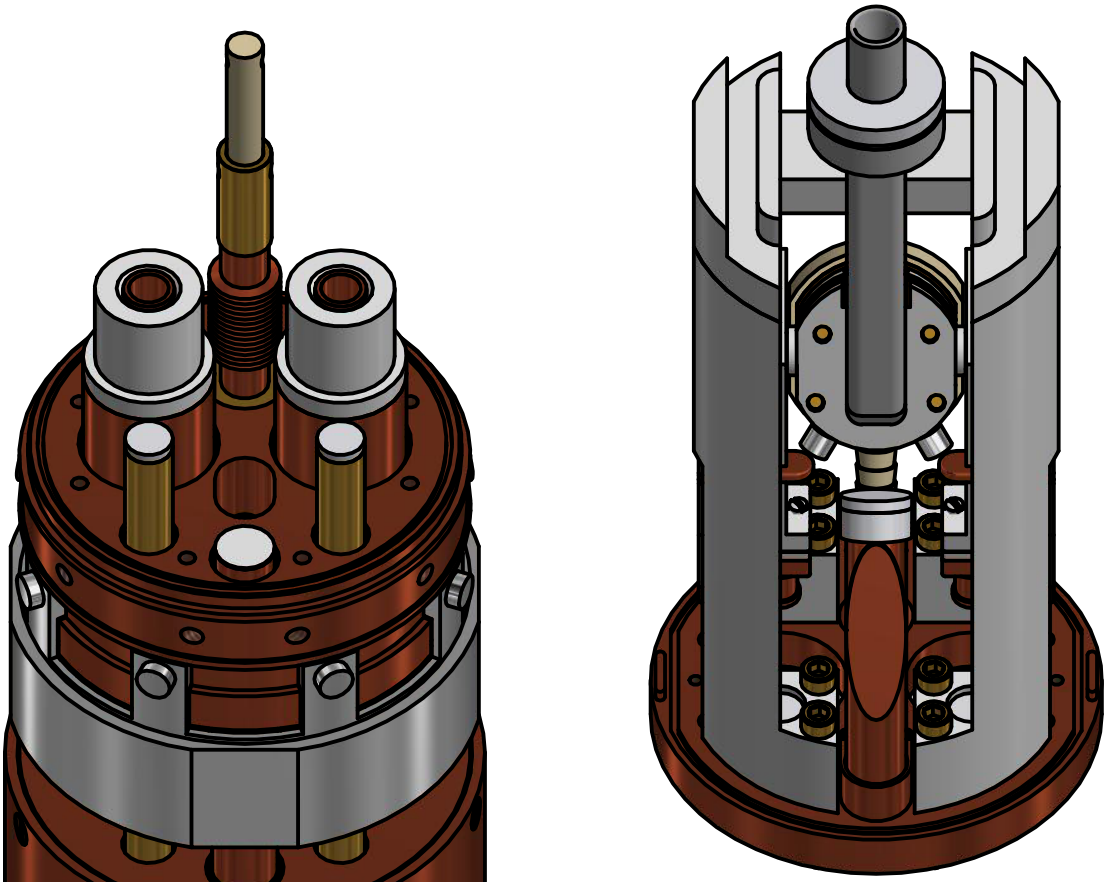

Figure 4.5: Diagram of a (right) stator module that has been removed from the (left) top probe.

4.4.1.2 Probe Box

The probe box contains the majority of the components for the Venturi pump system. The Venturi line is responsible for pulling a small vacuum (-200 to -400 mbar) on the back of the 1 mm stator in order to prevent rotor ejection. At helium DNP temperatures, the gas being pulled by the Venturi pump may be extremely cold (<50 K). To avoid ice buildup and destruction of sensitive probe components, several measures were taken. First, the Venturi vacuum line is vacuum-jacketed down the length of the probe until the gas reaches the probe box. From there, the Venturi line is connected to a ~9 in. copper heating tube via stainless steel VCR fittings. The copper heating tube is wrapped in electrical heating tape followed by a layer or layers of high temperature insulation to prevent the probe box from overheating. After passing through the heating tube, the

gas proceeds through a three-way VCR ball valve before entering a Piab (Täby, SE) M10L Venturi pump. The three-way valve was implemented as a convenient way to eject the rotor. When the Venturi pump is not in use, the valve may be turned 90° to allow gas to be pushed through the Venturi line and onto the bottom of the rotor to eject the sample from the probe.

The Venturi pump itself is housed within a cryostat. The cryostat consists of an inner and outer box with a layer of vacuum in between. The purpose of the cryostat is to insulate the Venturi pump and its components from the rest of the probe and to provide a way of recapturing the exhausted Venturi helium while avoiding leaks. A vacuum feedthrough tube in the cryostat allows electrical components such as temperature sensors and heating elements to be placed in the inner cryostat box. The inner cryostat box may contain a heating element to keep the Venturi pump warm in the event that the copper heating tube does not sufficiently warm the gas. This is to avoid damage to the plastic pump and rubber O-ring at low (< -20°C) temperatures. The inner and outer cryostat boxes are designed to be sealed with cryogenic epoxy, which can be removed in the event of required maintenance.

In addition to the Venturi components, the probe box also holds the tapered waveguide. The tapered waveguide reduces the diameter of the Gaussian microwave beam from the 19 mm diameter gyrotron waveguide down to 6.5 mm so that the microwaves can be delivered up the bore of the magnet and to the sample. The length of the taper was determined by Equation 1.27. The corrugations in the tapered waveguide were made individually using a grooving tool. Due to limitations in the length of available grooving tools, the tapered waveguide was machined in four sections. To improve the machinability of the corrugations in the tapered waveguide, the waveguide was constructed from brass.

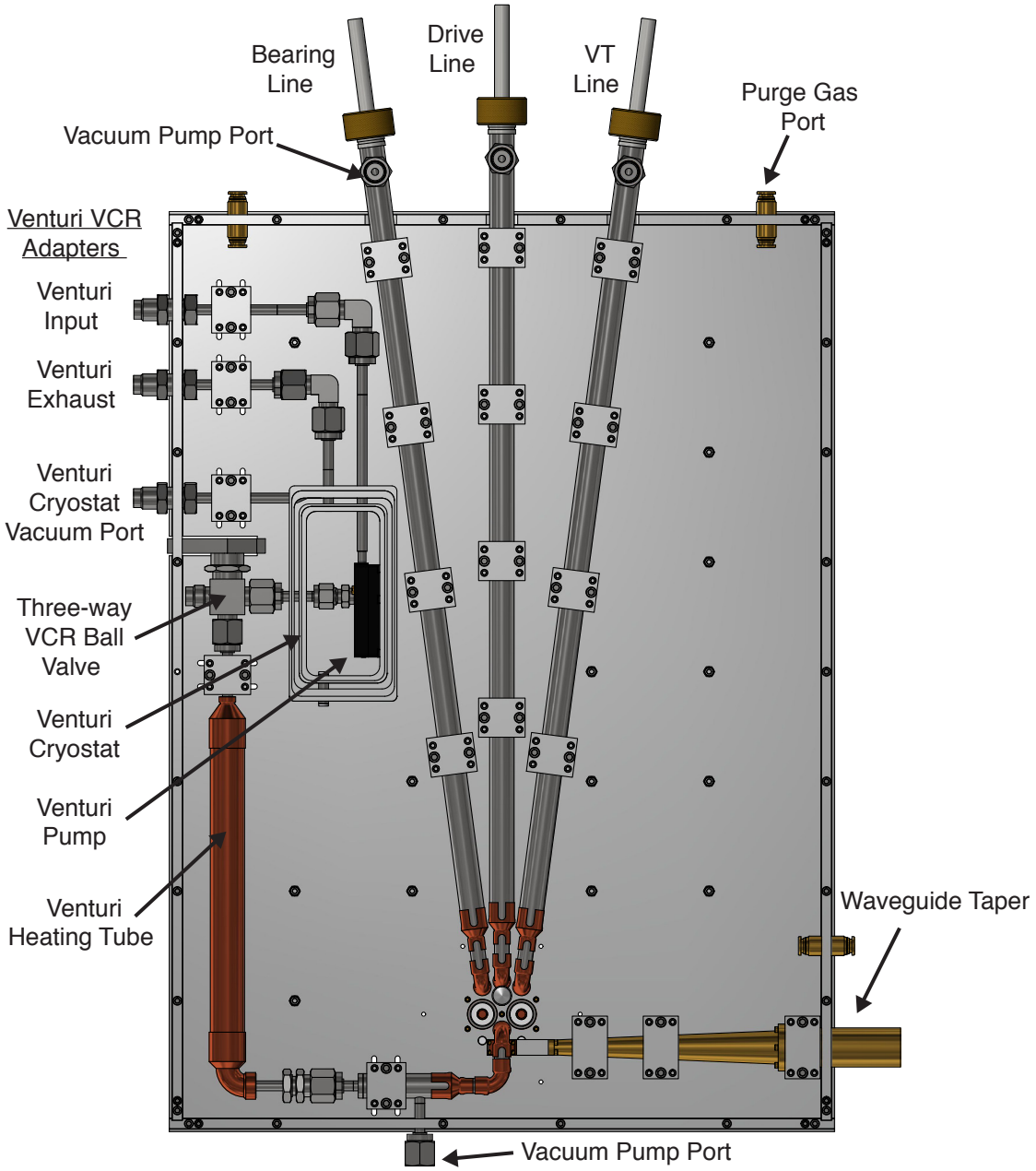

Figure 4.6: Diagram of probe box containing gas delivery lines, the venture cryostat, and the tapered waveguide.

4.4.2 Bottom Probe

The bottom probe contains the probe's tuning, matching, and balancing elements. The tuning/matching and balancing capacitors are all contained in individual shielding boxes (one per tune/match and balancing channel) to prevent external RF interference. At the center of the bottom

probe is the four-way tee that serves as the junction point for each channel in the probe. The tee contains four branches: one leading to the sample chamber and three other branches for each of the frequencies in the triple-resonance circuit. The bottom probe was designed with flexibility in mind, evidenced by the grid of threaded holes. This grid allows for smaller movements of the RF shielding boxes, and by extension, finer adjustments of the transmission line lengths, thereby facilitating optimization of the tuning and isolations along each branch. A CAD drawing of the bottom probe can be seen in Figure 4.7.

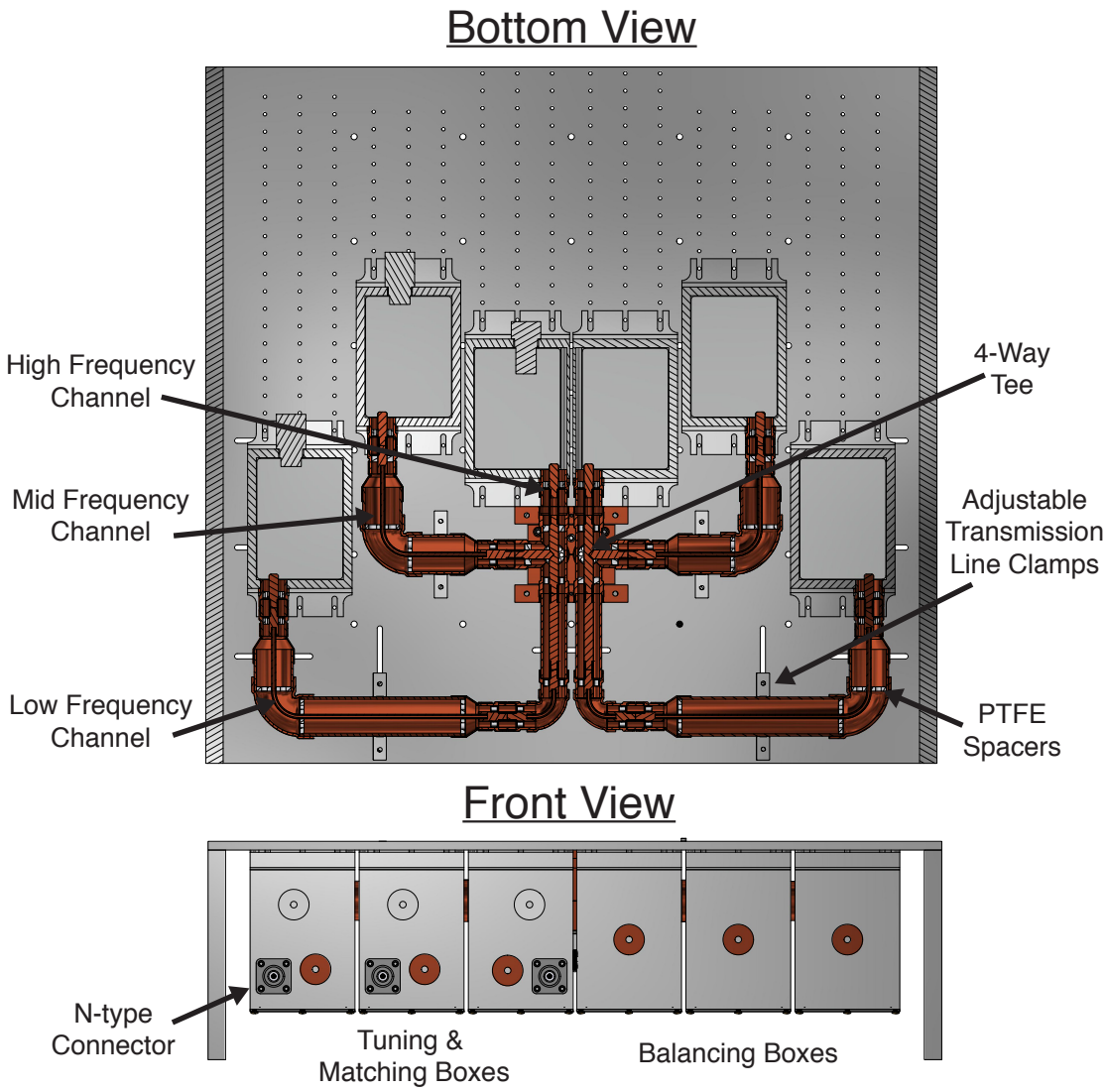

Figure 4.7: Diagram of bottom probe design.

4.4.3 Probe Cryostat

The purpose of the probe's cryostat is to insulate the low temperature sample chamber from the bore of the magnet. This piece of equipment is vital, as cryogenic cooling of the magnet bore may result in the magnet's O-rings cracking, which could lead to a quench of the high-field magnet. The cryostat consists primarily of two bronze jackets with a vacuum layer in between. Bronze is an ideal choice for DNP cryostats, as it is non-magnetic and has low thermal conductivity. The bronze jackets are each 0.030" thick and have a vacuum layer of 0.046" between the inner and outer jacket. A stainless steel VCR vacuum port is included at the bottom of the cryostat so that the cryostat may be continuously pumped on while inside the magnet. To allow for insertion of the eject and exhaust line through the top of the cryostat, a G-10CR thermal break was used in combination with a Mini-Flex (Ventura, USA) BeCu bellow. The thermal break reduces heat transfer between the cold inner jacket and warm outer jacket, while the bellow helps reduce strain on the cryostat due to thermal contraction. A set of threads was included on the top of the cryostat to attach the eject and exhaust line to the cryostat. These threads are referred to as compression threads, as they help form a helium-tight indium seal at the top of the probe's sample chamber (Section 4.4.5).

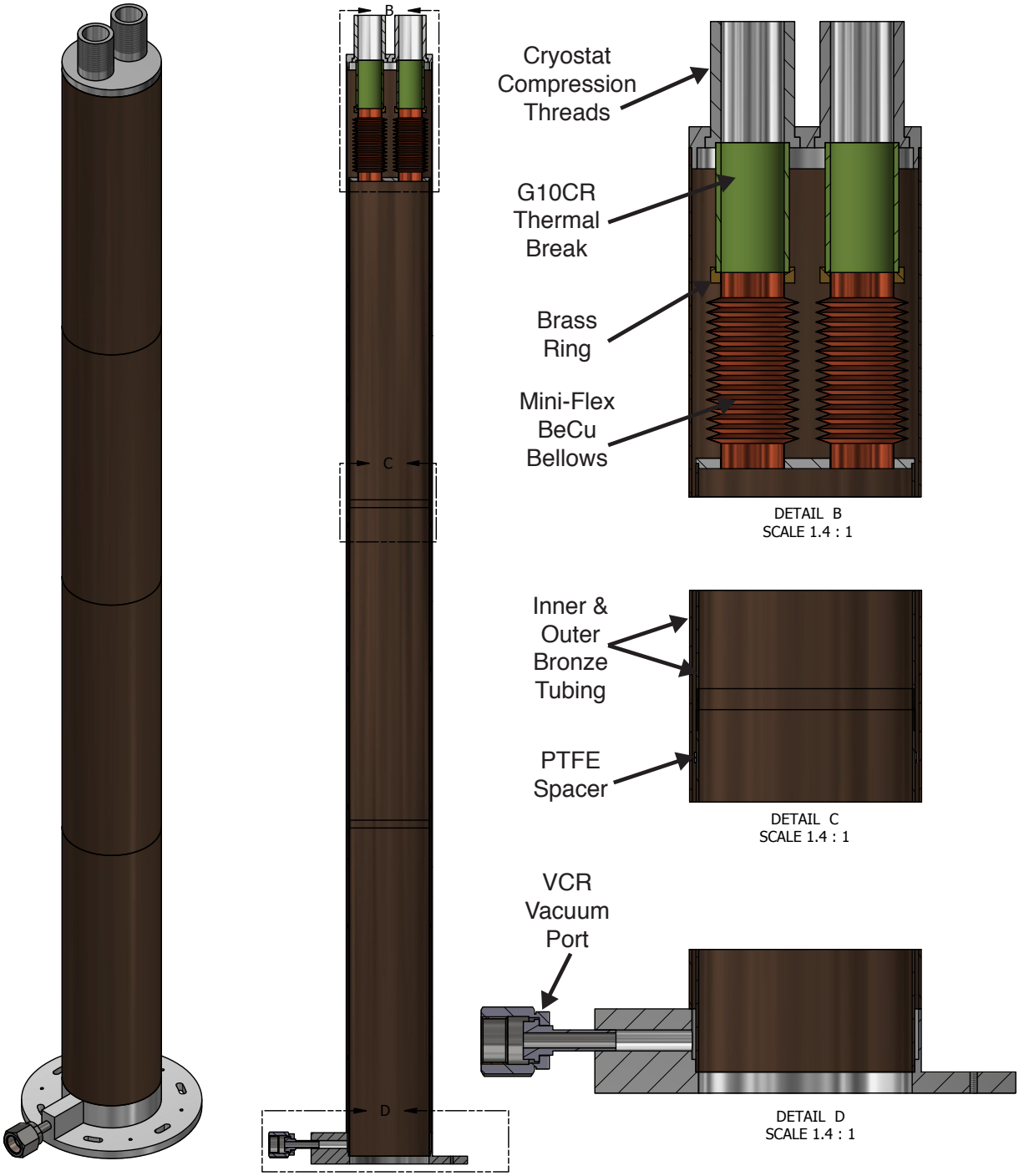

Figure 4.8: Diagram of the probe cryostat. (Left) Depiction of the full cryostat. (Middle) Cross-sectional view of the cryostat. (Right) Detailed views of various areas of the cryostat, including the thermal break and pump out port.

4.4.4 Eject & Exhaust Lines

The eject and exhaust lines are vacuum-jacketed lines that mate with the probe's cryostat. The lower halves of the lines are made from brass, while the tops of the lines are made from stainless steel due to its lower thermal conductivity. The mating surface at the bottom of the lines is highly polished (≤8 μin) so that it is compatible with helium sealing methods (Section 4.4.5). Each line contains a stainless steel bellow on the inner line to help reduce strain from thermal contraction during cooling. The exhaust line has a male bayonet at the top of the line that mates with a custom-built cryogenic shut off valve from Precision Cryogenics (Indianapolis, US). The eject line has a sample catcher at the top designed to insert and eject rotors under a helium atmosphere. For more details on the compatibility of the eject and exhaust lines with the helium recirculation system, please see Chapter 5.

4.4.5 Helium-tight Sealing Methods

In any application involving helium, proper sealing of the system can be challenging. As the smallest atom, helium is prone to high leak rates even through well-designed seals. Helium sealing for DNP probes is especially challenging, as the seals must remain helium-tight at cryogenic temperatures and ideally must be demountable in order to perform maintenance on the probe. Fortunately, there are a few potential solutions to create hermetic ("gas-tight"), demountable seals at cryogenic temperatures.[110]

In the current DNP probe design, there are two regions which are particularly susceptible to helium leakage: the gas lines to the probe and the sample chamber. The former can be sealed with proper cryogenic equipment rated for helium applications. The Venturi gas line is sealed using a series of VCR fittings and adapters as well as cryogenic epoxy. In this probe design, the input gas lines for drive, bearing, and VT gas delivery include a vacuum-jacketed bayonet sealing

system developed by Precision Cryogenics. The sealing of helium using the bayonets is two-fold. First, the male and female bayonets form a metal-to-metal gas-tight seal that minimizes the leakage of helium even at cryogenic temperatures. Second, an O-ring is used to help align the bayonets as well as form a secondary seal to prevent leakage of any helium that may escape the metal-to-metal seal. The lines can be taken on and off via a sealing nut located on the male bayonet. A diagram of the bayonet seals can be seen in Figure 4.9.

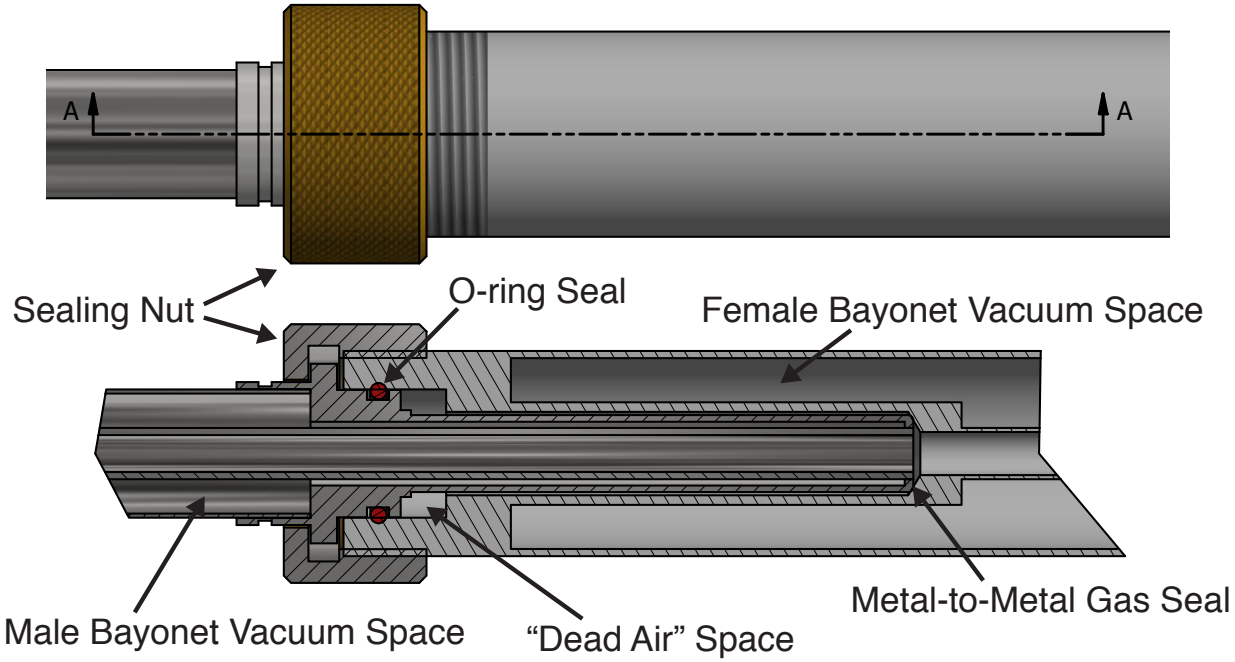

Figure 4.9: Diagram of Precision Cryogenics bayonet assembly. This assembly is used to prevent helium leaks at the gas input of the probe.

Preventing helium leaks in the sample chamber is more complex. For parts of the sample chamber in which sealing can be semi-permanent, cryogenic epoxies with low helium diffusivity may be used.[111] While more permanent than other options, epoxies generally can be removed with an extended soak in an organic solvent such as acetone. For preventing leaks from sample chamber components such as the gas line holes in the sample chamber base, applying a small amount of cryogenic epoxy around these lines should be sufficient for long-term cryogenic sealing.

There are a few methods for creating demountable, helium-tight seals at cryogenic temperatures, all of which are accompanied by their own respective challenges. The first, and perhaps most common, sealing method involves using indium metal.[112, 113] Indium has a low melting point and is highly malleable even at cryogenic temperatures. Generally, indium gaskets function by crushing clean, high purity (≥99.995%) indium between two pieces of metal. The indium is capable of filling in gaps in the metal surfaces and can form bonds with the metal to make a helium-tight seal. While indium seals can be formed on "as machined" surfaces, higher surface finishes (≤32 μin.) generally are preferred for creating optimal seals. Additionally, the metal surfaces should be kept clean and free of dirt.

For an indium O-ring, the groove for the indium wire should be sized such that the indium overfills the groove by ~10-20%. To properly crush the indium metal and ensure a good seal, the sealing flange should be designed in such a way that an even amount of pressure is distributed symmetrically around the O-ring groove. Consequently, the tight seals formed by indium metal make it difficult to remove the flange when necessary. For this reason, it is advisable to include a means to provide counterpressure to the flange to break the indium seal when needed. This can typically be achieved by leaving a few extra threaded holes through which a bolt can apply counterpressure to the flange and break the indium seal.

Another common method for helium-sealing involves the use of PTFE or FEP O-rings. FEP has significant advantages over elastomeric O-rings at cryogenic temperatures. As elastomeric O-rings cool down, they begin to harden and lose their sealing properties, but FEP remains flexible down to temperatures close to that of liquid helium. The disadvantages of FEP O-rings include their hardness, which makes it difficult to achieve quality seals, and their limited resistance to creep compared to elastomeric O-rings. The latter disadvantage can be reduced by

using spring-energized O-rings that improve creep resistance and reusability, while the former can be combated with very high surface finishes, typically < 8 μin. to achieve helium-tight seals for static applications.

An example of the demountable cryogenic seals used in the sample chamber can be seen in Figure 4.10. Each potential area where helium leakage may occur is sealed by both an indium seal as well as a spring-reinforced FEP O-ring. While either of these sealing methods on their own should be enough to prevent helium leakage in the sample chamber, both were included as an extra precaution. For all surfaces in contact with the FEP O-rings, a minimum surface finish of 8 μin. was specified during manufacturing. For surface finishes where indium O-ring were to be used, a minimum surface finish of 16 μin. was specified. Although not pictured in Figure 4.10, the sample chamber was designed in such a way that the indium seals could be properly formed and removed. The indium seal between the insert/eject line and exhaust line with the copper oven can be formed and broken with a compression and decompression nut on each of the lines that screws into the top of the probe's cryostat. The formation of the indium seal between the copper can and the top compression plate can be formed and broken by turning the locking ring clockwise and counterclockwise. The seal between the top compression plate and the sample chamber base can be formed and broken via a series of 4-40 and 2-56 bolts spaced around the sample chamber.

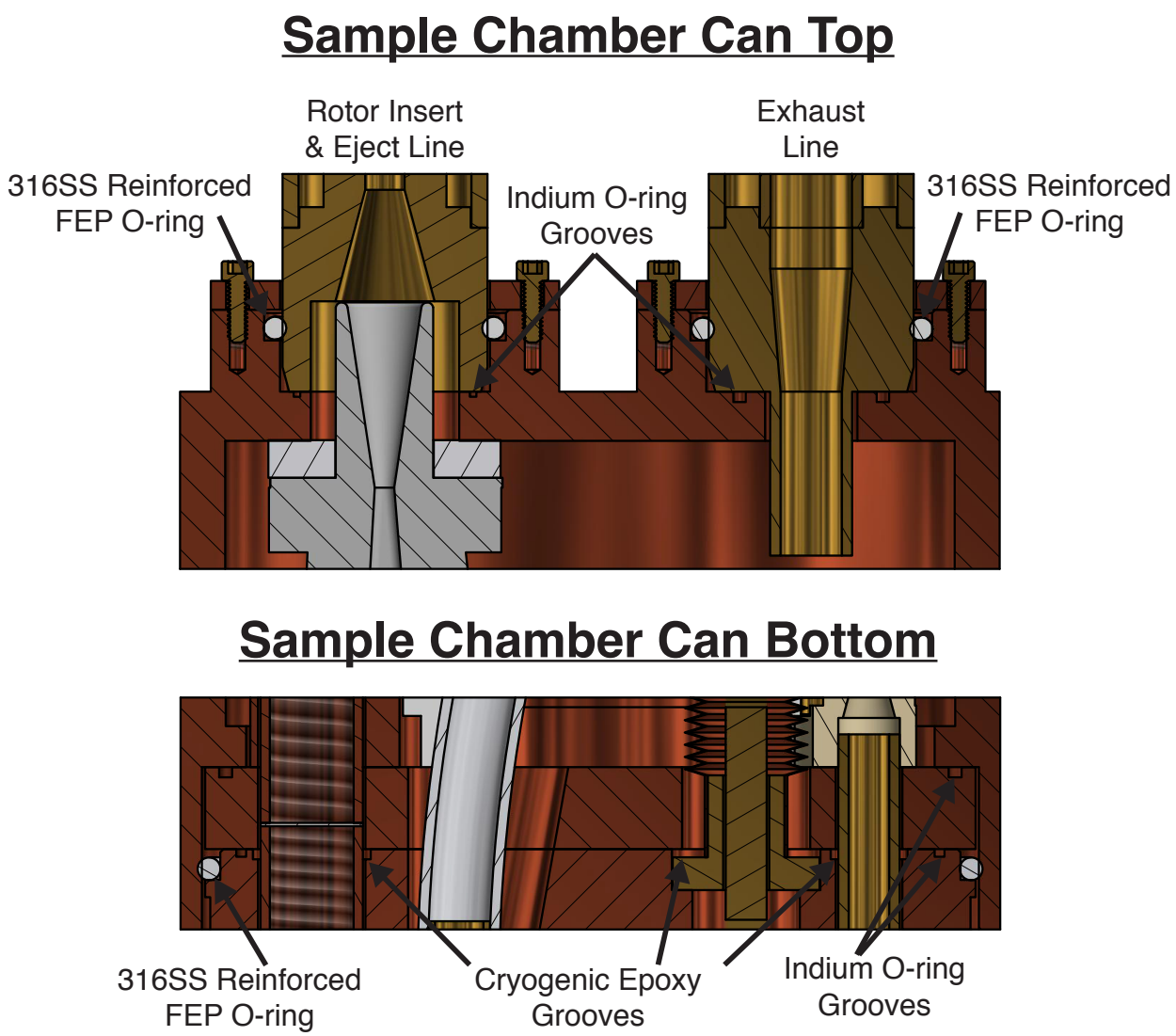

Figure 4.10: Diagram of cryogenic seal design in sample chamber. Each potential point for helium leakage is sealed with both an indium seal as well as a spring-reinforced FEP O-ring.

4.5 Stepped Transmission Line Design

At the heart of this balanced transmission line probe design is the stepped transmission line. The stepped transmission line is a critical feature, because it transforms the sample chamber impedances into an impedance node for every NMR frequency in the probe circuit. This is not a trivial task, particularly for NMR frequencies that are not well separated. The process of designing the stepped transmission line involves obtaining initial measurements on the sample scattering

parameters (S-parameters) followed by simulations of appropriate stepped transmission line designs.

4.5.1 Type-N Adapter Design

The type-N adapters are an indispensable tool for measuring the scattering parameters of the sample chamber. The adapters must be designed in such a way that their measurement of the S-parameters has a minimal effect on the S-parameters themselves. To do this, the type-N adapters should ideally behave as if they were 50 Ω coaxial cables. The adapters themselves feature a type-N RF connector attached to a 50 Ω characteristic impedance transmission line. CAD drawings of a type-N adapter pair can be seen in Figure 4.11.

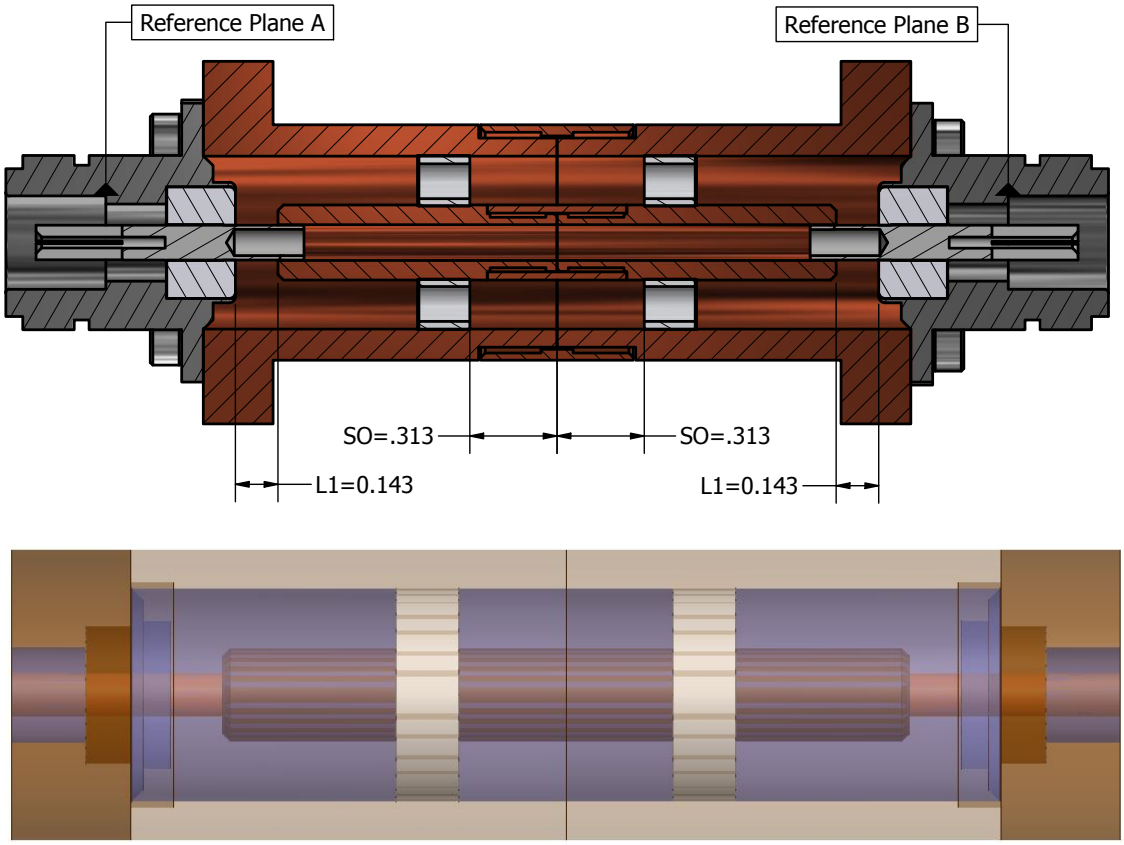

Figure 4.11: Drawings of type-N adapter pair. (Top) type-N adapter pair as drawn in Autodesk Inventor. (Bottom) type-N adapter pair as modeled in HFSS.

ANSYS (Canonsburg, PA) HFSS simulations were run to ensure that the type-N adapters behaved like ideal 50 Ω coaxial cables over the entire range of frequencies in the circuit. The model for the simulations consisted of a pair of type-N adapters connected at their transmission line ends. The HFSS simulations modeled the adapter pair up to the reference planes for the type-N connectors. Ideally, the reflections measured in the adapter pair should be minimized over all frequencies in the circuit. This can be modeled by assigning excitation ports at each end of the adapter pair and simulating the resulting S-parameters of the pair over the range of relevant frequencies. Geometrical optimization of the adapter pair can be performed in HFSS by sweeping parametrized dimensions in the adapter pair. In this case, the PTFE spacer offset (SO) and distance (L1) between the inner conductors and type-N connector were swept in order to minimize reflections. The results indicate that for all relevant frequencies in the circuit, the reflection of the type-N adapters should be -50 dB or better. A simulated frequency plot of the RF reflection for the type-N adapters can be seen in Figure 4.12.

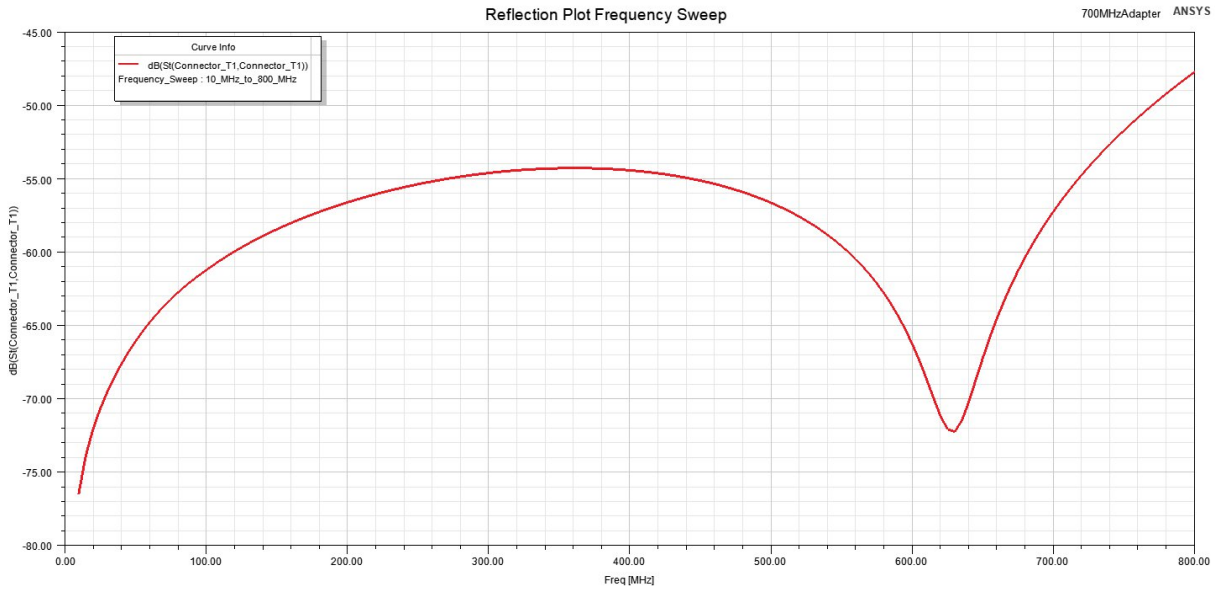

Figure 4.12: Frequency plot modeling the RF reflection in the type-N adapters.

4.5.2 Measuring Sample Chamber Impedances & De-embedding

The sample chamber contains stray capacitances and inductances that make it difficult to model the S-parameters of the chamber. Instead, the type-N adapters can be used to measure the S-parameters directly. The electrical delay of the type-N adapters can be measured on a vector network analyzer (VNA) using the adapter pair model seen in Figure 4.11. Since the type-N adapters should behave as 50 Ω coaxial lines, the effects of the adapters on the measured scattering parameters can be removed with a simple port extension.

When measuring the S-parameters of the sample chamber, de-embedding is a necessary step to remove the effects of the measuring devices on that of the device under test (DUT). In this case the DUT is the sample chamber of the probe and the measuring devices consist of uniform 50 Ω transmission lines on the tuning/matching and balancing sides of the sample chamber as well as the type-N adapters. The general procedure for de-embedding S-parameter measurements of the sample chamber can be seen in Figure 4.13 and proceeds as follows. First, the S-parameters of the uniform 50 Ω transmission lines are measured using the type-N adapters. This step is completed

for both the tuning/matching and balancing transmission lines. Next, the 50 Ω transmission lines are connected to the sample chamber, and the S-parameters of the transmission line and sample chamber assembly are measured. During all measurements, the effects of the type-N adapters are removed using port extensions. Additionally, it should be noted that the transmission lines themselves extend into the sample chamber and must be partially included in the S-parameter measurement of the sample chamber. To accomplish this, the reference plane of the sample chamber should include a small length (~0.5") of the transmission line. This effect on the S-parameters of the transmission lines can be removed by applying an appropriate port extension to the transmission lines during measurement. The measured S-parameters can then be converted to T-parameters via the following transformation

$$\begin{bmatrix} T_{11} & T_{12} \\ T_{21} & T_{22} \end{bmatrix} = \begin{bmatrix} -\frac{S_{11}S_{22} - S_{12}S_{21}}{S_{21}} & \frac{S_{11}}{S_{21}} \\ -\frac{S_{22}}{S_{21}} & \frac{1}{S_{21}} \end{bmatrix} \quad \textbf{4.4}$$

Once the T-parameters have been calculated for the sample chamber and transmission line assembly, the T-parameters for the DUT can be calculated using the transformation

$$T_{DUT} = T_A^{-1} T_m T_B^{-1} \quad \textbf{4.5}$$

where T_{DUT} are the T-parameters for the DUT, T_m are the measured T-parameters for the entire sample chamber assembly including transmission lines, and T_A and T_B are the T-parameters for each of the 50 Ω transmission lines. The S-parameters of the sample chamber can then be calculated using the transformation

$$\begin{bmatrix} S_{11} & S_{12} \\ S_{21} & S_{22} \end{bmatrix} = \begin{bmatrix} \frac{T_{12}}{T_{22}} & \frac{T_{11}T_{22} - T_{12}T_{21}}{T_{22}} \\ \frac{1}{T_{22}} & -\frac{T_{21}}{T_{22}} \end{bmatrix} \quad \textbf{4.6}$$

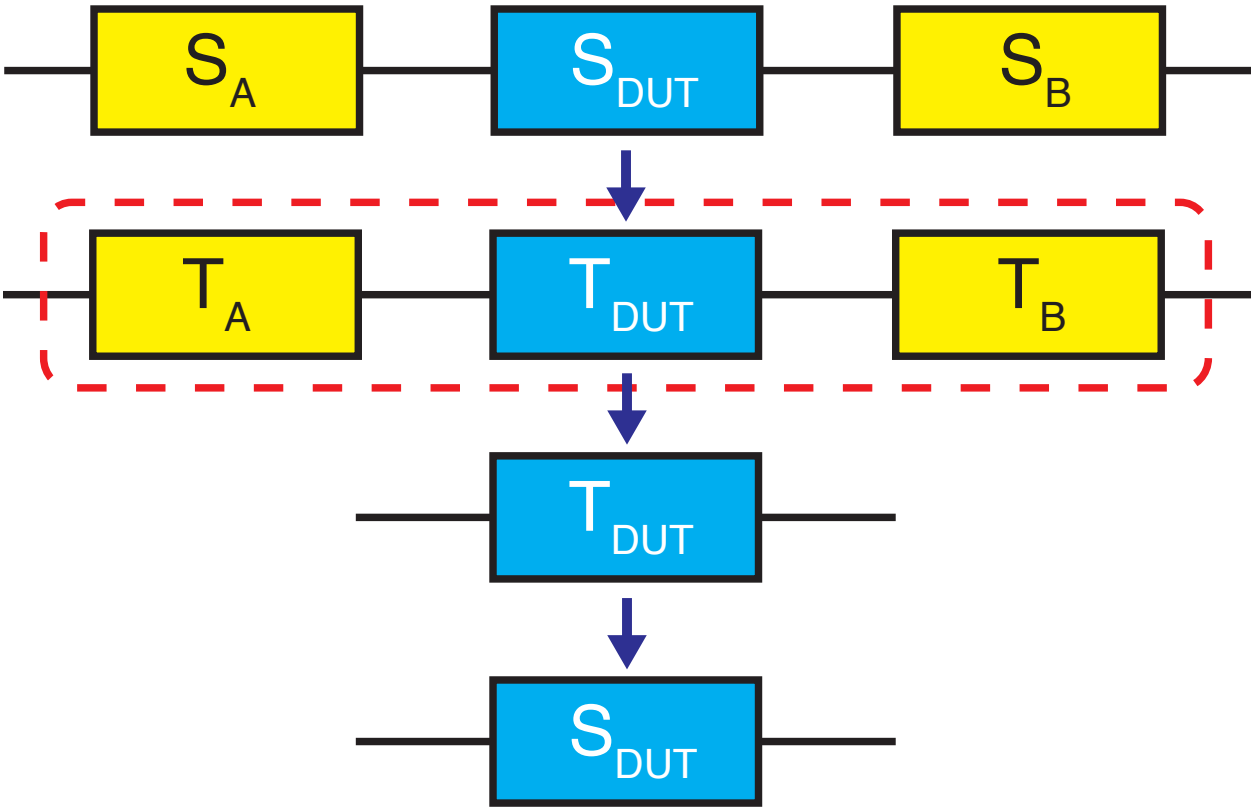

Figure 4.13: Schematic representation of de-embedding procedure.

Once the sample chamber S-parameters are known, the input and output impedances of the sample chamber can be determined using circuit simulation software. Input and output impedances must be complex conjugates of each other to achieve an impedance node at the center of the coil. There are two such conditions that can be used to achieve this: one that produces a current maximum in the center of the coil and one that produces a voltage maximum. For our purposes, the simulation software should be used to find the condition that produces the former.

4.5.3 Simulations of Stepped Transmission Line

Once the sample chamber balancing impedances are known, a stepped transmission line must be designed that will transform the impedance at the sample chamber to a common impedance node at the junction of the four-way tee. This can be accomplished by simulating the stepped transmission line and changing the transmission line parameters manually, but this is a

very time-consuming process. Instead, a MATLAB script was written to calculate multiple stepped transmission line designs that could achieve this impedance transformation. The MATLAB code utilizes the theory described in Section 4.3.3 to design a random set of stepped transmission lines that meet specified constraints. The MATLAB code for these calculations can be found in Section 4.9.

Accurate impedances are necessary for the MATLAB script to function. To test the MATLAB code, impedance measurements from previous literature were used.[77] The MATLAB script outputs a table of values for the length of each transmission line segment, the characteristic impedance of each segment, and the overall input impedance at each frequency. The stepped transmission lines determined by the MATLAB code were simulated in AWR to check for accuracy. Figure 4.14 shows a circuit simulation performed in AWR for a given stepped transmission line design. From the simulation, it is clear that the sample chamber impedance is transformed to a short at the input of the stepped transmission line. The final step before fabrication of a stepped transmission line is an HFSS analysis of the line to determine whether there are any problematic areas where high voltage may build up and arcing may occur.

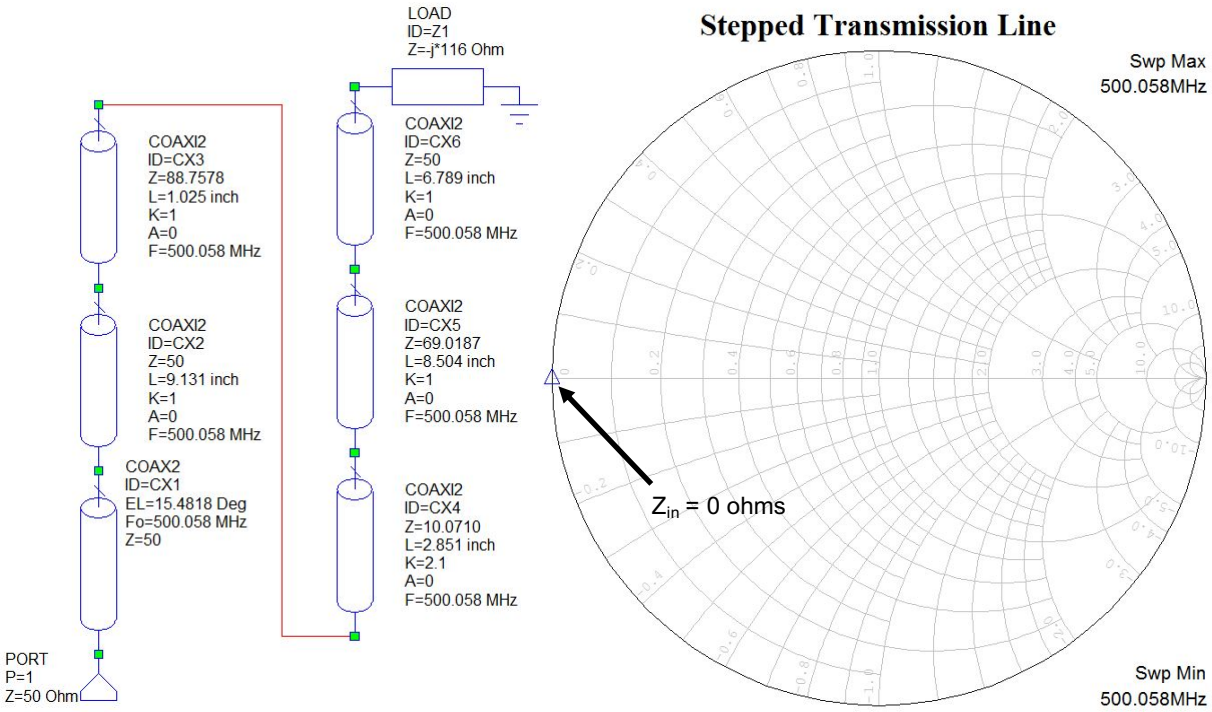

Figure 4.14: AWR circuit simulation of stepped transmission line.

4.6 1 mm MAS Stator

To perform ^{1}H-detected DNP experiments, the DNP probe must be equipped with a stator that can achieve the fast MAS frequencies necessary for high resolution ^{1}H-detection. Currently, both 1.3 mm and 0.7 mm DNP probes are commercially available. At 100 K, with nitrogen as the spinning medium, these probes can achieve MAS frequencies of 40 kHz and 65 kHz respectively.[56, 57] At these spinning frequencies, it is difficult to perform ^{1}H-detected experiments without requiring high levels of deuteration. Ideally, for ^{1}H-detected experiments on biological samples, the MAS frequency should be as high as possible. However, even MAS frequencies as low as 80 kHz can substantially affect the quality of multi-dimensional ^{1}H-detected NMR spectra. An example of this can be seen in Figure 4.15.[114]

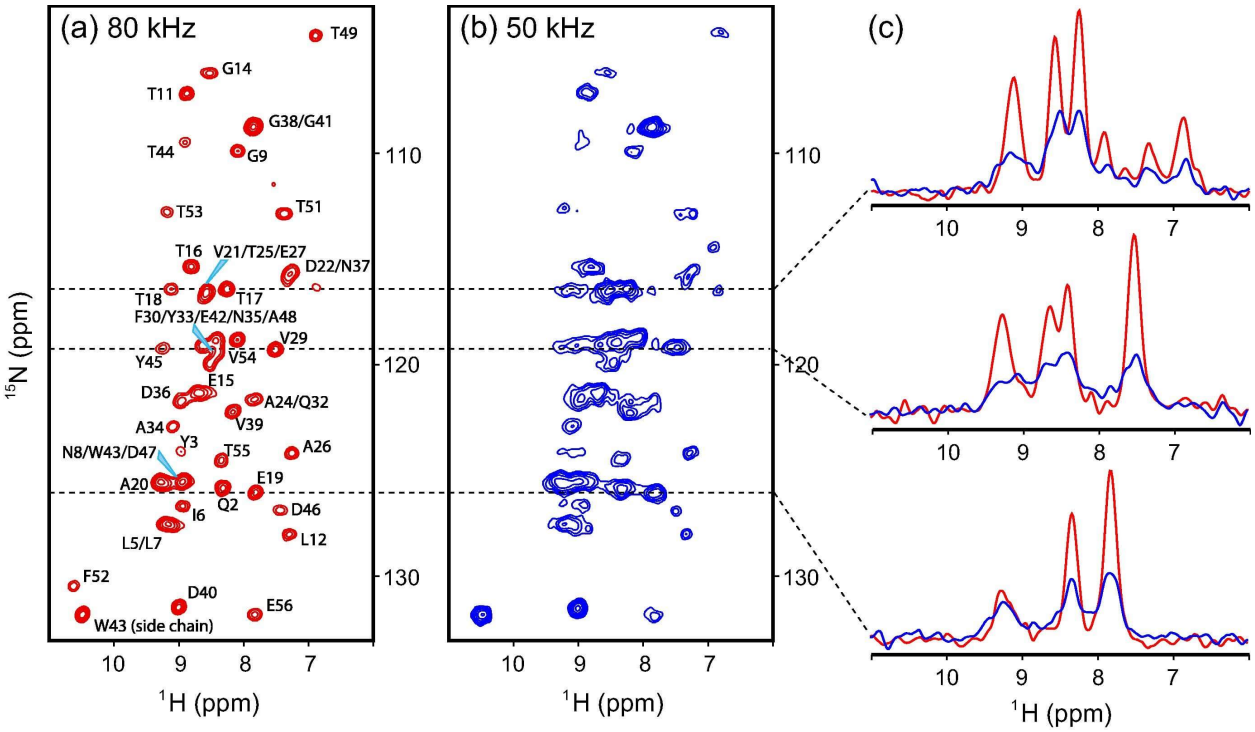

Figure 4.15: 2D NMR resolution comparison of ^{1}H-detected spectra recorded at 80 kHz and 50 kHz MAS. Reprinted with permission.[114]

Using helium as the spinning medium, MAS rotors should be able to achieve MAS frequencies at 100 K that, at a minimum, are comparable to room temperature spinning frequencies when nitrogen gas is the driving fluid. For 1.3 mm and 0.7 mm rotors, this would translate to MAS frequencies of approximately 67 kHz and 110 kHz at 100 K, respectively. Presently, there are no systems in the literature that utilize helium gas to spin rotors smaller than 3.2 mm. Spinning frequencies as high as 25 kHz have been achieved for 3.2 mm rotors at 90 K, however this is well below the threshold for ^{1}H-detection experiments.[115] Given these limitations, the decision was made to develop a 1 mm stator system that would be capable of performing ^{1}H-detection experiments at cryogenic temperatures.

4.6.1 1 mm Stator Design

Although 0.7 mm MAS probes are typically considered to be the state-of-the-art ^{1}H-detection systems, they have practical limitations with respect to fabrication. Due to their size,

components for 0.7 mm MAS systems are extremely difficult to machine and are far more fragile than larger rotor systems. Rotors and bearings in particular are very difficult to fabricate out of zirconia at these sizes, and rotor crashes are more common for 0.7 mm MAS systems compared to larger rotor systems. Consequently, rather than attempting to fabricate 0.7 mm stators, it was decided to design a 1 mm stator system that would be more robust and easily machined. It is anticipated that this stator system should be capable of reaching MAS frequencies of 80-90 kHz at room temperature. A previously fabricated 1.3 mm spinning system was used as a base model for designing the 1 mm stator system. CAD drawings of the 1 mm stator can be seen in Figure 4.16.

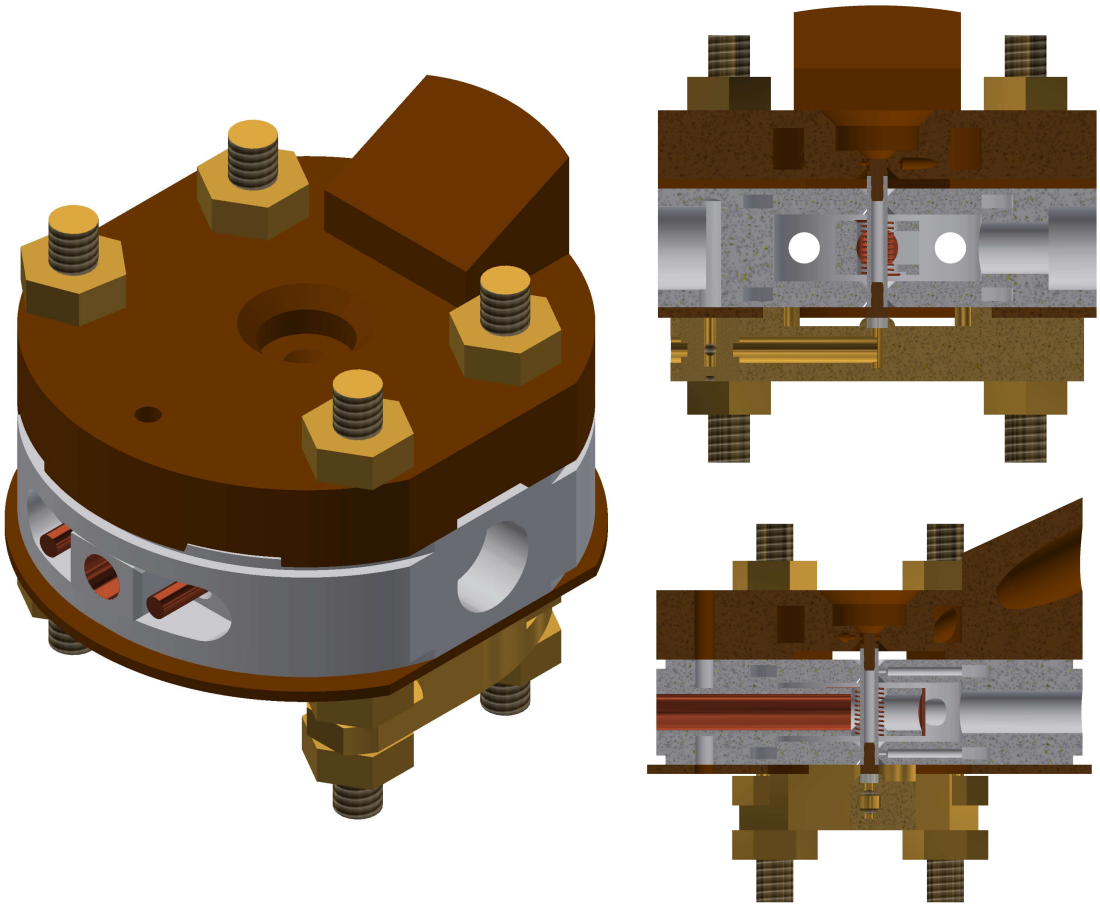

Figure 4.16: Diagram of 1 mm stator system. Images on the right represent cross-sectional view of the stator.

The stator's coil block is designed to deliver microwaves to the rotor via a smooth metallic waveguide in the front of the coil block. This design is similar to previous methods developed for 1.3 mm stator systems.[116] The coil block features a smooth, thin layer of metal that acts as a small waveguide to improve microwave coupling to the sample. The metallic waveguide may consist of a tube, foil, or even electroplated metal provided that the thickness of the metallic layer is appreciably thicker than the skin depth at the required microwave frequency. Another benefit of this coil block design is that it enables two microwave passes through the rotor. After the microwaves' initial pass through the rotor, a metallic mirror on the back of the coil block reflects and refocuses the microwaves back to the center of the sample to improve overall microwave absorption. Delivery of cooling gas to the sample can be accomplished via a hole in the side of the coil block. A CAD drawing of the coil block assembly can be seen in Figure 4.17.

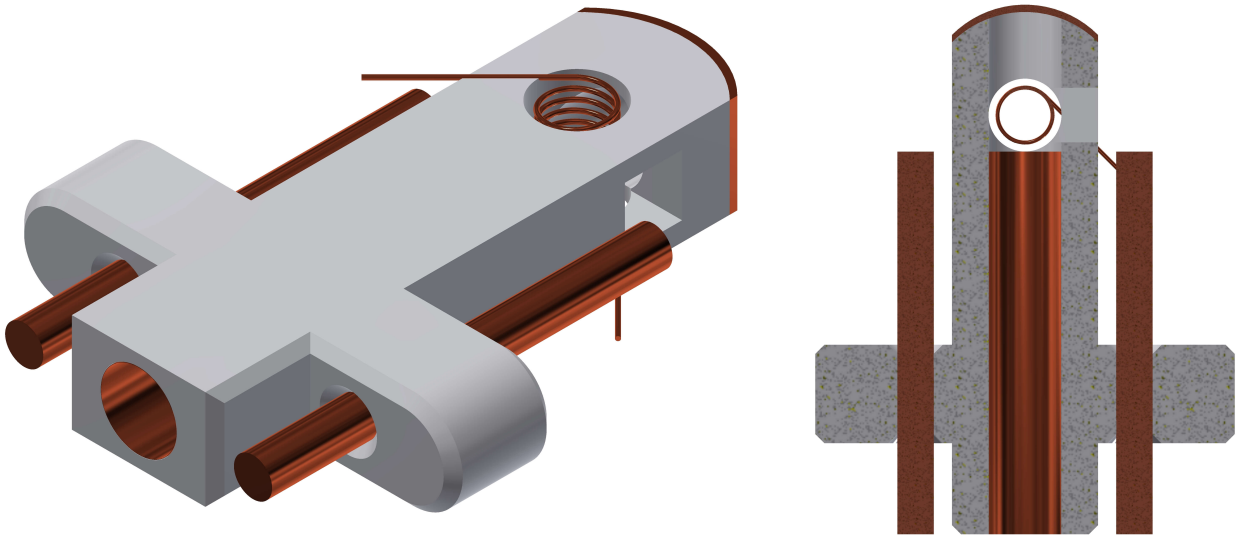

Figure 4.17: CAD drawing of 1 mm coil block assembly.

To improve the filling factor in the 1 mm system, the thickness of the coil block was maintained from the previous 1.3 mm system. In this way, the RF coil could be made longer, allowing for larger gaps between coil turns and a larger percentage of the rotor's sample volume to be captured within the volume of the coil. This was made possible by decreasing the thickness

of the bearings to 1.25 mm to accommodate the extra space. Three holes in the back of the stator can be used for any combination of items including exhaust, temperature sensors, and fiber optics for optical irradiation of the sample.

4.6.2 1 mm Rotor Design

The custom-designed 1 mm rotor was devised with reliability and machinability in mind. For a given rotor diameter, rotors with thicker walls and shorter lengths are capable of faster spinning. However, short, thick-walled rotors are capable of holding less sample, which decreases the sensitivity of the experiment. Therefore, a compromise must be made between maximizing the sensitivity of the experiment and maximizing the performance and reliability of the system. To obtain preliminary results, the rotor was designed to maximize the latter. For an in-depth review on rotor dynamics, see Section 6.2.2.

The inner diameter, outer diameter, and length of the rotor are 0.6 mm, 1 mm, and 6.3 mm respectively. The stem of the drive and end caps are both 1.2 mm in length, which gives the rotor an active sample volume of ~1.10 μL (~1.8x active sample volume of a 0.7 mm rotor). The stems on the drive and end caps are slightly oversized (OD = 0.605 mm) and contain grooves to create a tight fit and improve sealing of the rotor during spinning. A CAD drawing of the 1 mm rotor can be seen in Figure 4.18.

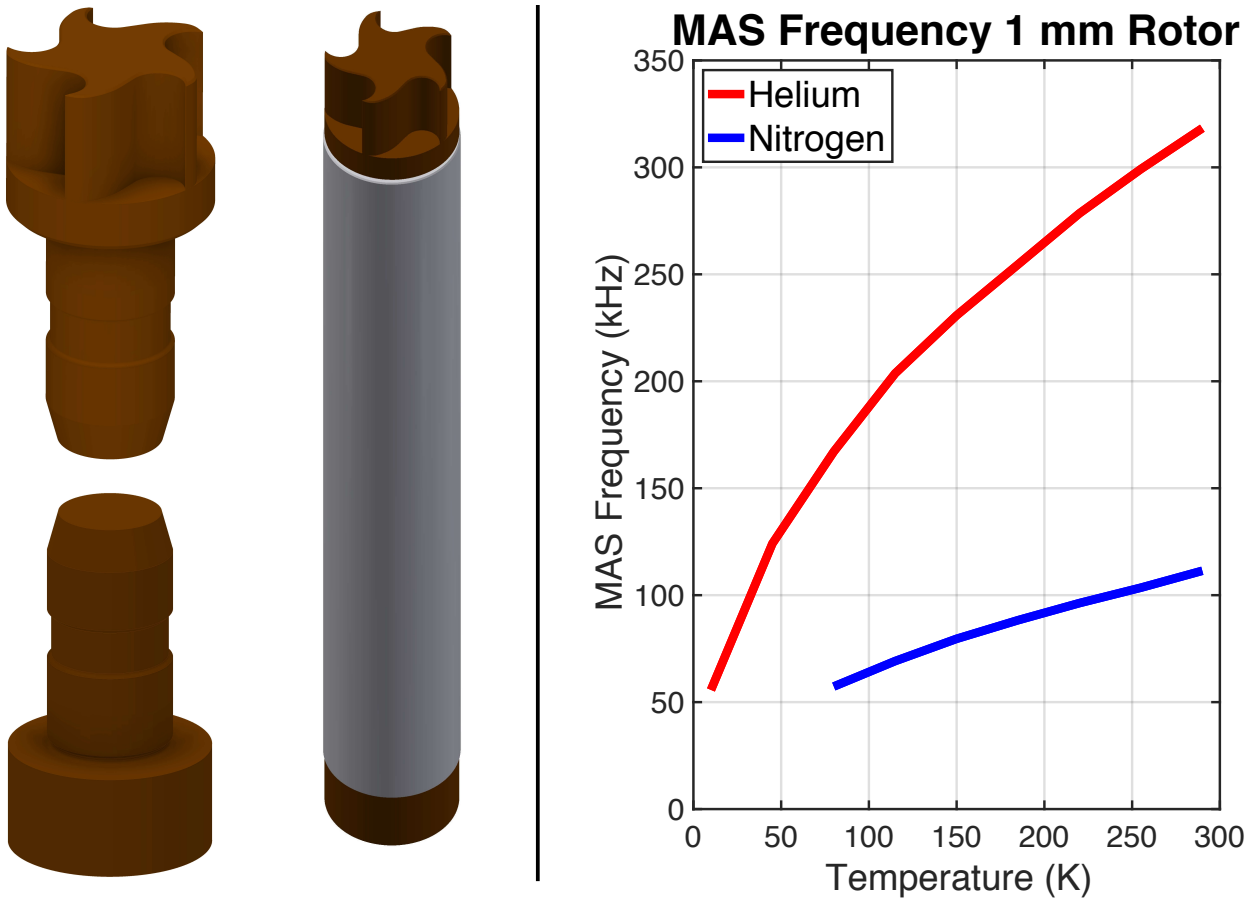

Figure 4.18: (Left) CAD drawings of 1 mm rotor design. (Right) MAS plot showing the theoretical maximum achievable spinning frequencies for an indestructible 1 mm rotor using helium and nitrogen gas as the spinning medium.

4.6.3 Fluid Dynamic Simulations

To verify that MAS frequencies >80 kHz would be achievable in the 1 mm stator system, computational fluid dynamic (CFD) simulations were performed. All simulations were performed in SOLIDWORKS Flow Simulation. For a thorough review of fluid dynamics in MAS systems, the reader is referred to other literature.[117] Two primary investigations were performed with these simulations. The first was to confirm that the flow of fluid in the turbine region was smooth and that no turbulent regions were observed. The second was to check if fluid flow in the turbine region exceeded the speed of sound in the fluid (Ma > 1).

Similar simulation parameters that have been used in prior fluid dynamic simulations were employed.[117] The rotation frequency of the rotor was set to 90 kHz. The flow type model was set to laminar and turbulent with nitrogen gas as the system fluid. The walls of the system were considered to be adiabatic, and the temperature of the system was set to 293.2 K. The mass inlet flow rate of the gas was set to 5 x 10^{-4} kg/s, and the pressure at the top and bottom outlets of the turbine region were set to 1 atm. The results of the simulations can be seen in Figure 4.19.

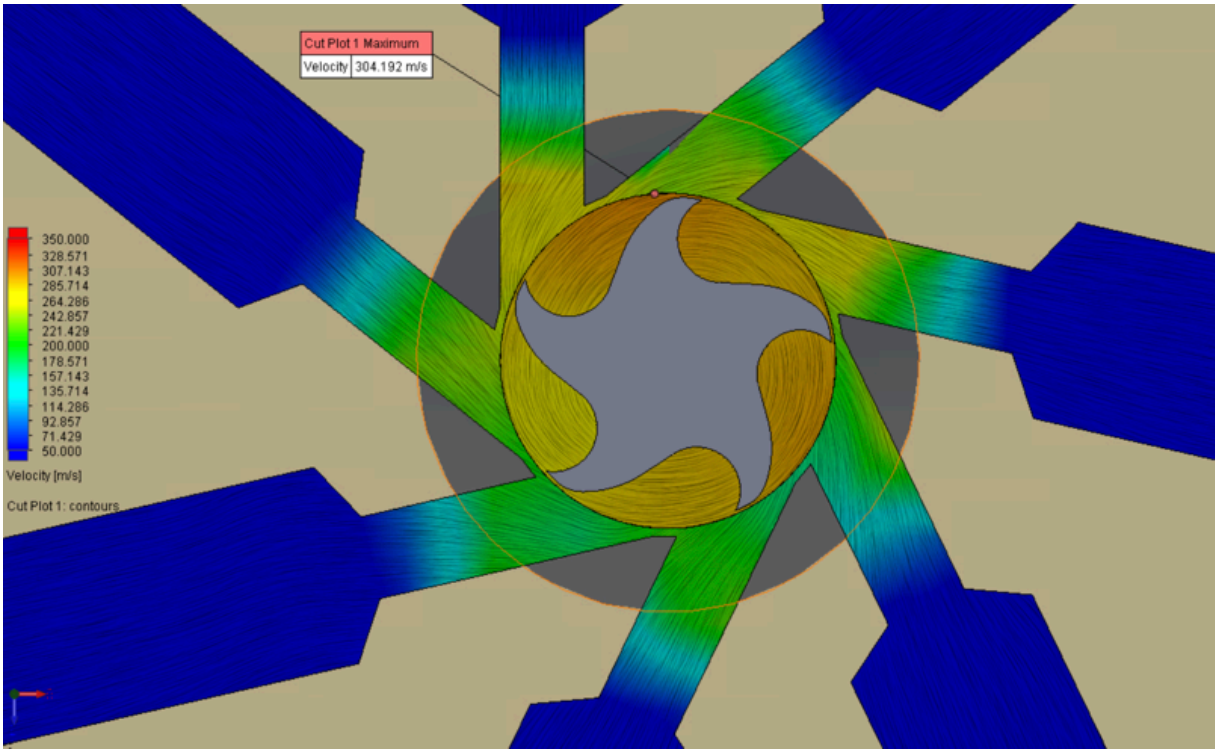

Figure 4.19: CFD simulation results for the custom-designed 1 mm rotor spinning at 90 kHz.

The CFD simulations for the 1 mm rotor spinning at 90 kHz revealed promising results. Based on the simulations, fluid flow in the turbine region appears to be smooth, and no pockets of instability can be observed. MAS > 90 kHz may therefore be achievable with a properly designed, sufficiently strong rotor. Additionally, at the mass flow rate and spinning frequency used in the simulation, the speed of the fluid in the turbine region remains subsonic. These results indicate that the 1 mm rotor should spin comfortably at MAS frequencies between 80-90 kHz.

4.7 Conclusions & Future Work

In this chapter, a novel design for a fast-spinning MAS DNP probe was presented. This probe is designed to be compatible with a helium recirculation system and should be capable of spinning samples stably at MAS > 80 kHz. Further improvements to the system could be made to take advantage of the properties of helium, such as the addition of a cryostat along the VT line to house cryogenic preamplifiers. Future work may also include expanding the probe circuit to four channels to add another nuclear frequency to the circuit such as ^{31}P or ^{2}H.

The 1 mm stator system may benefit from further optimization via CFD simulations. In this study, the purpose of the simulations was to confirm via modeling that the turbine system, as designed, would spin stably at MAS frequencies > 80 kHz. No simulations were run to study the frictional power loss in the radial bearing system or to optimize the turbine beyond its original design. Future studies may vary different parameters such as drive nozzle diameters and angles as well as the number of turbine grooves and their respective curvature.

Another aspect of the 1 mm stator that could be further optimized is the radial gas bearings for helium spinning. The frictional power loss in a turbine system can be calculated using the equation

$$P_f = \frac{8\mu\pi^3 r_r^3 f^2}{r_c} \qquad \textbf{4.7}$$

where μ is the dynamic viscosity of the gas, r_r is the radius of the rotor, f is the rotation frequency in Hz, and r_c is the radial clearance between the rotor and radial bearing.[117] It can be clearly observed that as the viscosity of the gas increases, the radial clearance between the rotor and radial bearing must also increase in order to prevent an increase in the frictional power loss. At room temperature, the difference in viscosity between helium and nitrogen gas is not substantial enough to warrant a redesign of the stator system. At 100 K however, the viscosity of helium is

approximately 40% greater than the viscosity of nitrogen.[118] Therefore, for stator systems intended for DNP applications, consideration should be given towards increasing the radial bearing clearance, either by increasing the inner radius of the radial gas bearing or by decreasing the diameter of the MAS rotor. While increasing the radial bearing gap will consequently lower the natural frequency of the rotor, at low temperatures the rotor's spinning frequency should be limited more by the density of the driving fluid rather than the critical speed of the rotor.

4.8 Chapter-Specific Acknowledgements

There are several people I would like to thank that helped make this project possible. First, I'd like to thank Eric Keeler, whose amazing work on ^{17}O NMR helped to inspire this project. I'd like to thank Christy George and Marcel Reese for their help with the probe design and simulations. Christy was always willing to answer any questions I had regarding previous probe designs and greatly aided my understanding of balanced transmission line circuitry and simulations. Marcel Reese wrote a preliminary version of MATLAB code to help select different stepped inner conductor designs and was very helpful with troubleshooting HFSS issues when designing the N-type adapters. I'd also like to thank Brian Michael and Natalie Golota for helpful discussions. Natalie was especially helpful in making improvements to the probe design.

4.9 MATLAB Code for Stepped Transmission Line Calculations

An example of the MATLAB code used to design a transmission line with a stepped inner conductor is provided below/on the following pages.

```
clear all
clc
tic

%%%%%%%%%%%%%%%%%%%%%%%%%%%%%%%%%%%%%%%%%%%%%%%%%%%%%%%%%%%%%%%%%%%%%%%%%%%%

ocd=0.620;                                      %Inner diameter of outer
conductor
icdmin=0.120; icdmax=0.500; icdinc=0.001;   %Minimum, maximum, and increments
of outer diameter possible for inner conductor

nchn=3;                                 %Number of channels on probe
sections=5;                             %Number of desired sections in inner
conductor
totplc=28.3;                            %Inner conductor total length constraint
in inches
plmin=1; plinc=0.001; plmax=10;     %Physical Length range of inner conductor
sections
perm=1000000;                           %Number of inner conductor permutations to
find
findlim=1;                              %Number of inner conductor combinations to
find before code quits
Zmcut=0.5;                              %Cutoff impedance for the sum of tee
impedances of all channels

myf=[500.058 125.739 50.67];        %RF freqeuncies of probe in MHz
Zsc=[0-116j 0+13.2j 0-58.5j];       %Sample chamber impedance

Zcut=20;                                %Cutoff impedance between using air and
PTFE dielectric in inner conductor
Z0base=50;                              %Characteristic impedance of first section
of inner conductor
Z0top=50;                               %Characteristic impedance of last section
of inner conductor
tdT=[86 86 87];                         %Time delay (in picoseconds) of T-arm at
each frequency
Z0T=50;                                 %Characteristic impedance of T-arm

%%%%%%%%%%%%%%%%%%%%%%%%%%%%%%%%%%%%%%%%%%%%%%%%%%%%%%%%%%%%%%%%%%%%%%%%%%%%
permlim=1000000;
found=0;
while found<findlim
if perm>permlim
    disp('Number of permutations exceeds permlim max: Please choose smaller
number')
else

%Calculation reference values
c=299792458;                            %Speed of light (m/s)
myfhz=myf.*1e6;                         %Convert RF frequencies from MHz to Hz
la=c./myfhz;                            %Reference wavelengths
in2m=0.0254000508;                      %Constant (inches/meter) - use for unit
conversions in conductor lengths
permcount=0;
f0=myfhz(1);
la0=la(1);
bl=tdT*.000000000001.*myfhz*2*pi;
```

```
%Creates Z vector for reflection calculations
icd=(icdmin:icdinc:icdmax);                 %Outer diameter of inner
conductor
kair=1; kptfe=2.1;                          %Dielectric constants of air and
PTFE
Z0air=(138/sqrt(kair)).*log10(ocd./icd);    %Characteristic impedance of air-
filled transmission line
Z0ptfe=(138/sqrt(kptfe)).*log10(ocd./icd);  %Characteristic impedance of
PTFE-filled transmission line

%Variable preallocation
G1=zeros(1,nchn);
G2=zeros(1,nchn);
Zf=zeros(1,nchn);

Results=zeros(8,sections);
rowNames = {'Section Number','Physical Length (inches)','Chracteristic
Impedance (Ohms)','_________________','Frequency (MHz)','Impedance
Magnitude','Impedance','Reflection Coefficient'};
sectionnum=(1:1:sections);
Results(1,1:sections)=sectionnum;

Z0=Z0air;

for k=1:length(icd)
    if Z0(k)<=Zcut
        Z0(k)=Z0ptfe(k);
    end
end

plperms=zeros(perm,sections-1);         %Creates matrix for length
permutations
Z0perms=zeros(perm,sections);           %Creates matrix for impedance
permutations
plpermsnew=zeros(perm,sections);

for z=1:perm
randZ=randi(length(Z0),1,sections);     %Creates random number vector to
select random impedances
Z0perms(z,:)=Z0(randZ) ;                %Creates matrix with random
permutations of impedances
end

plr=(plmin:plinc:plmax);           %Physical length range. Defines the
physical length range of each section in inches

while permcount<perm
randpl=randi(length(plr),1,sections-1);   %Creates random number vector to
select random physical length
plperms(permcount+1,:)=plr(randpl);       %Creates matrix with random
permutations of lengths
    if (sum(plperms(permcount+1,:))>=totplc-plmax) &&
(sum(plperms(permcount+1,:))<=totplc-plmin)
        plpermlast=totplc-sum(plperms(permcount+1,:));
        plpermsnew(permcount+1,:)=[plperms(permcount+1,:) plpermlast];
```

```
        permcount=permcount+1;
    end
end
toc
elperms=plpermsnew./la0;
Z0perms(:,1)=Z0base;
Z0perms(:,sections)=Z0top;
elperms=elperms.*in2m;

for l=1:length(elperms)
    for m=1:sections
        if Z0perms(l,m)<=Zcut
            elperms(l,m)=elperms(l,m).*sqrt(kptfe);
        end
    end
end

for r=1:size(elperms,1)
 L=elperms(r,:);
 Z=Z0perms(r,:);
 G1=multiline([Z0T Z],L,Zsc,myfhz/f0);       %Calculates reflection
coefficient given vector of characteristic impedances, electrical lengths,
load impedance and reference frequency
 Zic=gamma2z(G1);                                %Converts reflection
coefficient to impedance - gamma2z is built-in MATLAB command

 for n=1:nchn
     Zf(n)=zprop(Zic(n),Z0T,bl(n));
 end

 Zm=abs(Zf);

 if (sum(Zm)<Zmcut)
    Results(2,1:sections)=plpermsnew(r,:);
    Results(3,1:sections)=Z;
    Results(5,1:length(myf))=myf;
    Results(6,1:length(Zm))=Zm;
    Results(7,1:length(Zf))=Zf;
    Results(8,1:length(G1))=G1;

    Results(Results==0)=NaN;
    FinalResultTable = array2table(Results,'RowNames',rowNames);
    writetable(FinalResultTable,'outputfile.txt');

    found=found+1;
 end
end
end
found
toc
end
disp('Calculations Complete')
toc
```

5 Design of a Helium Recirculation System for MAS DNP

5.1 Abstract

The unique properties of helium could unlock new frontiers in MAS DNP spectroscopy. The usage of helium gas to cool RF electronics and spin MAS rotors should provide substantial enhancement in spectral resolution and potentially orders of magnitude improvement in sensitivity for MAS DNP experiments. Unfortunately, due to the high cost of helium, extended experiments that consume helium are often prohibitively expensive. This chapter describes a design for a helium recirculation system for MAS DNP experiments that allows recycling of helium instead of single-use consumption. This system will be used to perform MAS experiments on a 1 mm DNP probe and should enable spinning frequencies >80 kHz at 100 K.

5.2 Introduction & Motivation

Helium has the potential to substantially improve the sensitivity and resolution of MAS DNP experiments. The speed of sound in helium is nearly three times that of nitrogen gas, which should allow a MAS rotor to spin approximately three times faster using helium gas compared to nitrogen. Additionally, helium is capable of being cooled to ~4 K before liquefying, a property that can be utilized to substantially improve the sensitivity of MAS DNP experiments via cooling of the sample and electronics.

Recall from Equation 1.10 that the Boltzmann polarization for nuclear spins scales inversely with respect to temperature. If, for example, an NMR sample were cooled from room temperature (~293 K) down to 30 K, one should expect an approximately ten-fold increase in sensitivity as a result. Furthermore, longer relaxation times at low temperatures may lead to significantly improved DNP enhancements. This is demonstrated in Figure 5.1, in which

enhancements on silica nanoparticles and urea samples at 30 K are approximately three-fold higher than the observed enhancements at 90 K.[119]

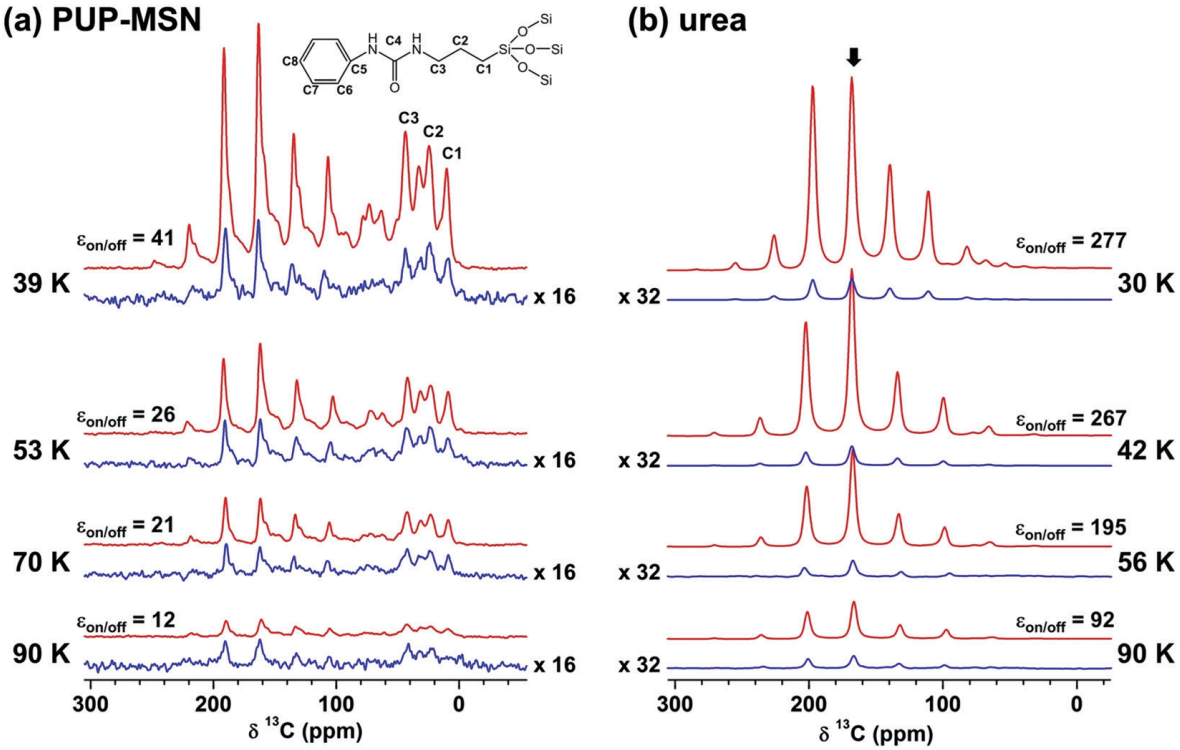

Figure 5.1: DNP enhancements at temperatures from 30-90 K. (a) 1D DNP spectra of silica nanoparticles immersed in a solution of deionized water with 10 mM AMUPol. (b) DNP 1D DNP spectra of ^{13}C-labeled urea in a glycerol/water matrix with 10 mM AMUPol. Reprinted with permission.[119]

In addition to the sensitivity enhancements that can be achieved by cooling the sample with helium gas, there are substantial benefits to cooling the electronics in the probe circuit as well. The signal-to-noise with respect to temperature in an NMR probe circuit scales as

$$S/N \sim \frac{1}{\sqrt{T_c R_c + T_a[R_c + R_s] + T_s R_s}} \qquad \textbf{5.1}$$

where T_c is the RF coil temperature, R_c is the resistance of the RF coil, T_a is the noise temperature of the preamplifier, T_s is the sample temperature and R_s is the resistance added to the coil by the sample, otherwise known as the "sample resistance".[120] Cryogenically cooled solution NMR probes are known to enhance the signal-to-noise of NMR spectra by a factor of 2-4 by cooling the coil and preamplifier in the circuit to very low temperatures (~20 K) with helium gas. The recent

development of cryogenically cooled probes for MAS NMR has likewise seen similar increases in signal-to-noise by similar means.[121] Example MAS spectra acquired with a cryoprobe compared to a standard room temperature probe can be seen in Figure 5.2. An excellent review of cryogenically cooled probes can be found in other literature.[122]

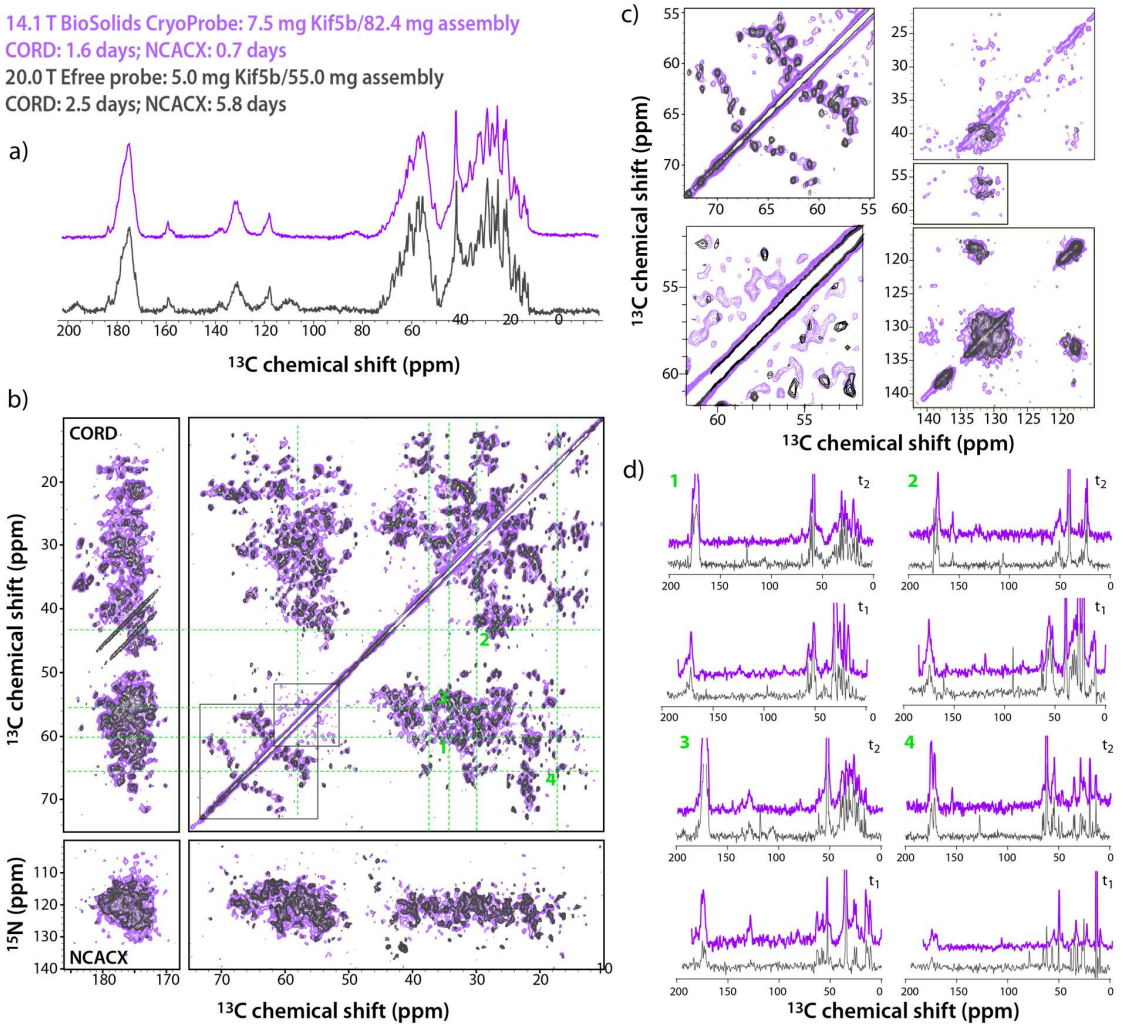

Figure 5.2: Spectral comparison of MAS NMR spectra recorded with the CPMAS cryoprobe at 14.1 T vs. a standard room temperature probe at 20.0 T. Spectra were recorded on a sample of kinesin Kif5B microtubules. Reprinted with permission.[121]

The benefits of helium are not limited to its cryogenic properties. Helium can also be used to improve the resolution of NMR spectra via faster MAS. Average Hamiltonian theory (AHT) predicts that spectral linewidths should narrow as $2\pi/\omega_r$, where ω_r is the spinning frequency of the rotor.[10] This has been confirmed experimentally for spinning frequencies up to 170 kHz.[123, 124]

Figure 5.3 shows the maximum achievable spinning frequency for a range of rotor sizes using helium and nitrogen as the spinning medium. It can be clearly seen that, especially for smaller rotor sizes, using helium gas for MAS can lead to substantially higher spinning frequencies and by extension, substantially improved spectral resolution.

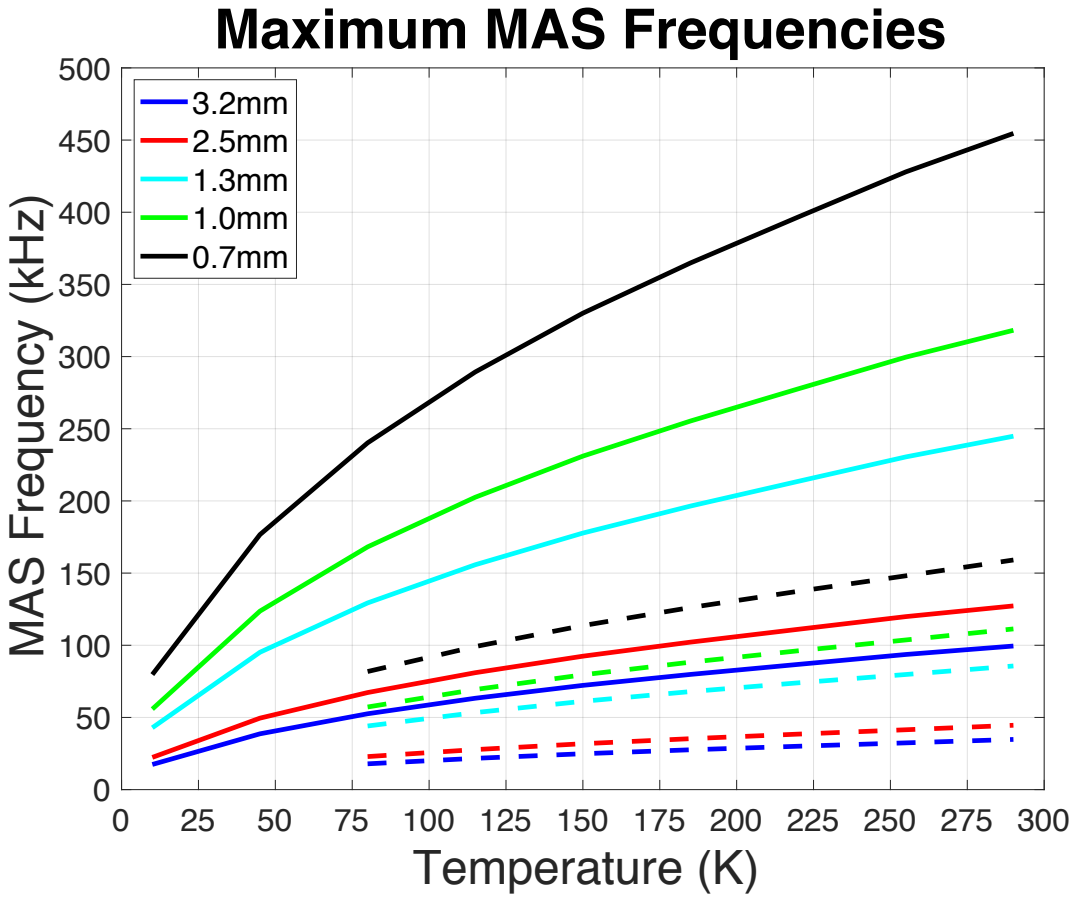

Figure 5.3: Maximum theoretical spinning frequencies for different rotor sizes as a function of temperature. Solid lines represent spinning frequencies achievable with helium gas. Dashed lines represent spinning frequencies achievable with nitrogen gas.

For smaller rotor sizes (<1.3 mm), MAS frequencies >100 kHz are achievable at 100 K. Such spinning frequencies allow for ^{1}H-detected DNP experiments on biological systems, a significant feat, as ^{1}H-detection can increase the sensitivity of the experiment by a factor of $(\gamma_H/\gamma_C)^{3/2} \sim 8$ compared to equivalent carbon detection. This improved sensitivity can be compounded with the increased enhancements discussed previously due to cryogenic cooling of

the sample and circuit. When factoring in ^{1}H detection with improved nuclear spin polarization, improved DNP enhancements, and reduced noise in the probe circuitry, gains in signal-to-noise of > 10,000 are not unreasonable. At this sensitivity level it may even become feasible to record multidimensional NMR spectra on natural abundance samples.

The challenge with using helium gas for MAS DNP is primarily an engineering issue. Helium is the smallest atom and consequently has the potential to leak through even well-designed seals. This becomes especially problematic at cryogenic temperatures where sealing options are more limited. Additionally, using helium for MAS requires high mass flow rates at high pressures (>90 psi). Designing a system that is helium-leak tight at these pressures and temperatures is extremely challenging. This chapter discusses equipment and methods for building a helium recirculation system and the potential difficulties as well as solutions.

5.3 Helium Recirculation System Layout

5.3.1 Previous Helium Systems

A limited number of systems that use helium gas for MAS and DNP have previously been demonstrated. Such systems utilize both recirculating and non-recirculating helium. Perhaps the most well-known non-recirculating helium system is that by Thurber and Tycko as seen in Figure 5.4.[125-127] This design uses nitrogen as the spinning gas while using liquid helium boil-off to cool the sample and RF coil. The helium boil-off is delivered via a line inserted into the center of the stator. The 4 mm stator features an elongated rotor to create further separation between the warmer nitrogen gas (~80 K) and the colder helium boil-off gas. For a 4 mm rotor, sample temperatures of 25 K have been achieved at MAS frequencies up to 7 kHz. The helium consumption rate is kept low at <1.3 l/hr. Remarkably, an approximately ten-fold increase in the DNP enhancement was observed for the triradical DOTOPA-Ethanol when cooling the sample from 90 K to 30 K.

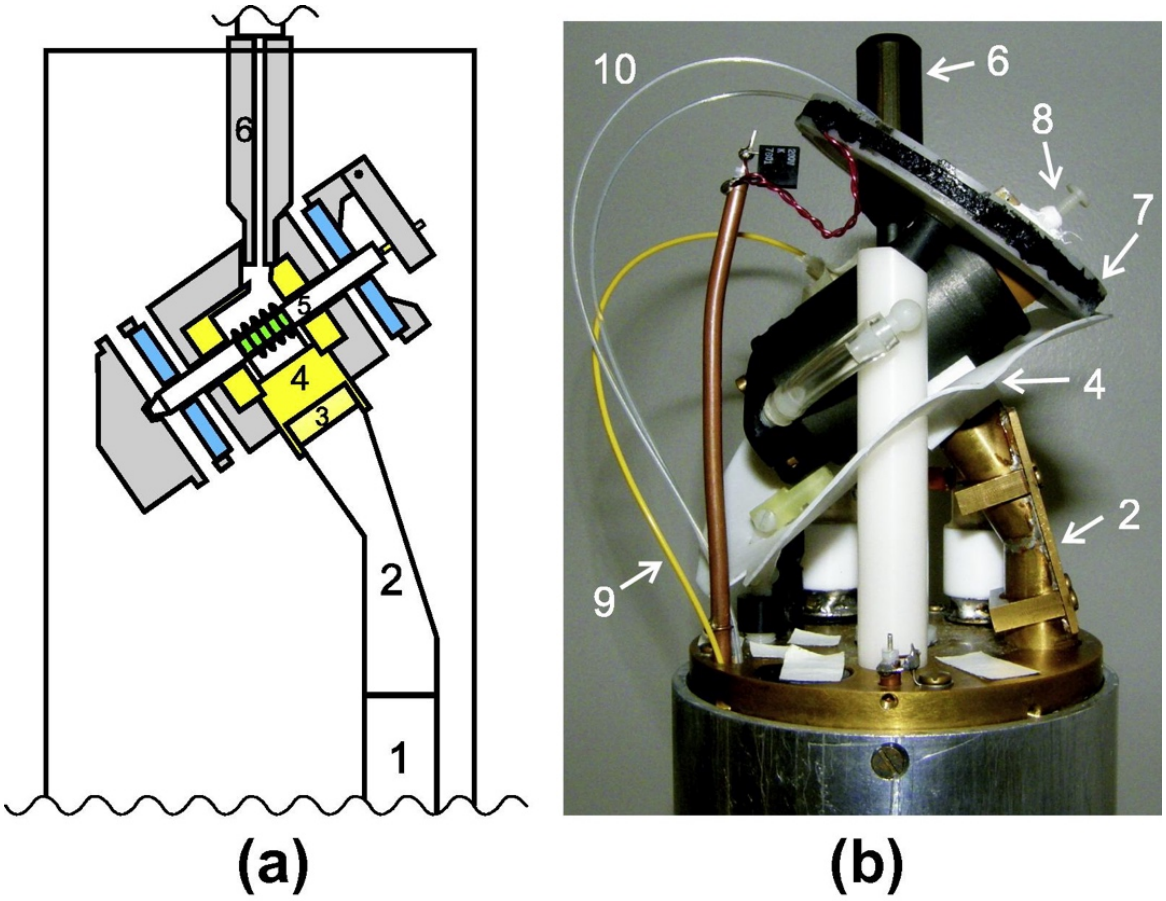

Figure 5.4: Thurber and Tycko cryogenic probe design. (a) Schematic representation of helium-cooled probe with waveguide. (b) Photograph of helium-cooled DNP probe. The helium supply line is indicated by the number 6 in the figure. Reprinted with permission.[126]

The Barnes group has performed numerous DNP experiments at temperatures <6 K using helium without a recirculation system.[59, 128-130] This includes in-cell DNP experiments on intact human cells where DNP enhancements >40-fold were achieved. The Barnes group has also used helium gas to spin MAS spheres to frequencies significantly higher than what is achievable with nitrogen gas.[72, 73] Using helium gas as the spinning medium, 4 mm MAS spheres have been spun to frequencies >28 kHz, which is substantially higher than was is achievable for a standard 4 mm cylindrical rotor.

Helium recirculation systems for MAS NMR and DNP have been pioneered by the groups in Osaka and Grenoble. Examples of these systems can be seen in Figure 5.5. Gaël de Paëpe and co-workers have developed and built two helium recirculation systems, NUMOC and

SACRYPAN, which are capable of performing MAS DNP experiments at temperatures as low as 30 K.[115, 131, 132] NUMOC was a prototype system used to demonstrate the feasibility of a closed-cycle helium system for DNP applications. In the NUMOC design, cooling of the input gas is accomplished via a heat exchanger that contains an external supply of liquid helium. Using NUMOC, spinning frequencies of 25 kHz were achieved on a 3.2 mm system at 90 K. SACRYPAN differs from NUMOC in that it uses cryocoolers rather than an external supply of liquid helium to cool the sample to < 77 K. Both NUMOC and SACRYPAN utilize return gas from the probe to cool the RF electronics in the probe as well as shield the incoming gas.

Yoh Matuski and co-workers have also had success building helium DNP systems.[119, 133, 134] Like the Grenoble systems, the Osaka helium recirculation system has been used to perform MAS DNP experiments at 30 K and utilizes return gas to cool the RF electronics as well as assist with cooling of the input gas from the heat exchanger. An advantage of the Osaka system is that the cryogenic helium circulation (CHC) unit, which contains the cryocoolers and helium compressors, can be transported easily to different spectrometers via casters on the bottom of the unit. Since the system is a closed helium loop, the only costs to run the system are due to power consumption, which are estimated to be ~$3/h.

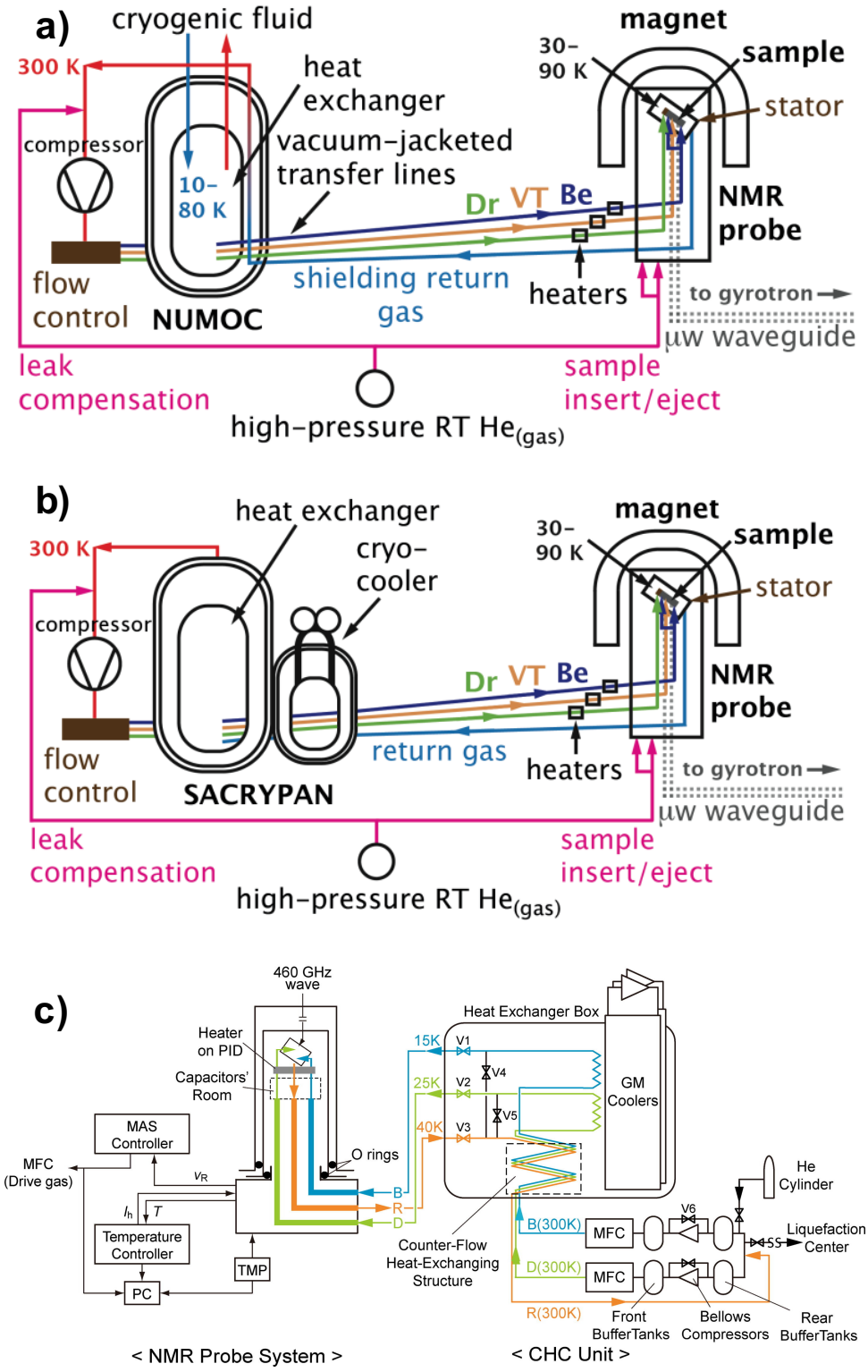

Figure 5.5: Previous helium recirculation designs. (a,b) NUMOC and SACRYPAN helium recirculation systems.[115] (c) Osaka helium recirculation system design.[134] Figures modified with permission.

5.3.2 Current Design

Building upon previous systems demonstrated in the literature, we have designed the helium recirculation system schematically depicted in in Figure 5.6. The components of the system were all chosen to ensure that the required helium specifications could be met and that leaks in the system would be minimized. A significant percentage of the system is intended to be controlled via LabVIEW programs or other automation programs of choice. A detailed description of the individual sections of the recirculation system is provided in the following sections.

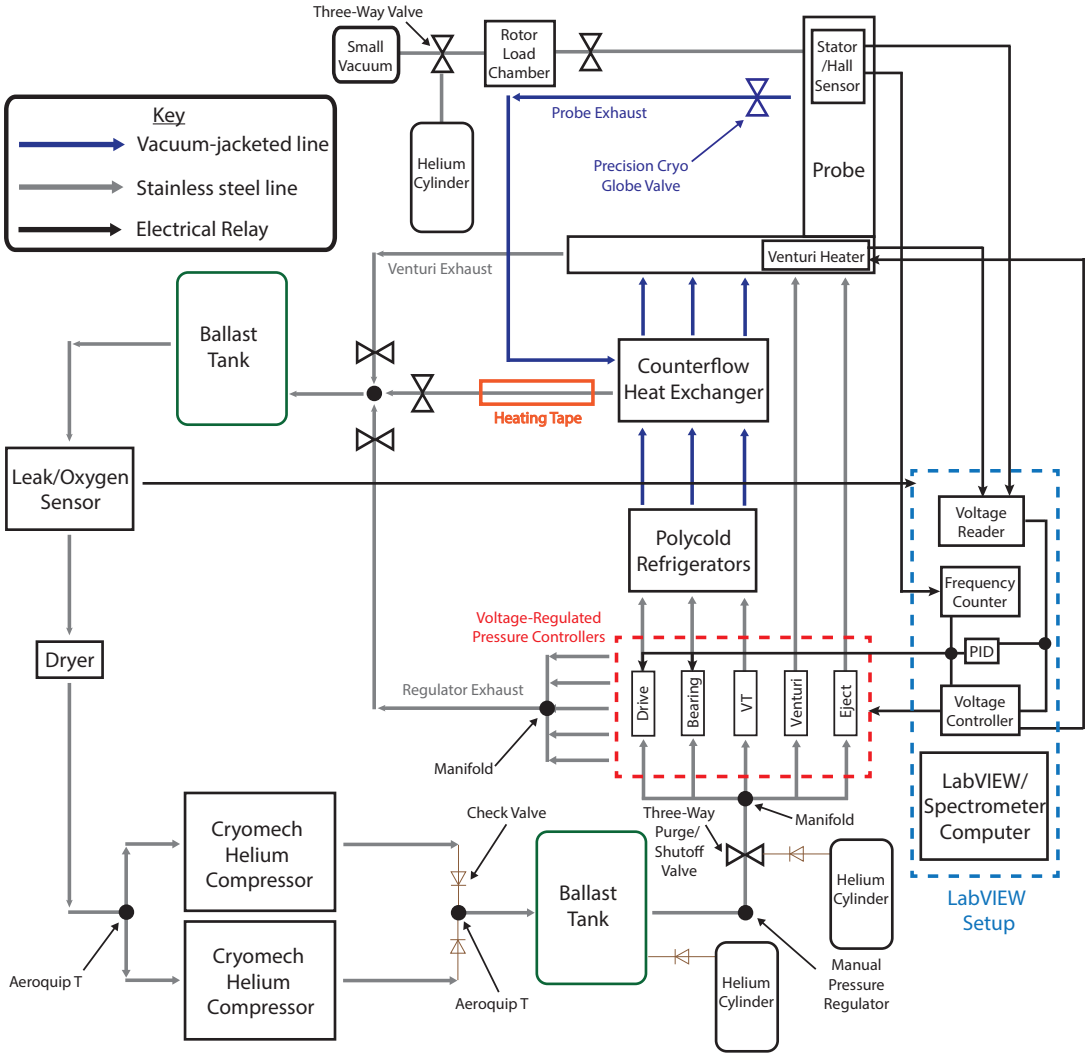

Figure 5.6: Schematic representation of current helium recirculation system design.

5.3.3 Helium Compressors & Adapters

Two CPA286i helium compressors, purchased from Cryomech (Syracuse, US), form the heart of our helium recirculation system. The mass flow rate required to drive a MAS system can be calculated from the ideal gas law

$$\dot{m} = \frac{MP\dot{V}}{RT} \qquad \textbf{5.2}$$

where $\dot{m}$ is the mass flow rate, M is the molar mass of the gas, P is the pressure, $\dot{V}$ is the required volume flow rate, R is the ideal gas constant, and T is the temperature of the gas. From conversations with Yoh Matsuki and Gaël de Paëpe, it was estimated that the mass flow rate required to drive the 1 mm system is between 0.7-1.0 g/s. The Cryomech compressors are each capable of outputting helium gas at 100 psig of pressure with a variable flow rate between 0-0.9 g/s depending on the desired power consumption. By running the compressors in parallel, the total helium output of the system can be adjusted from 0-1.8 g/s. Each of the compressors utilizes helium-tight Aeroquip fittings. Custom Aeroquip tees and adapters were fabricated to allow the compressors to be run in parallel and mated with the NPT ports of a ballast tank.

Figure 5.7: Helium compressors (left) and Aeroquip adapters (right) for helium recirculation system.

5.3.4 Counterflow Heat Exchanger

A counterflow heat exchanger was constructed based on a similar design to Albert et. al.[135] A diagram of the heat exchanger design can be seen in Figure 5.8. The purpose of the heat exchanger is to cool the helium gas to low temperatures (<100 K) for DNP experiments. Before the helium gas enters the heat exchanger, it is passed through a Polycold gas chiller that pre-cools the gas to 150-180 K. The heat exchanger is then further cools the gas to temperatures as low as 77 K.

The counterflow heat exchanger features three separate modules (bearing, drive, and VT) that sit in a bath of liquid nitrogen. Each module has a two-stage cooling system. The first stage is equipped with two heat exchanger coils, one inside the other. The space between the inner and outer coil utilizes return gas to pre-cool the gas before entering the second stage. A vacuum chamber thermally insulates the first cooling stage from the liquid nitrogen bath, preventing unnecessary boil-off. The second stage contains a heat exchanger within a can of pressurized nitrogen. The pressure of the nitrogen in the can be regulated to control the level of liquid nitrogen, which in turn controls the temperature of the output gas. Higher levels of liquid nitrogen in the can will lead to increased cooling, while lower levels will result in warmer gas temperatures.

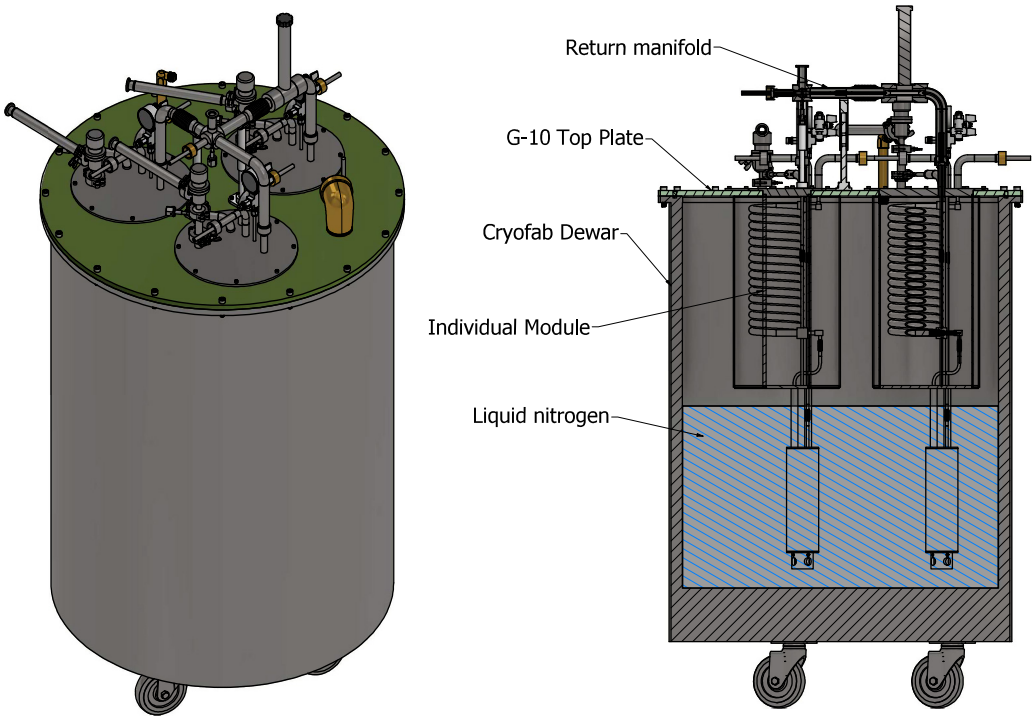

Figure 5.8: Diagram of counterflow heat exchanger. The heat exchanger is used to cool the helium gas down to temperatures of approximately 77 K. Figure courtesy of Natalie Golota.

5.3.5 Sample Exchanger

The exchange of samples in the DNP probe can potentially introduce air into the system, a problem that must be addressed to avoid consequences such as the condensation of oxygen. A custom sample exchanger was designed to circumvent this issue and aid with ejection of the rotor. A schematic representation of the sample chamber can be seen in Figure 5.9. The procedure for removing a rotor from the sample chamber is as follows: first, the cryogenic exhaust valve should be shut off and the three-way purge valve should be set to the "off" position. This closes off the probe, heat exchanger, and Polycold gas chillers from the rest of the system. Next, with the sample exchanger's ball valve closed, a vacuum can be pulled on the rotor chamber. Once the chamber is evacuated, the ball valve can be opened, and the rotor should be pulled into the chamber by the vacuum. If the vacuum is insufficient, additional helium gas may be pushed through the Venturi

line to aid with ejection. After the rotor has ejected into the rotor chamber, the ball valve may be shut off again.

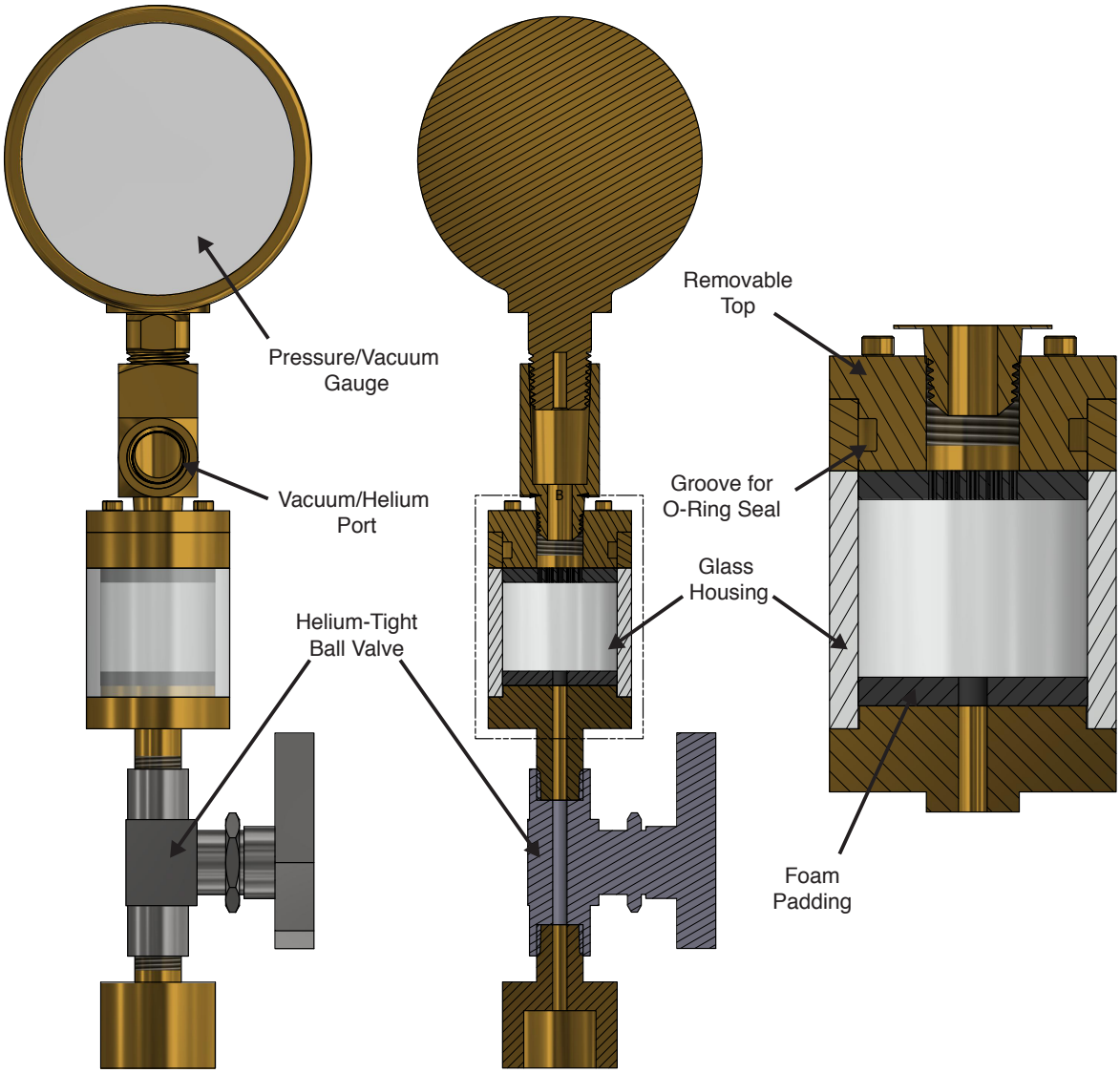

Figure 5.9: Sample exchanger assembly. This apparatus can be used to insert and eject rotors without introducing air into the system.

To insert the rotor, the reverse procedure is used. First, the rotor should be inserted such that it is sitting on top of the ball valve. Next, a vacuum can slowly be pulled on the rotor chamber to evacuate any air from the system. The sample chamber can then be back-filled with helium gas at low pressure. Once the chamber is filled with helium, the ball valve may be opened to allow the sample to insert. If the rotor is having difficulty entering the stator, the rotor chamber can be

pressurized at higher pressure, and the ball valve may be quickly opened and shut to provide bursts of helium to insert the rotor.

5.3.6 Additional Components

For a detailed review of the DNP probe and the methods used to create helium-tight seals, please see Section 4.4.5. After passing through the counterflow heat exchanger, the gas may require additional warming to reach room temperature. This may be accomplished by passing the gas through an additional heating chamber that contains a copper coil wrapped in heating tape or a hot water bath for example. Introducing impurities such as air or water to the system may result in buildup of ice or liquid oxygen in the system. The former can impact the functionality of the system and the latter is a significant safety hazard. For this reason, an oxygen detector is included in the design. Oxygen sensors typically require that the input gas be at low pressure and close to room temperature, so the sensor is placed before the input of the compressors rather than the input to the heat exchanger. Assuming it can be properly sealed, an optional dryer may be added prior to the compressors as well to remove any water vapor that may leak in.

5.3.7 Helium Leak Testing of Flex Lines

Helium leaks in areas with NPT fittings were a major concern for the system. While flex lines can be purchased with more secure VCR fittings, these lines are more than an order of magnitude more expensive than lines with NPT fittings. To characterize the extent of helium leakage, a braided stainless steel hose with NPT fittings was purchased from McMaster-Carr and helium leak tested with different thread sealants. An NPT to VCR adapter was attached to one end of the line to additionally test the performance of VCR fittings under a pressurized helium environment. Of the sealants tested, Torr Seal showed the best performance. Using a helium leak

detector, no leaks were observed in the epoxy-sealed NPT fitting or the VCR fitting over an extended period of time.

5.4 Future Work

Future work will involve further assembly of the helium recirculation system, which will require automation of the pressure regulation of helium gas for MAS and performance of additional leak testing of recirculation system components. Additionally, an operating environment must be created to control and operate the system. This can be accomplished using LabVIEW or another program of choice. Upon confirmation that the system functions and is free of helium leaks, consideration should be given to constructing an additional counterflow heat exchanger, consisting of a Gifford-McMahon or pulse tube helium cryocooler, to allow for low temperature experiments down to 10 K. Such cryocoolers require a dedicated helium compressor for operation, but due to the presence of the Polycold refrigerators and nitrogen counterflow heat exchanger, the required cooling capacity should be reduced dramatically.

5.5 Chapter-Specific Acknowledgements

I would like to thank Gaël de Paëpe and Yoh Matsuki for helpful discussions regarding their helium recirculation systems and the necessary requirements to power a MAS system with helium. I would also like to give a huge thank you to Natalie Golota who designed the counterflow heat exchanger and provided several helpful discussions and suggestions regarding the design of the helium recirculation system.

6 Fabrication of Diamond MAS Rotors

6.1 Abstract

The choice of material for MAS rotors has important consequences related to the maximum achievable spinning frequency and microwave transparency of the rotor for MAS DNP experiments. Traditionally, rotors for MAS NMR and DNP have been fabricated from materials such as zirconia, sapphire, and silicon nitride among others. Due to its high strength, thermal conductivity, and transparency to microwave radiation, diamond is an ideal material choice for fabricating rotors for MAS DNP. This chapter presents a novel laser machining method for fabricating MAS rotors and drive caps from chemical vapor deposition (CVD) diamond. An in-depth description of the machining apparatus and parameters are provided, and preliminary fabrication results are shown.

6.2 Introduction & Motivation

Since the inception of MAS NMR in the 1950s, techniques for fabricating MAS rotors have improved significantly. At the time of this writing, the smallest rotor size found in the literature is 0.5 mm and MAS frequencies >170 kHz are now achievable.[123] There are generally two limiting factors that determine the maximum spinning frequency of a rotor: (1) the speed of sound in the driving medium and (2) the strength of the rotor material. The former can be improved upon by using gases such as helium for MAS experiments rather than air or nitrogen. Improving the latter is more difficult given the difficulties in machining high-strength materials such as ceramics.

At spinning frequencies >100 kHz, line broadening from strong ^{1}H-^{1}H homonuclear dipolar couplings is significantly reduced, and the resolution of ^{1}H MAS NMR spectra is greatly improved.[136-138] Furthermore, recent literature has suggested that at MAS frequencies >300 kHz,

it is possible to obtain solution-like resolution in selectively protonated samples.[105] In addition to improved spectral resolution, the structural information that can be obtained from ^{1}H distance constraints could prove to be invaluable for protein structure calculations. Given the currently limited options for rotor materials, the push towards higher MAS frequencies has been driven primarily by fabrication of rotors with increasingly smaller diameters. However, achieving hyper-fast spinning frequencies via fabrication of rotors where the rotor diameter is <0.5 mm becomes somewhat impractical due to the quadratic scaling between the inner diameter of the rotor and its sample volume. Instead, one must explore the use of stronger rotor materials as an alternative way to achieve these hyper-fast MAS frequencies.

Faster MAS not only improves spectral resolution, it can considerably boost the sensitivity of NMR experiments as well. The ability to perform ^{1}H-detected experiments offers potential gains in sensitivity of $(\gamma_H/\gamma_C)^{3/2} \cong 8$ compared to that of equivalent ^{13}C-detection methods. Building upon this, if ^{1}H-detection can be combined with dynamic nuclear polarization (DNP), the gain in sensitivity could be amplified by additional orders of magnitude.[57, 139] In order to optimally combine these two techniques, the material used for fabricating rotors would have to be both exceptionally strong as well as highly transparent to microwave irradiation. For these reasons we explored fabricating MAS rotors from single-crystal CVD diamond.

6.2.1 Rotor Material Comparison

CVD diamond offers significant advantages over traditional rotor materials.[140] First, diamond is one of the hardest materials in the world. The Young's modulus of CVD diamond is approximately five times greater than that of zirconia, which makes it significantly more durable with respect to plastic deformation.[141] This is a crucial property for MAS rotors due to the substantial mechanical stress they experience during MAS. CVD diamond is also one of the

world's best thermal conductors, with thermal conductivity approximately five times greater than copper and four hundred times greater than zirconia.[142] This makes CVD diamond an ideal choice for MAS NMR and DNP experiments, as cooling of the sample can be achieved more uniformly and efficiently with diamond compared to other rotor materials. Diamond's low coefficient of friction may also help to reduce sample heating during MAS. In contrast to zirconia, diamond also has very high transparency to THz radiation, making it an ideal candidate for DNP experiments.[143-145] Finally, the cost of CVD diamond stock material is surprisingly low. 1x1x5 mm diamond logs can be purchased from Element Six (Didcot, UK) for ~$50 which, assuming there is access to proper fabrication equipment, makes rotor fabrication very affordable.

6.2.2 Rotor Dynamics

Rotor dynamics is a branch of mechanical engineering concerning the behavior of rotating structures.[146, 147] As such, it is appropriate to utilize concepts from rotor dynamics to study the behavior of MAS rotors undergoing rotation. One of the most important factors to consider when designing MAS rotor systems is the rotor's critical speed. The critical speed is the angular frequency at which the natural frequency of the rotor is excited. As the rotor approaches its critical speed, it will reach a bending resonance condition and will fail. The natural frequency of a tube with rigid supports on each end is given by

$$f = \frac{\lambda^2}{2\pi L^2}\sqrt{\frac{EI}{A\rho}} \qquad \textbf{6.1}$$

where λ is the vibrational frequency factor (4.753 when vibration is first order), L is the rotor length, E is the young's modulus of the tube material, I is the moment of inertia, A is the cross-sectional area and ρ is the density of the tube material.[148] The cross-sectional area and moment of inertia for a hollow tube are given by

$$A = \frac{\pi}{4}(D^2 - d^2) \quad \textbf{6.2}$$

$$I = \frac{\pi}{64}(D^4 - d^4) \quad \textbf{6.3}$$

where D and d are the outer diameter and inner diameter of the tube, respectively.

For a rotor supported by air bearings, the critical speed of a rotor cannot be calculated purely off the above equations, as the air bearings are not rigid supports and therefore have a damping effect. A simplified model of a rotor system with two radial air bearings can be seen in Figure 6.1. While the air bearings help lower the frictional force on the rotor, they also lower the stiffness of the rotor system and consequently the critical speed of the rotor as well. An estimate of the average static bearing stiffness is given by

$$k = 2lr_b(p - p_{atm})/r_c \quad \textbf{6.4}$$

where k is the static bearing stiffness, l is the axial length of the bearing, r_b is the radius of the bearing, p is the manifold pressure, p_{atm} is the atmospheric pressure and r_c is the radial clearance between the rotor and bearing wall.[149] From this equation we can deduce that there is a tradeoff between the natural frequency of the rotor and the frictional force on the rotor. Increasing the bearing length, bearing manifold pressure, or decreasing the radial clearance will all result in a higher critical speed for the rotor but consequently will also increase the frictional force on the rotor. These are important factors to consider when designing MAS systems.

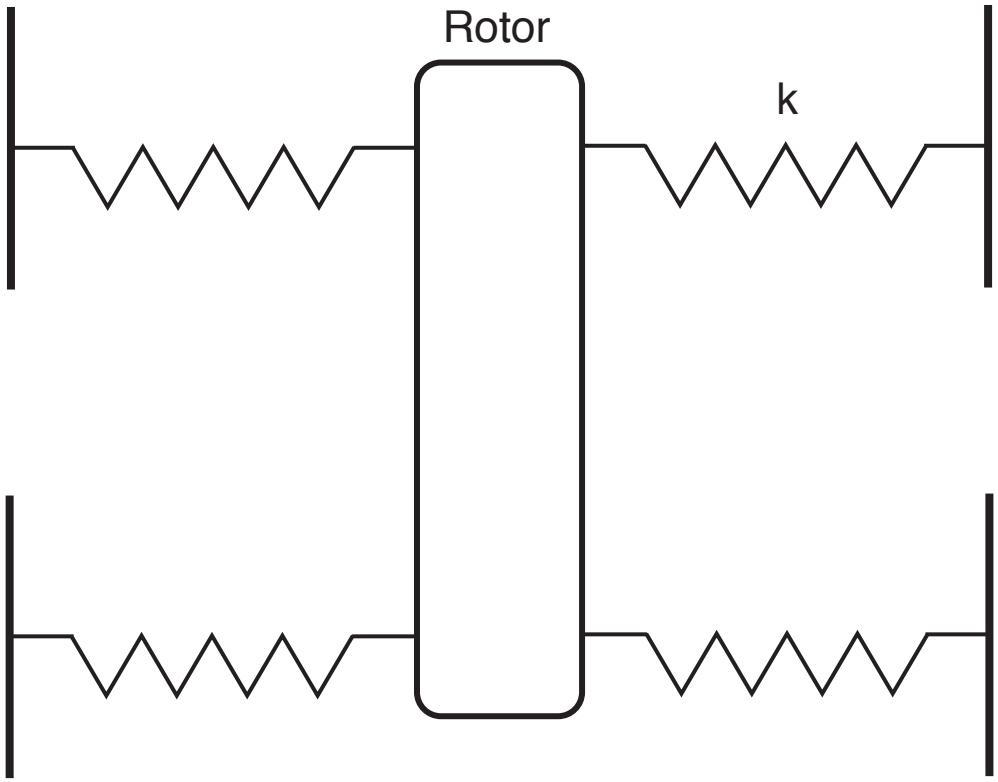

Figure 6.1: Cross-sectional schematic of a rotor supported by two radial air bearings. The air supplied by the radial air bearings helps to reduce friction and acts like a spring system to help keep the rotor spinning on-axis. The stiffness, k, of the air bearings plays a role in determining the critical speed of the rotor system.

For most applications, it is recommended that the maximum angular frequency of a rotor not exceed 70-75% of its critical speed. While it is possible to exceed a system's critical speed without damaging the machinery, to accomplish this the system must be rapidly swept through its natural frequency which for MAS rotors at high spinning frequencies is not practical. Figure 6.2 shows the undamped bending resonance zone for diamond and zirconia rotors. Given the number and complexity of the forces involved with MAS, accurately predicting the failure point of a rotor via theoretical calculations is difficult, however, the undamped critical speed of a rotor provides a good approximation of the best achievable spinning frequency for a given rotor material. Figure 6.2 clearly shows that diamond rotors have a significantly higher bending resonance condition than zirconia rotors, which is particularly crucial when using helium gas as the driving medium.

Therefore, fabricating rotors from diamond rather than zirconia should lead to a much higher regime of accessible spinning frequencies.

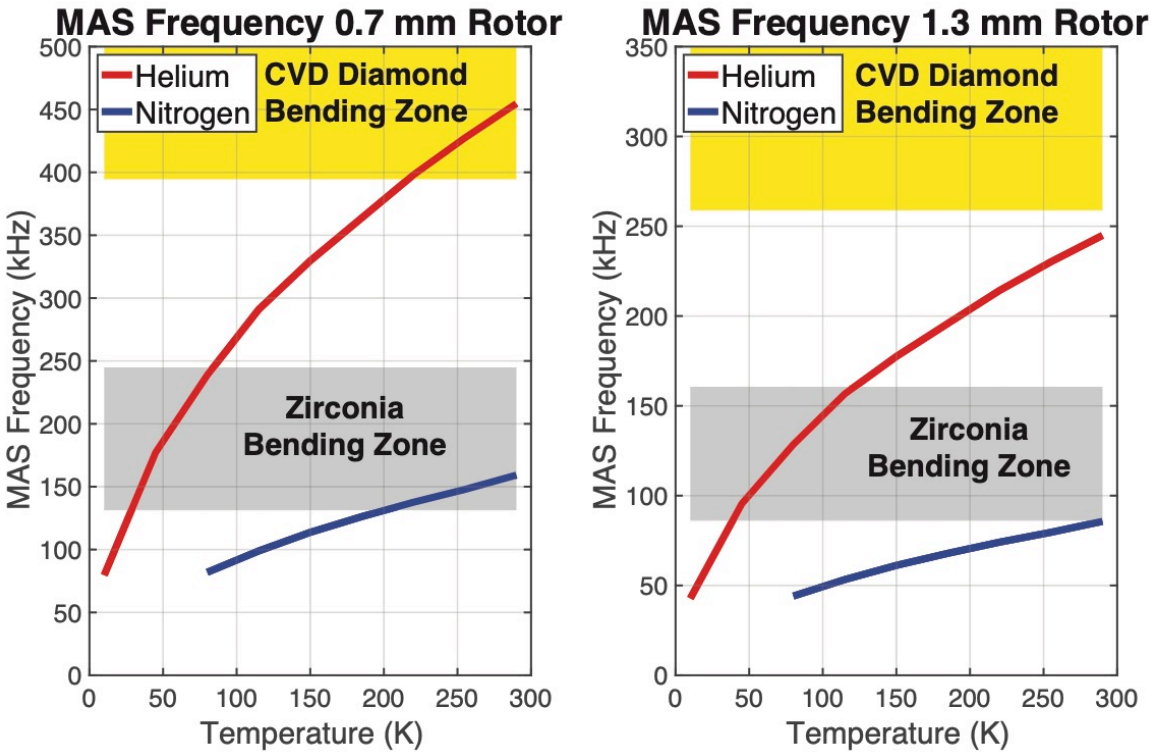

Figure 6.2: Diagram of bending resonance zones for 0.7 mm and 1.3 mm rotors. Critical speed bending zones represent 0.7-1.3x the undamped natural frequency of the rotor. Red and blue lines indicate the theoretical maximum achievable spinning frequency using helium and nitrogen as the driving gas assuming that the rotor is made of an indestructible material.

6.3 Fabrication Details

6.3.1 Characterization of CVD Diamond Optical Properties

Given diamond's extreme hardness, machining it using conventional tooling is incredibly difficult. One of the most common methods for machining diamond is using laser machining tools due to their ability to make precise cuts in hard materials. Nd:YAG lasers in particular are especially popular for cutting diamond.[150-152] In order to determine the optimal wavelength for cutting our CVD diamond logs, absorbance measurements were recorded on a sheet of single-crystal CVD diamond. Using these absorbance measurements, the penetration depth of light can

be calculated as a function of wavelength. The Beer-Lambert law describes the intensity of light in a given material as a function of depth which is given by the equation

$$I(z) = I_0 e^{-\alpha z} \tag{6.5}$$

where I is the light intensity, I_0 is the light intensity at the material's surface, α is the absorption coefficient and z is the depth. We can see that the intensity of light falls off exponentially with respect to depth. Consequently, the penetration depth of the laser light is given by

$$\delta_p = \frac{1}{\alpha} \tag{6.6}$$

where α is the absorption coefficient.

Figure 6.3 shows the absorbance and penetration depth of light in single-crystal CVD diamond as a function of wavelength. Nd:YAG lasers typically emit light at a wavelength of 1064 nm. This light can be efficiently frequency-doubled so that the laser can also operate at 532 nm. It can be seen in Figure 6.3 that both of these wavelengths are ideal for machining high aspect ratio features in diamond, as they offer a good compromise between laser absorbance and penetration depth. The 532 nm wavelength seems to be particularly ideal as it sits right on the edge of the absorbance spike. All absorbance measurements were recorded on an Agilent (Santa Clara, CA) Cary 5000 UV-Vis-NIR spectrophotometer.

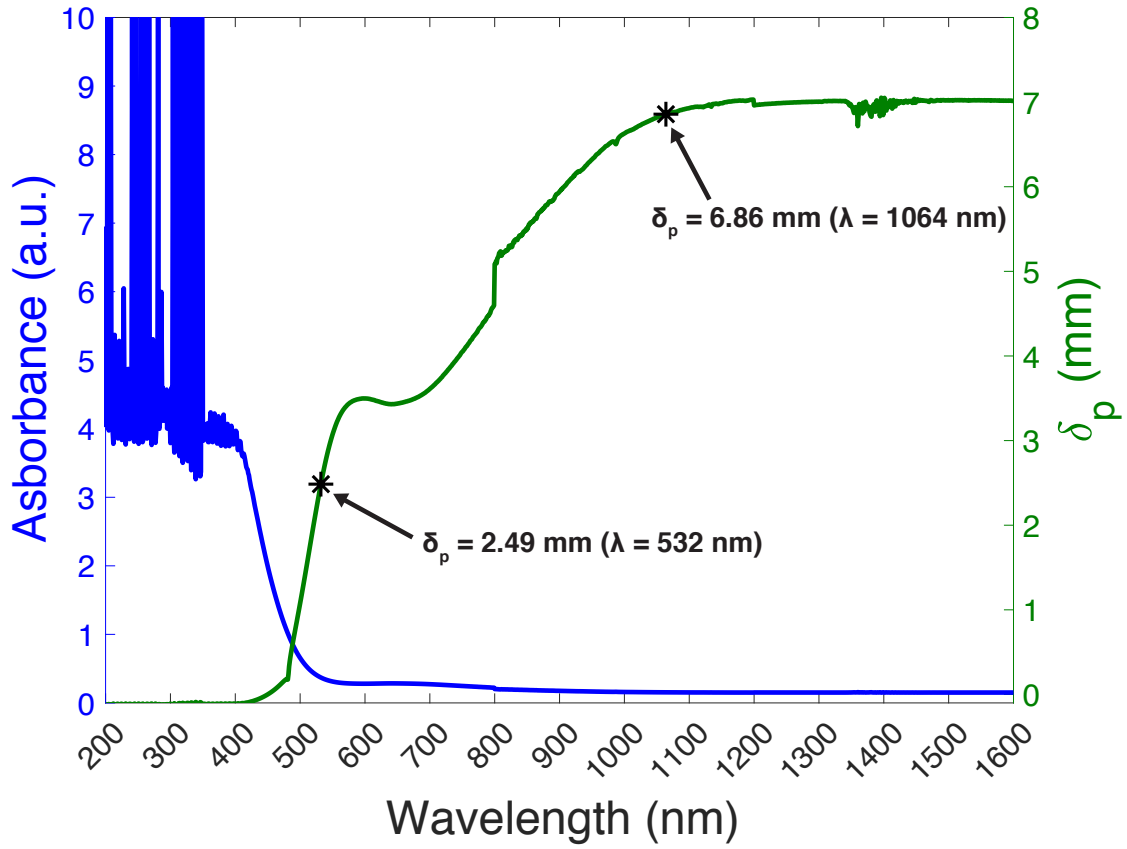

Figure 6.3: (Blue) Absorbance vs. wavelength for CVD diamond sheet. (Green) Penetration depth vs. wavelength for CVD diamond. The 532 nm light from a Nd:YAG laser offers a nice combination of absorbance and penetration depth.

6.3.2 Laser Machining Apparatus

All laser machining of CVD diamond took place on an A Series laser micromachining system from Oxford Lasers (Didcot, UK). The laser operates at a frequency-doubled wavelength of 532 nm and uses a Q-switch Nd:YAG solid state diode-pumped laser source. The laser produces a Gaussian beam which can be focused to a spot size of approximately 13 μm. For all laser machining fabrication an optical lens with a focal length of 100 mm was used. The laser cabinet features three independent linear actuators from Aerotech (Pittsburgh, US), that are capable of traveling distances of 200 mm, 200 mm, and 130 mm in the x, y, and z Cartesian directions,

respectively. Each of the Aerotech actuators have linear resolution of 0.25 μm and are accurate to within 2 μm.

To machine diamond rotors and drive caps, a custom machining apparatus was constructed within the Oxford laser system. The apparatus that was constructed is referred to as a "micro-lathe" and has both a "lathe" mode and "turntable" mode to machine the outer diameter and inner diameter of the rotor, respectively. Precise repositioning of the micro lathe setup when switching between modes is accomplished using a Thorlabs (Newton, NJ) KB3X3 kinematic base. The "micro-lathe" features a DDR100 rotary stage from Thorlabs capable of continuous 360° rotation at a maximum rate of 3 Hz. The DDR100 stage has a maximum axial wobble of 60 μrad and a maximum radial eccentricity of 6 μm. The rotary stage has a custom designed kinematic mount to adjust for tilt and yaw with respect to the stage's rotational axis. Additional tilt and yaw adjustment mounts were placed underneath the rotary stage to assist with squaring the diamond stock with respect to the laser beam. A custom clamp to mount the diamond stock to the rotary stage was fabricated via wire EDM using aluminum as the stock material. A diagram of the "micro-lathe" apparatus can be seen in Figure 6.4.

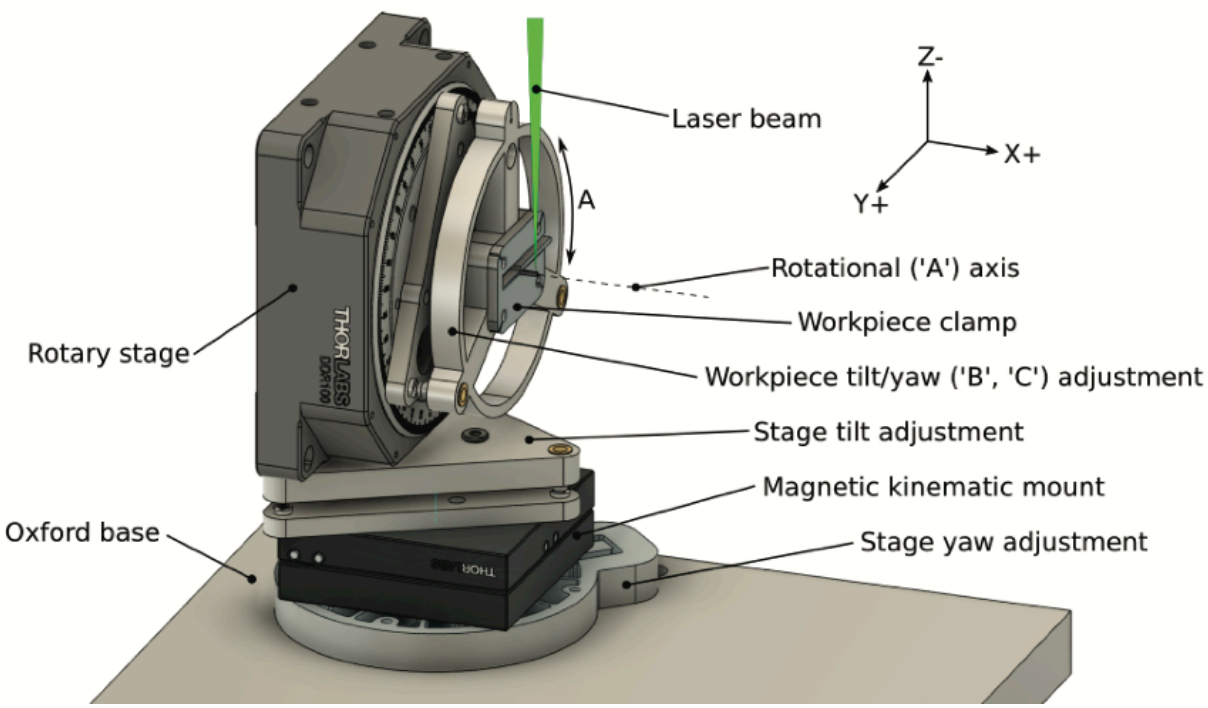

Figure 6.4: Diagram of Oxford "micro-lathe" apparatus. Figure courtesy of Zach Fredin.

Orthogonal alignment of the diamond stock with the laser beam is accomplished via an iterative process. Alignment measurements were performed using an OptoNCDT 2300-10 laser micrometer from Micro-Epsilon (Ortenburg, DE). The laser micrometer was attached to the frame of the Oxford system such that the micrometer laser faces the front surface of the rotary stage's kinematic mount. The front surface of the kinematic mount was lapped to ensure a smooth finish that would minimize surface roughness effects during displacement measurements. 3/16-100 TPI fine adjustment screws from Kozak Micro Adjusters (Randolph, NJ) were used to dial in the tilt, yaw, and runout of the rotary stage assembly. When properly optimized the "micro-lathe" apparatus was able to achieve a measured runout of <10 μm.

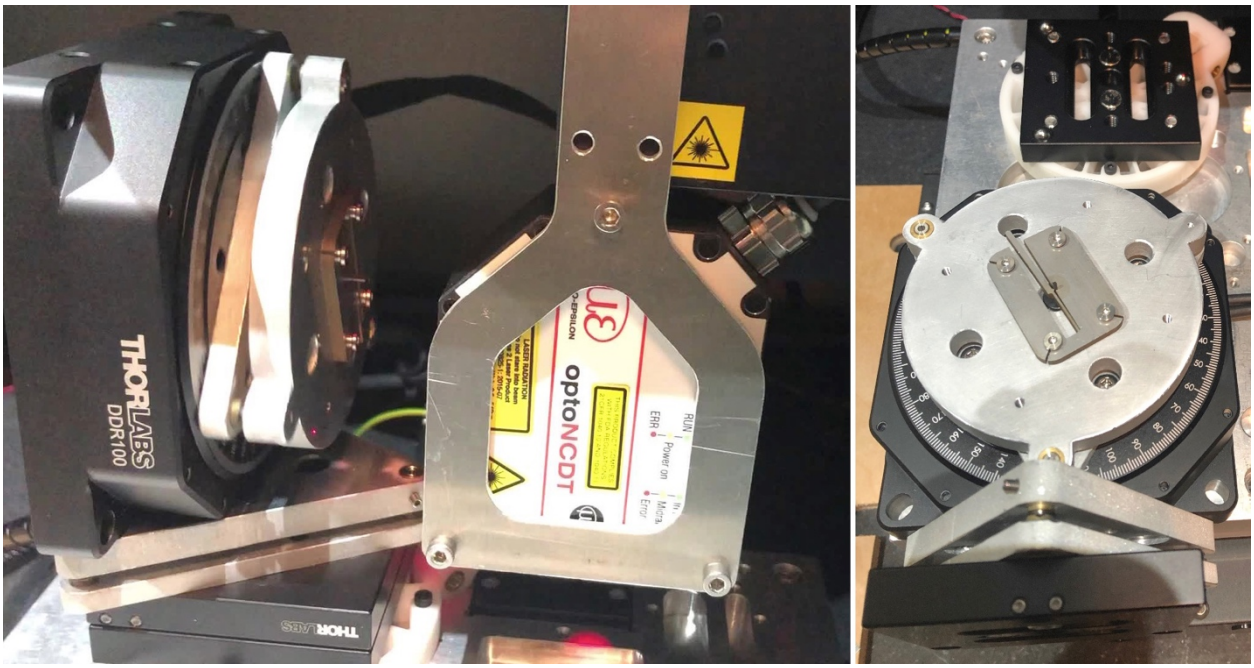

Figure 6.5: "Micro-lathe" assembly in Oxford laser cabinet. (Left) The apparatus is in "lathe" mode which is used to machine the outer diameter of the rotor. The Micro-Epsilon laser micrometer is used to dial in the tilt, yaw, and runout of the rotary stage. (Right) The apparatus is in "turntable" mode which is used to machine the inner diameter of the rotor. Switching between the two modes can be easily accomplished using the magnetic kinematic base.

6.3.3 Material Removal Mechanism

To our surprise, we were able to machine holes with remarkably high aspect ratios in the diamond logs. We believe that the mechanism for the high removal rate of diamond during the laser machining process can be attributed to a phase conversion from diamond to graphite, followed by oxidation of the graphite to CO, or CO_2. For an excellent review of the phase transitions that diamond undergoes under different oxidation conditions, we refer the reader to outside literature.[153] A brief summary of these transitions can be seen in Table 6.1. A more rigorous review of potential material removal mechanisms on a molecular level can be found in other literature.[154-157] The majority of these mechanisms involve the interaction of oxygen with the diamond surface, which causes a rearrangement of the carbon bonds along the surface and eventual removal of the carbon via oxidation to CO or CO_2. We believe that the oxygen present in ambient

air during laser machining plays a key role in material removal. Further studies involving graphite and CO_2 detection will be performed to confirm these mechanisms.

Table 6.1: Oxidation Conditions of Diamond.[153]

Temperature	Oxygen Surface Coverage	Phase Transition
700 °C – 1500 °C	0%	Phase transition from sp^3 to amorphous sp^2 carbon
>1600 °C	0%	Phase transition from sp^3 to crystalline graphite
>700 °C	<20%	Phase transition from sp^3 to amorphous sp^2 carbon followed by oxidation to gaseous CO/CO_2
>500 °C	>50%	Phase transition from sp^3 to amorphous sp^3 carbon followed by oxidation to gaseous CO/CO_2

6.3.4 Machining Toolpaths and Parameters

Early attempts at drilling holes in diamond did not involve a rotary stage. Instead, a spiral toolpath was used to drill pockets in the diamond logs. In this setup, the diamond log was mounted vertically in a vise, and a spiral pattern was traced out at different hole depths. The spiral toolpath helped create a pocket in the center of the hole that assisted in material removal. The first drilling tests were performed at high power (80-100% of maximum laser power), which led to bulging holes and occasional cracking of the diamond material. During initial tests, it was quickly realized that lower laser power (≤50% of maximum laser power) reduced and usually eliminated any potential bulging or cracking from overheating. The lowest pulse frequency of the Oxford laser system is 5 kHz, which was found to produce the lowest taper in the drilled holes. The feed rate

for the spiral pattern was typically 1 mm/s. All spiral toolpaths were designed using VCarve Pro by Vectric (Redditch, UK).

An important factor to consider when laser machining diamond is the power density of the laser pulse compared to the critical energy necessary to remove the diamond material. For a single laser pulse, the power density of the pulse is given by

$$P_L = \frac{4P_{avg}}{\pi t_0 f d_b^2} \quad \textbf{6.7}$$

where P_L is the power density of the laser, P_{avg} is the average power output of the laser, t_0 is the pulse width, f is the pulse frequency and d_b is the beam diameter at the focal point. Likewise, the critical energy needed to cause evaporation of the diamond is given by

$$P_C = \frac{k(T_e - T_0)}{2A}\sqrt{\frac{\pi}{\alpha t_0}} \quad \textbf{6.8}$$

where k is the thermal conductivity of diamond, T_e is the evaporation temperature, T_0 is room temperature, α is thermal diffusivity and A is the thermal absorption rate. These equations hold true for cases where there is no relative motion between the diamond stock and the laser, otherwise adjustments to the calculations must be made. For direct removal of diamond material via laser machining, P_L should be greater than P_C. However, for removal mechanisms involving a phase transition to graphite followed by oxidation to CO or CO_2, the calculations become more complicated. For a more in-depth analysis of this topic, the reader is referred to other literature.[158]

Spiral toolpaths generally lead to highly tapered, asymmetric holes during drilling. In an attempt to fix these issues, toolpaths utilizing the rotary stage were developed. All rotary stage toolpaths utilized the "micro-lathe" apparatus described in section 6.3.2 and were developed using custom Python scripts that output the machining toolpath in a G-code format that could be processed by the Oxford laser software. The parameters that could be changed via the Python

scripts included the laser power, x-axis feed rate, total distance traveled in x-axis, total depth of cut, depth of cut per pass, and repetitions per pass.

To machine the through hole of the rotor, the rotary stage was first mounted in "turntable" mode. The diamond log was rotated on the stage at a rotation rate of 1000 °/s, and the center of rotation of the log was found using the Oxford's viewing microscope. Using the log's center of rotation as the origin, a linear path for the laser was traced out using the desired radius of the through hole. Rotating the log during machining ensured that whatever hole was produced would be rotationally symmetric. Generally, both a coarse and finishing pass were used. It was found that the hole taper could be reduced significantly by ramping the laser power with respect to the depth of the hole on the coarse pass, as material removal was generally more difficult at deeper depths. A finishing pass was then used at 100% laser power to clean up the hole taper further. The finishing pass traced out a ring with inner diameter and outer diameter 60% and 100% of the diameter of the through hole, respectively. A summary of typical machining parameters for the rotor through hole is given in Table 6.2.

Table 6.2: Inner Diameter Machining Parameters using Rotary Stage Toolpaths

Step	Pulse Frequency (kHz)	Total Cut Depth (mm)	Linear Feed Rate (mm/s)	Depth Increments (mm)	Repetitions (Double Passes)	Laser Start Power	Laser End Power
Coarse Pass	5	6	0.050	0.050	10	20%	100%
Finishing Pass	5	6	0.050	0.015	40	100%	100%

After machining the inner diameter of the through hole, the rotary stage was returned to "lathe" mode to machine the outer diameter of the rotor. The diamond log was first manually rotated on the rotary stage to determine the trapezoidal log's maximum positions in the +y and -y

directions. This served as a guide to determine how many coarse passes were necessary to achieve dimensions close to the desired outer diameter. The coarse passes were intended to reduce machining time by quickly removing excess bulk material. After the coarse passes, an estimate of the outer diameter of the diamond tube was determined via the Oxford's viewing microscope. Finishing passes were then used to achieve the desired outer diameter of the rotor as well as the desired surface finish. After each finishing pass the outer diameter of the diamond rotor was measured via the Oxford's viewing microscope, and the next pass was adjusted accordingly to dial in the correct dimensions.

A summary of typical parameters used for machining the outer diameter of the rotor is provided in Table 6.3. After machining the outer diameter of the rotor, the top of the rotor was faced to produce a flat surface. The rotor was then cut from the stock material. For the facing and removal operations, the same feed rate and laser power as the finishing pass were used. Generally, the 5 mm long diamond logs did not have enough length to machine the entire length of the 4.6 mm long rotor. In the future, adjustments will need to be made to the mounting clamp that allow it to grip the diamond with less stock, or alternatively, longer diamond logs will need to be used.

Table 6.3: Outer Diameter Machining Parameters using Rotary Stage Toolpaths

Step	Pulse Frequency (kHz)	Total Cut Length (mm)	Linear Feed Rate (mm/s)	Depth Increments (mm)	Repetitions (Double Passes)	Laser Power
Coarse Pass	5	3.8	0.010	0.050	1	50%
Finishing Pass	5	3.8	0.002	0.005	1	50%

6.3.5 Removal of Amorphous Carbon Layer

The laser machining process leaves behind a thin layer of amorphous carbon on the surface of the CVD diamond. The amorphous carbon layer on the diamond surface presents a difficult problem for NMR and DNP experiments, as the presence of a conductor on the surface of the rotor could have a substantial effect on the probe's RF tuning as well as the microwave transparency of the rotor. The microwave transparency of the rotor is particularly concerning, as the skin depth in the THz regime is orders of magnitude smaller than at RF frequencies. Many different methods were used in initial attempts to remove the amorphous carbon from the diamond surface including piranha etching, oxygen plasma cleaning, and microwave acid digestion. All of these methods proved to be unsuccessful.

To remove the amorphous carbon from the diamond surface, the laser machined CVD diamond was baked in a furnace at 600 °C. The gas inside the furnace was ambient air at atmospheric pressure. In the presence of air, amorphous carbon should oxidize at temperatures of approximately 375-450 °C.[159] The rate of removal can be increased at temperatures above 450 °C, however, care must be taken not to exceed 700 °C, as above this temperature the diamond can begin to oxidize and burn away. The best results for the amorphous carbon removal were achieved by leaving the diamond in the furnace overnight. An image of a partially machined diamond rod can be seen in Figure 6.6 both before and after baking.

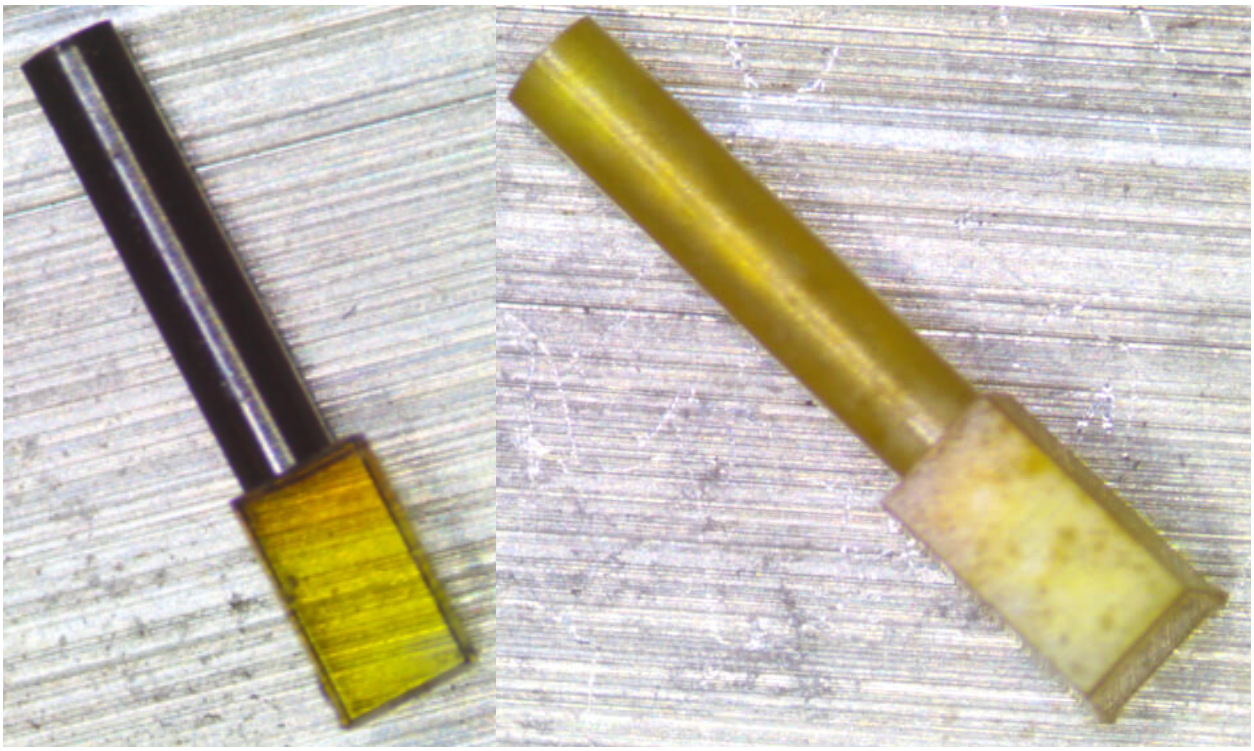

Figure 6.6: (Left) Partially machined diamond rod. (Right) Partially machined diamond rod after baking in furnace at 600 °C.

6.3.6 Fabrication Progress

The first attempts at machining diamond rotors produced rough, highly tapered through holes. Based on exit hole observations, the through holes being machined were highly asymmetrical, which would have inevitably led to substantial rotor imbalances during MAS. The taper angle of the holes also prevented drive and end caps from being properly inserted into the rotor, even with the aid of adhesives. Subsequent iterations and adjustments have greatly improved the quality of the rotors that have been fabricated. The outer diameter of the rotor can be machined to within ~5 μm of the target diameter. Using improved toolpaths with the rotary stage, the taper angle of the through hole has been reduced to <0.3° and a taper of <1%. This corresponds to a difference in the diameter of the entrance and exit holes of less than 50 μm. For comparison, using an optical lens with a 100 mm focal length, the taper angle of the Gaussian laser beam is ~3°. These results suggest that it is possible to machine a through hole with <10% of the taper of the

laser beam itself. As the machining apparatus continues to be improved, we hope to achieve a taper angle of <0.05°, which should be sufficient for fabricating well-balanced MAS rotors. A collage of our current machining progress can be seen in Figure 6.7.

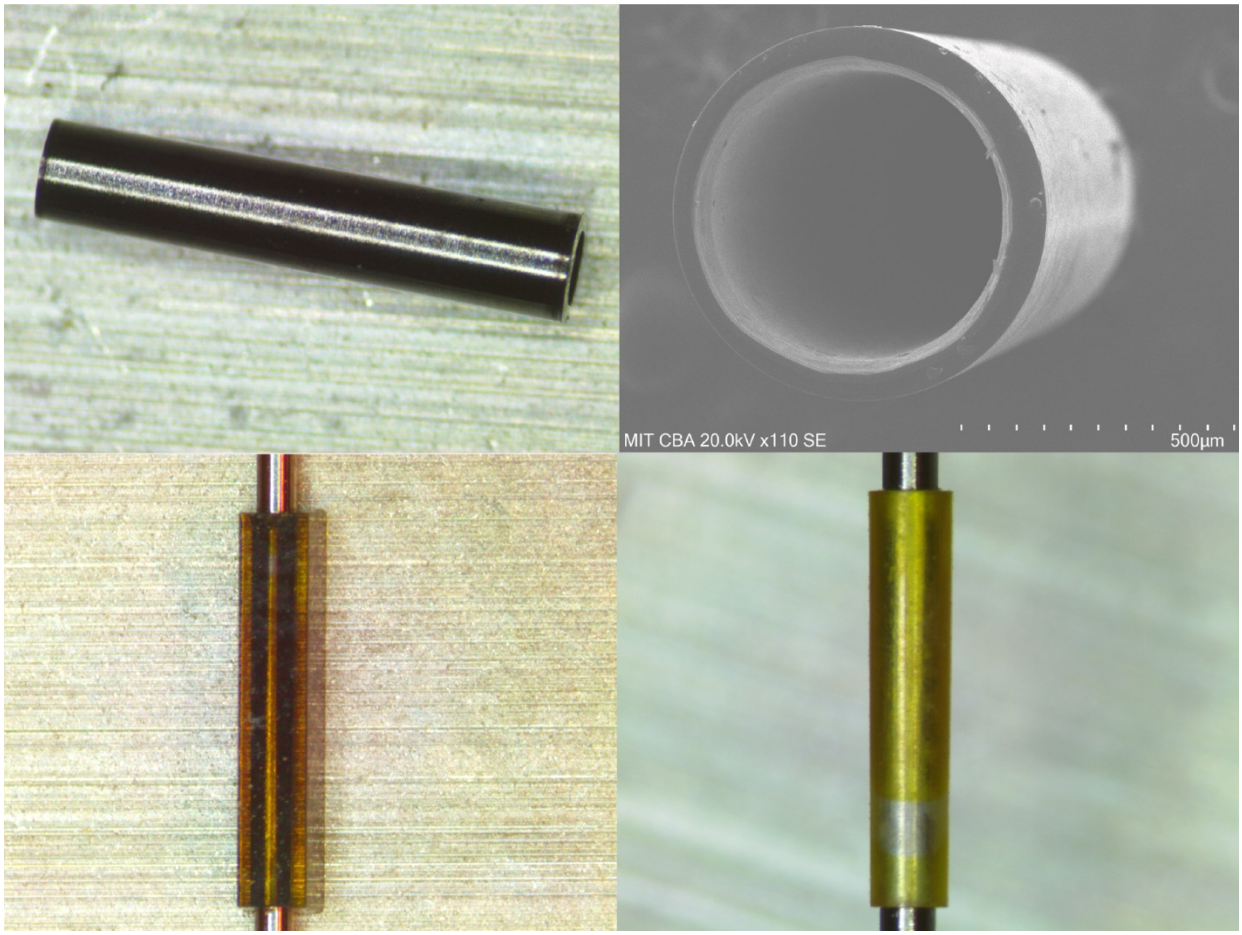

Figure 6.7: Collage of current diamond rotor machining progress. (Top left) Fully machined diamond rotor prior to being baked in a furnace. (Top right) SEM image of diamond rotor. (Bottom left) Diamond log with machined through hole. A 0.49 mm gauge pin has been placed through the hole. (Bottom right) Fully machined diamond rotor after being baked in a furnace. A 0.49 mm gauge pin has been placed through the rotor.

In addition to laser machining diamond rotors, significant progress has been made machining drive caps from CVD diamond as well. CVD diamond drive caps offer several advantages over their plastic counterparts such as improved rigidity of the turbine as well as improved microwave transparency for potential axial microwave coupling experiments. Diamond turbines that qualitatively resemble their plastic counterparts have been achieved, but a primary

issue that remains when laser machining drive caps for MAS rotors is the lack of depth control during the machining process. This creates difficulty in machining turbines with a flat section on the bottom that can seal the rotor. However, as the machining apparatus and parameters continue to improve, the potential to machine CVD diamond drive caps remains highly feasible based on current progress. A comparison between a laser machined diamond drive cap and a plastic drive cap can be seen in Figure 6.8.

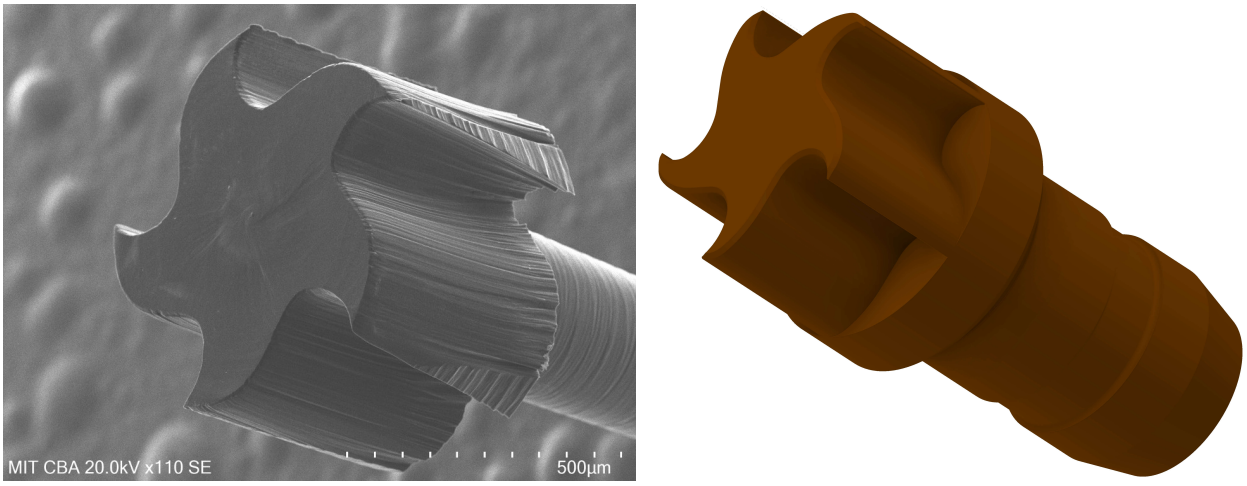

Figure 6.8: Drive tip machining progress. (Left) 0.7 mm CVD diamond drive tip fabricated via laser machining. (Right) CAD drawing of 0.7 mm Vespel drive tip for comparison.

6.3.7 Spin Testing

Prior to running MAS experiments, the diamond rotors must be thoroughly tested in order to ensure that the potential for a rotor crash is minimized. To test the viability of spinning laser machined MAS rotor components, a spin test was performed with a 1.3 mm diamond end cap. The diamond end cap was machined from a 1.5x1.5x5 mm CVD diamond log from Element Six. The end cap was epoxied into the end of a 1.3 mm zirconia rotor and spin tested at an unregulated spinning frequency of 30 kHz. To our knowledge this was the world's first spin test of a MAS rotor component made from CVD diamond. Despite not achieving the desired dimensional tolerances on the end cap, the rotor was able to spin at a MAS frequency of 30 kHz without

crashing. Upon trying to spin up to 35 kHz, the rotor ejected from the stator, however, this preliminary test is extremely encouraging, as it demonstrates that it is feasible to spin diamond rotor components to high spinning frequencies if the dimensions of the components are reasonably close to the necessary specifications. A summary of the spin test results can be seen in Figure 6.9.

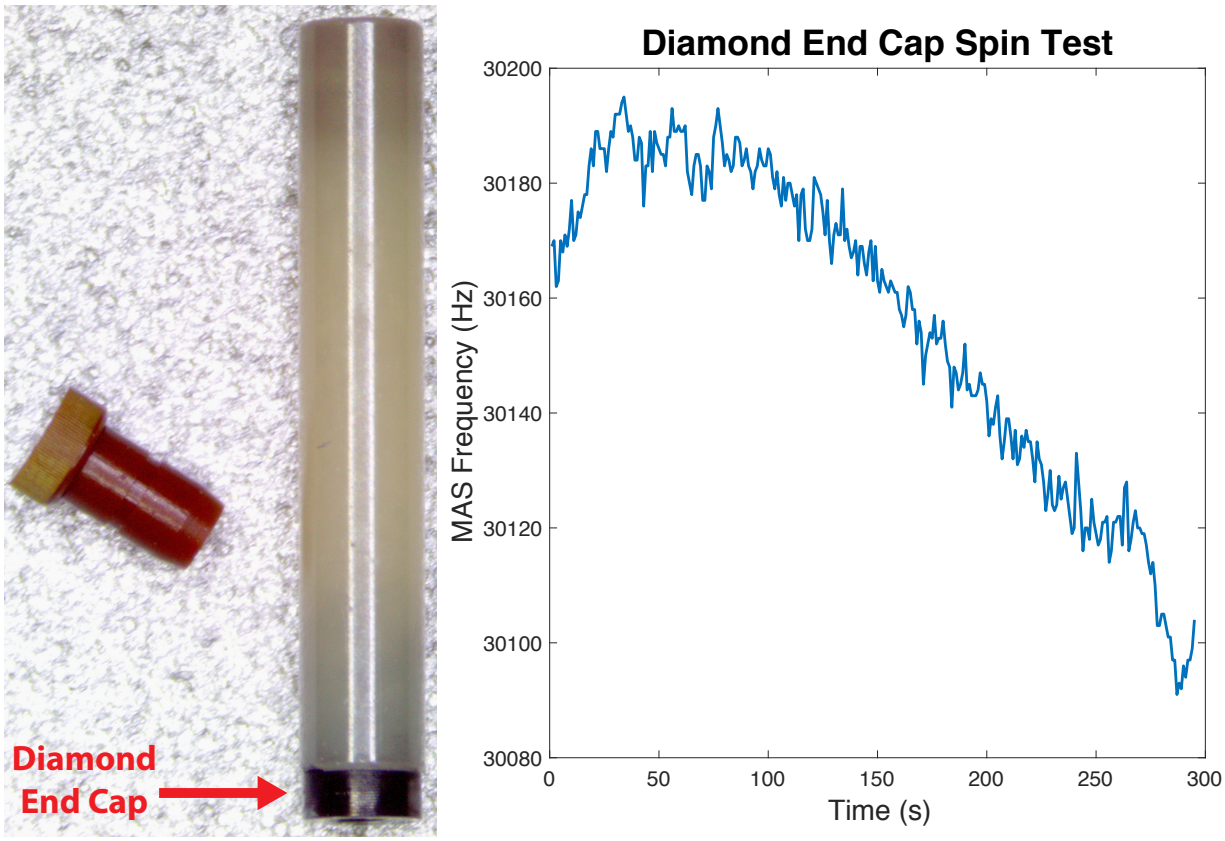

Figure 6.9: (Left) Diamond end cap in 1.3 mm rotor. (Right) Spin test results for 1.3 mm rotor with diamond end cap.

Given the encouraging results of the 1.3 mm diamond end cap, additional spin testing was performed using a 0.7 mm CVD diamond rotor. This rotor was machined from custom 1x1x5.5 mm long CVD diamond logs to provide enough length to machine the entire 4.6 mm length of the rotor. Due to the presence of a ~40 μm taper in the diamond rotor, the Vespel drive cap and end cap were epoxied into the ends of the rotor. The rotor was spin tested in the 0.7 mm Bruker test stand seen in Section 6.6. Surprisingly, despite the significant taper in the rotor, it was able to spin up to a MAS frequency of 7 kHz. While the rotor was unable to meet our ultimate target of >100

kHz, this was a monumental first test, marking the first time a diamond MAS rotor has ever been spun and further demonstrating that with proper tolerances, diamond rotors are feasible for performing MAS experiments. A spin plot of the 0.7 mm diamond rotor spin test is seen in Figure 6.10.

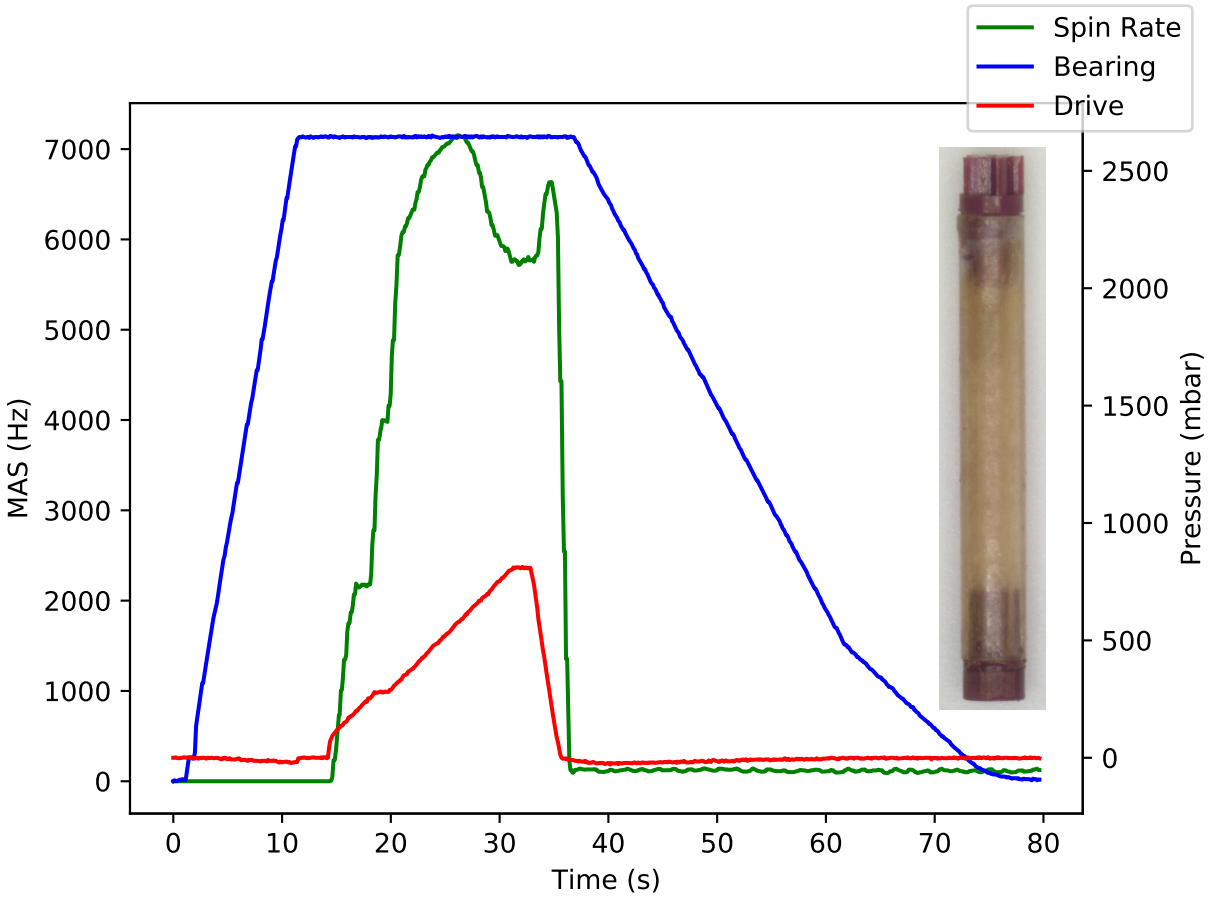

Figure 6.10: MAS plot of 0.7 mm diamond rotor test. A maximum MAS frequency of ~7 kHz was reached. A picture of the diamond rotor can be seen on the right side of the graph. Figure courtesy of Brian Michael, Salima Bahri, and Zach Fredin.

6.4 Future Work

The top priority proof-of-concept test for the MAS diamond rotors is to successfully spin a fully machined diamond rotor at high frequencies. However, there are many additional aspects of the diamond laser machining process that would benefit from further characterization. First, it would be of great interest to further characterize the material removal mechanism, including

describing the components of the amorphous carbon layer and detecting the release of CO or CO_2 during the machining process. Determining the effect that different atmospheres have on the material removal rate would also be beneficial.[160] For example, tests could be performed to determine the effects of varying concentrations of atmospheric oxygen on the material removal rate. Raising the temperature may also increase the material removal rate and reduce the through hole taper by lowering the energy barrier necessary to remove the carbon material. For these tests, a miniature furnace was designed which can be seen in Figure 6.11. This furnace can be constructed in the future and used as a characterization tool to further study the mechanisms behind the carbon material removal.

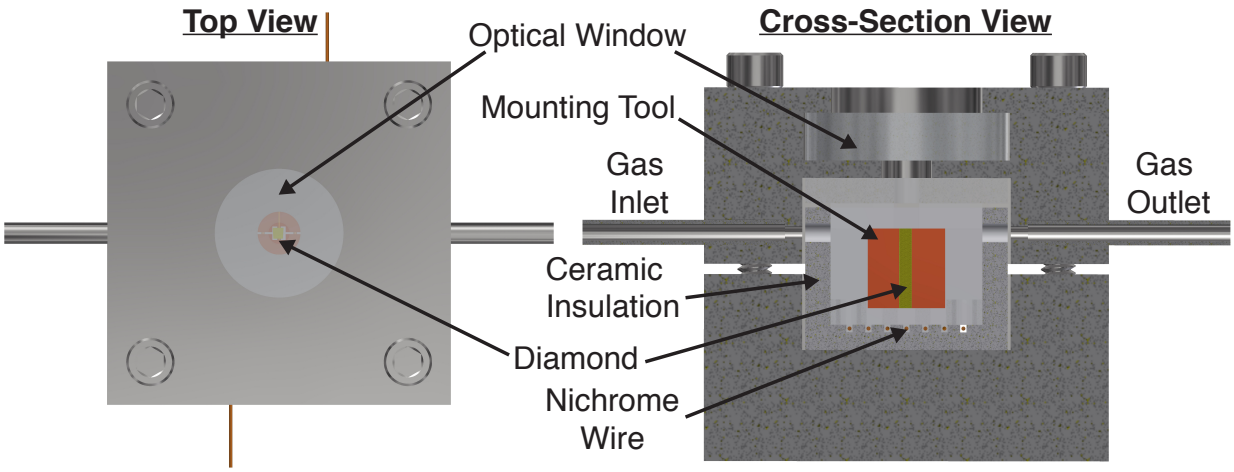

Figure 6.11: Miniature furnace for heat and atmospheric testing during diamond laser machining.

Ultimately, the success of fabricating diamond rotors is dependent on reducing the taper of the through hole. For optimal spinning, the inner diameter of the rotor must be uniform and circular throughout. There are a few different methods by which the taper could be improved. One option is to construct a laser apparatus that is capable of angling the laser beam in a way similar to that of a galvanometer scanner. In previous literature, inclination of the beam angle has shown to significantly reduce the taper of laser machined holes and can even create reverse tapers if done properly.[161] An example of this can be seen in Figure 6.12.

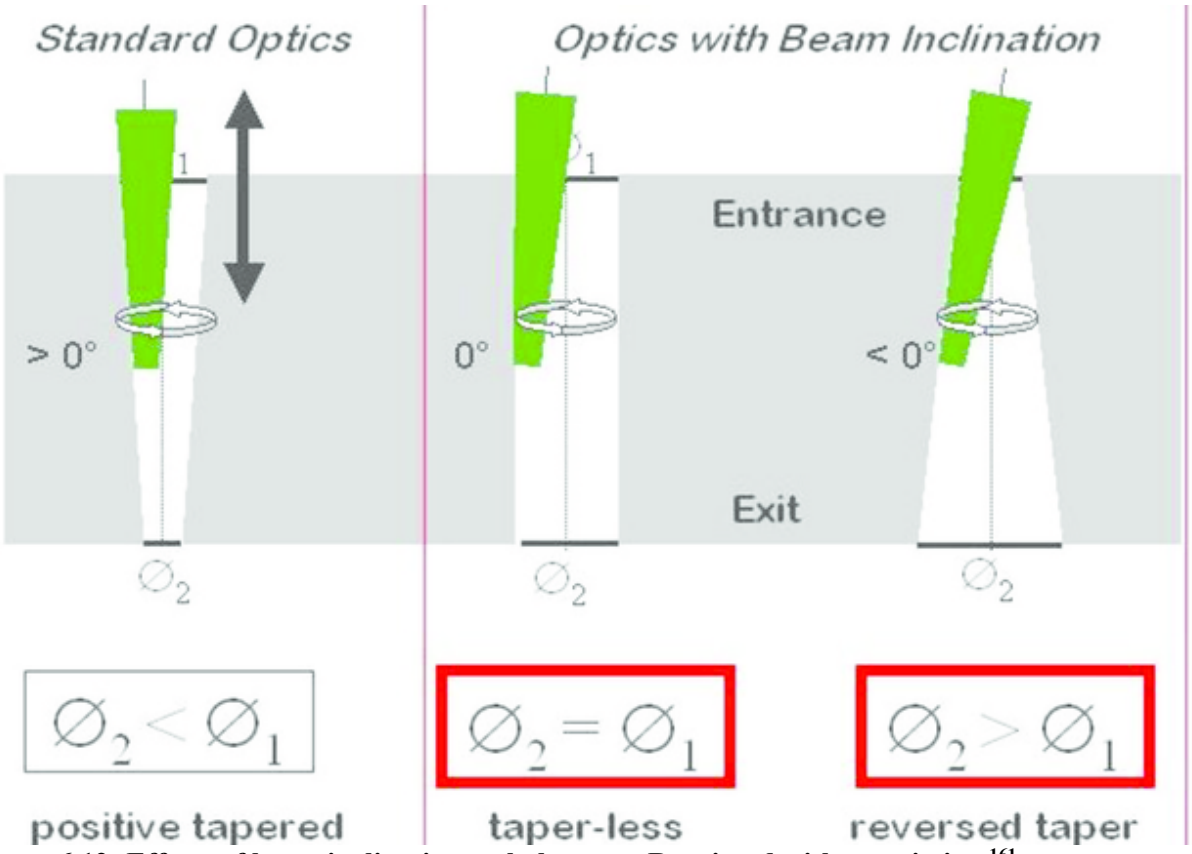

Figure 6.12: Effects of beam inclination on hole taper. Reprinted with permission.[161]

Another option for reducing the taper of the through hole is to machine the diamond rotor from both ends. This can be accomplished by constructing a laser apparatus with multiple beam paths or by flipping the log between operations. The latter option requires a way to accurately reposition the laser beam at the center of the log's rotation axis. Assuming minimum perturbation (a few microns) occurs during the process of flipping the log, one way to accurately relocate the center of the log is to use a reference marker. The reference marker may consist of a removable target which can be laser marked with a microscopic hole prior to flipping the mount. If the offset from the center of the log and the mark is known, a viewing microscope can be used to find the center of the mark, and the offset can be used to reset the position of the laser to the center of the log. Either method would hopefully reduce the taper of the though hole sufficiently so that the

drive and end caps could be properly mounted in the diamond rotors and the assembly then used for MAS NMR experiments.

6.5 Chapter-Specific Acknowledgements

This work would not have been possible without the contributions from many wonderful colleagues and collaborators. First, I would like to thank our collaborators at Bruker Biospin for providing us with equipment for spin testing diamond rotors as well as for helpful discussions regarding rotor dimensions and specifications. I'd like to say thank you to Nicole Moody for her help with acquiring the optical absorption data of the CVD diamond sheet and initial characterization of the optical properties of the diamond. Zach Fredin had numerous, substantial contributions to this work, including designing and fabricating the "micro-lathe" apparatus, optimizing machining parameters, as well as many helpful discussions regarding laser machining approaches. Prashant Patil was instrumental in obtaining early laser machining results as well as optimizing machining parameters to achieve high-aspect ratio features. Salima Bahri significantly contributed towards the optimization of diamond machining parameters. Camron Blackburn performed diamond machining characterization at different wavelengths on a PHAROS femtosecond laser and wrote the initial Python toolpaths for laser machining. Will Langford provided significant early support with constructing a suitable machining apparatus for diamond machining, including initial setup of the Thorlabs rotary stage and fabrication of pitch and yaw adjustment mechanisms. Finally, we owe a huge thank you to Neil Gershenfeld, director of MIT's Center for Bits and Atoms, for providing us with access to all of his fabrication equipment and for incredibly helpful discussions regarding methods for improving our machining procedures.

6.6 Supporting Information

For the purpose of spin testing 0.7 mm and 1.3 mm diamond rotors, a spinning test stand was generously supplied by Bruker Biospin (Billerica, MA). Pictures of the test stand can be seen in Figure 6.13. The test stand features swappable stator modules for testing 0.7 mm and 1.3 mm rotors. The test stand stators lack an RF coil and are manufactured from stainless steel to improve the durability of the stator system during destructive testing.

Figure 6.13: Bruker test stand equipped with 0.7 mm stator. The test stand can be used for destructive testing of diamond rotors.

7 References

1. Rabi, I. I.; Zacharias, J. R.; Millman, S.; Kusch, P., A New Method of Measuring Nuclear Magnetic Moment. *Physical Review* **1938,** *53* (4), 318-318.
2. Gerlach, W.; Stern, O., Der experimentelle Nachweis der Richtungsquantelung im Magnetfeld. *Zeitschrift für Physik* **1922,** *9* (1), 349-352.
3. Rabi, I. I.; Millman, S.; Kusch, P.; Zacharias, J. R., The Magnetic Moments of $_3Li^6$, $_3Li^7$ and $_9F^{19}$. *Physical Review* **1938,** *53* (6), 495-495.
4. Rabi, I. I.; Millman, S.; Kusch, P.; Zacharias, J. R., The Molecular Beam Resonance Method for Measuring Nuclear Magnetic Moments. The Magnetic Moments of $_3Li^6$, $_3Li^7$ and $_9F^{19}$. *Physical Review* **1939,** *55* (6), 526-535.
5. Bloch, F.; Hansen, W. W.; Packard, M., The Nuclear Induction Experiment. *Physical Review* **1946,** *70* (7-8), 474-485.
6. Purcell, E. M.; Torrey, H. C.; Pound, R. V., Resonance Absorption by Nuclear Magnetic Moments in a Solid. *Physical Review* **1946,** *69* (1-2), 37-38.
7. Hahn, E. L., Nuclear Induction Due to Free Larmor Precession. *Physical Review* **1950,** *77* (2), 297-298.
8. Hahn, E. L., Spin Echoes. *Physical Review* **1950,** *80* (4), 580-594.
9. Ernst, R. R.; Anderson, W. A., Application of Fourier Transform Spectroscopy to Magnetic Resonance. *Rev. Sci. Instrum.* **1966,** *37* (1), 93-102.
10. Haeberlen, U.; Waugh, J. S., Coherent Averaging Effects in Magnetic Resonance. *Physical Review* **1968,** *175* (2), 453-467.
11. Waugh, J. S.; Huber, L. M.; Haeberlen, U., Approach to High-Resolution nmr in Solids. *Physical Review Letters* **1968,** *20* (5), 180-182.
12. Gullion, T.; Schaefer, J., Rotational-echo double-resonance NMR. *Journal of Magnetic Resonance (1969)* **1989,** *81* (1), 196-200.
13. Mansfield, P., Symmetrized pulse sequences in high resolution NMR in solids. *Journal of Physics C: Solid State Physics* **1971,** *4* (11), 1444-1452.
14. Bennett, A. E.; Rienstra, C. M.; Auger, M.; Lakshmi, K. V.; Griffin, R. G., Heteronuclear decoupling in rotating solids. *The Journal of Chemical Physics* **1995,** *103* (16), 6951-6958.
15. Levitt, M. H., Symmetry in the design of NMR multiple-pulse sequences. *The Journal of Chemical Physics* **2008,** *128* (5), 052205.
16. Bennett, A. E.; Griffin, R. G.; Vega, S., Recoupling of Homo- and Heteronuclear Dipolar Interactions in Rotating Solids. In *Solid-State NMR IV Methods and Applications of Solid-State NMR*, Blümich, B., Ed. Springer Berlin Heidelberg: Berlin, Heidelberg, 1994; pp 1-77.
17. Pines, A.; Gibby, M. G.; Waugh, J. S., Proton-Enhanced Nuclear Induction Spectroscopy. A Method for High Resolution NMR of Dilute Spins in Solids. *The Journal of Chemical Physics* **1972,** *56* (4), 1776-1777.
18. Levitt, M. H., *Spin Dynamics: Basics of Nuclear Magnetic Resonance*. 2nd ed ed.; John Wiley & Sons: Chichester, England ; Hoboken, NJ, 2008; p 714.
19. Keeler, J., *Understanding NMR Spectroscopy*. 2nd ed ed.; John Wiley and Sons: Chichester, U.K, 2010; p 511.
20. Duer, M. J., *Solid-state NMR spectroscopy: Principles and Applications*. Blackwell Science: Malden, MA, 2002; p 567.

21. Medek, A.; Harwood, J. S.; Frydman, L., Multiple-Quantum Magic-Angle Spinning NMR: A New Method for the Study of Quadrupolar Nuclei in Solids. *Journal of the American Chemical Society* **1995,** *117* (51), 12779-12787.
22. Keeler, E. G.; Michaelis, V. K.; Wilson, C. B.; Hung, I.; Wang, X.; Gan, Z.; Griffin, R. G., High-Resolution 17O NMR Spectroscopy of Structural Water. *The Journal of Physical Chemistry B* **2019,** *123* (14), 3061-3067.
23. Gan, Z., Isotropic NMR Spectra of Half-Integer Quadrupolar Nuclei Using Satellite Transitions and Magic-Angle Spinning. *Journal of the American Chemical Society* **2000,** *122* (13), 3242-3243.
24. Trebosc, J.; Amoureux, J.-P.; Gan, Z., Comparison of high-resolution solid-state NMR MQMAS and STMAS methods for half-integer quadrupolar nuclei. *Solid State Nuclear Magnetic Resonance* **2007,** *31* (1), 1-9.
25. Overhauser, A. W., Polarization of Nuclei in Metals. *Physical Review* **1953,** *92* (2), 411-415.
26. Carver, T. R.; Slichter, C. P., Polarization of Nuclear Spins in Metals. *Physical Review* **1953,** *92* (1), 212-213.
27. Carver, T. R.; Slichter, C. P., Experimental Verification of the Overhauser Nuclear Polarization Effect. *Physical Review* **1956,** *102* (4), 975-980.
28. Abragam, A., Overhauser Effect in Nonmetals. *Physical Review* **1955,** *98* (6), 1729-1735.
29. Jeffries, C. D., Polarization of Nuclei by Resonance Saturation in Paramagnetic Crystals. *Physical Review* **1957,** *106* (1), 164-165.
30. Jeffries, C. D., Dynamic Orientation of Nuclei by Forbidden Transitions in Paramagnetic Resonance. *Physical Review* **1960,** *117* (4), 1056-1069.
31. Corzilius, B.; Smith, A. A.; Griffin, R. G., Solid effect in magic angle spinning dynamic nuclear polarization. *The Journal of Chemical Physics* **2012,** *137* (5), 054201.
32. Kessenikh, A. V.; Lushchikov, V. I.; Manenkov, A. A.; Taran, Y. V., Proton Polarization in Irradiated Polyethylenes. *Soviet Physics Solid State* **1963,** *5*, 321.
33. Hwang, C. F.; Hill, D. A., New Effect in Dynamic Polarization. *Physical Review Letters* **1967,** *18* (4), 110-112.
34. Lilly Thankamony, A. S.; Wittmann, J. J.; Kaushik, M.; Corzilius, B., Dynamic nuclear polarization for sensitivity enhancement in modern solid-state NMR. *Progress in Nuclear Magnetic Resonance Spectroscopy* **2017,** *102-103*, 120-195.
35. Equbal, A.; Leavesley, A.; Jain, S. K.; Han, S., Cross-Effect Dynamic Nuclear Polarization Explained: Polarization, Depolarization, and Oversaturation. *The Journal of Physical Chemistry Letters* **2019,** *10* (3), 548-558.
36. Can, T. V.; Caporini, M. A.; Mentink-Vigier, F.; Corzilius, B.; Walish, J. J.; Rosay, M.; Maas, W. E.; Baldus, M.; Vega, S.; Swager, T. M.; Griffin, R. G., Overhauser effects in insulating solids. *The Journal of Chemical Physics* **2014,** *141* (6), 064202.
37. Changsik, S.; Kan-Nian, H.; Chan-Gyu, J.; Swager, T. M.; Griffin, R. G. r. m. e., TOTAPOL: A Biradical Polarizing Agent for Dynamic Nuclear Polarization Experiments in Aqueous Media. *Journal of the American Chemical Society* **2006,** *128* (35), 11385-11390.
38. Sauvée, C.; Rosay, M.; Casano, G.; Aussenac, F.; Weber, R. T.; Ouari, O.; Tordo, P., Highly Efficient, Water-Soluble Polarizing Agents for Dynamic Nuclear Polarization at High Frequency. *Angewandte Chemie International Edition* **2013,** *52* (41), 10858-10861.

39. Ni, Q. Z.; Daviso, E.; Can, T. V.; Markhasin, E.; Jawla, S. K.; Swager, T. M.; Temkin, R. J.; Herzfeld, J.; Griffin, R. G., High Frequency Dynamic Nuclear Polarization. *Accounts of Chemical Research* **2013,** *46* (9), 1933-1941.
40. Granatstein, V. L.; Parker, R. K.; Armstrong, C. M., Vacuum electronics at the dawn of the twenty-first century. *Proceedings of the IEEE* **1999,** *87* (5), 702-716.
41. Becerra, L. R.; Gerfen, G. J.; Temkin, R. J.; Singel, D. J.; Griffin, R. G., Dynamic nuclear polarization with a cyclotron resonance maser at 5 T. *Physical Review Letters* **1993,** *71* (21), 3561-3564.
42. Blank, M.; Borchard, P.; Cauffman, S.; Felch, K. In *Demonstration of a 593 GHz Gyrotron for DNP*, 2018 43rd International Conference on Infrared, Millimeter, and Terahertz Waves (IRMMW-THz), 9-14 Sept. 2018; 2018; pp 1-2.
43. Booske, J. H.; Dobbs, R. J.; Joye, C. D.; Kory, C. L.; Neil, G. R.; Park, G.; Park, J.; Temkin, R. J., Vacuum Electronic High Power Terahertz Sources. *IEEE Transactions on Terahertz Science and Technology* **2011,** *1* (1), 54-75.
44. Rosay, M.; Scrgeyev, I.; Tometich, L.; Hickey, C.; Roitman, A.; Yake, D.; Berry, D. In *Opportunities and Challenges for EIK's in DNP NMR Applications*, 2018 43rd International Conference on Infrared, Millimeter, and Terahertz Waves (IRMMW-THz), 9-14 Sept. 2018; 2018; pp 1-2.
45. Sergeyev, I. V.; Aussenac, F.; Purea, A.; Reiter, C.; Bryerton, E.; Retzloff, S.; Hesler, J.; Tometich, L.; Rosay, M., Efficient 263 GHz magic angle spinning DNP at 100 K using solid-state diode sources. *Solid State Nuclear Magnetic Resonance* **2019,** *100*, 63-69.
46. Kowalski, E. J.; Tax, D. S.; Shapiro, M. A.; Sirigiri, J. R.; Temkin, R. J.; Bigelow, T. S.; Rasmussen, D. A., Linearly Polarized Modes of a Corrugated Metallic Waveguide. *IEEE Transactions on Microwave Theory and Techniques* **2010,** *58* (11), 2772-2780.
47. Nanni, E. A.; Jawla, S. K.; Shapiro, M. A.; Woskov, P. P.; Temkin, R. J., Low-loss Transmission Lines for High-power Terahertz Radiation. *Journal of Infrared, Millimeter, and Terahertz Waves* **2012,** *33* (7), 695-714.
48. Unger, H.-G., Circular Waveguide Taper of Improved Design. *Bell System Technical Journal* **1958,** *37* (4), 899-912.
49. Tang, C. C. H., Optimization of Waveguide Tapers Capable of Multimode Propagation. *IRE Transactions on Microwave Theory and Techniques* **1961,** *9* (5), 442-452.
50. Doane, J. L., Parabolic tapers for overmoded waveguides. *International Journal of Infrared and Millimeter Waves* **1984,** *5* (5), 737-751.
51. Schaub, S. C.; Shapiro, M. A.; Temkin, R. J., Simple Expressions for the Design of Linear Tapers in Overmoded Corrugated Waveguides. *J Infrared Millim Terahertz Waves* **2016,** *37* (1), 100-110.
52. Albert, B. J.; Pahng, S. H.; Alaniva, N.; Sesti, E. L.; Rand, P. W.; Saliba, E. P.; Scott, F. J.; Choi, E. J.; Barnes, A. B., Instrumentation for cryogenic magic angle spinning dynamic nuclear polarization using 90L of liquid nitrogen per day. *Journal of Magnetic Resonance* **2017,** *283* (Supplement C), 71-78.
53. Barnes, A. B.; Markhasin, E.; Daviso, E.; Michaelis, V. K.; Nanni, E. A.; Jawla, S. K.; Mena, E. L.; DeRocher, R.; Thakkar, A.; Woskov, P. P.; Herzfeld, J.; Temkin, R. J.; Griffin, R. G., Dynamic nuclear polarization at 700 MHz/460 GHz. *J Magn Reson* **2012,** *224*, 1-7.
54. Wind, R. A.; Anthonio, F. E.; Duijvestijn, M. J.; Smidt, J.; Trommel, J.; de Vette, G. M. C., Experimental setup for enhanced 13C NMR spectroscopy in solids using dynamic nuclear polarization. *Journal of Magnetic Resonance (1969)* **1983,** *52* (3), 424-434.

55. Wind, R. A.; Hall, R. A.; Jurkiewicz, A.; Lock, H.; Maciel, G. E., 2 Novel DNP-NMR Probes. *Journal of Magnetic Resonance, Series A* **1994,** *110* (1), 33-37.
56. Chaudhari, S. R.; Berruyer, P.; Gajan, D.; Reiter, C.; Engelke, F.; Silverio, D. L.; Copéret, C.; Lelli, M.; Lesage, A.; Emsley, L., Dynamic nuclear polarization at 40 kHz magic angle spinning. *Physical Chemistry Chemical Physics* **2016,** *18* (15), 10616-10622.
57. Berruyer, P.; Bjorgvinsdottir, S.; Bertarello, A.; Stevanato, G.; Rao, Y.; Ganesan, K.; Gilles, C.; Ouari, O.; Lelli, M.; Reiter, C.; Engelke, F.; Emsley, L., Dynamic Nuclear Polarization Enhancement of 200 at 21.15 T Enabled by 65 kHz Magic Angle Spinning. *Journal of Physical Chemistry Letters* **2020,** *11* (19), 8386-8391.
58. Barnes, A. B.; Mak-Jurkauskas, M. L.; Matsuki, Y.; Bajaj, V. S.; van der Wel, P. C. A.; DeRocher, R.; Bryant, J.; Sirigiri, J. R.; Temkin, R. J.; Lugtenburg, J.; Herzfeld, J.; Griffin, R. G., Cryogenic sample exchange NMR probe for magic angle spinning dynamic nuclear polarization. *Journal of Magnetic Resonance* **2009,** *198* (2), 261-270.
59. Scott, F. J.; Alaniva, N.; Golota, N. C.; Sesti, E. L.; Saliba, E. P.; Price, L. E.; Albert, B. J.; Chen, P.; O'Connor, R. D.; Barnes, A. B., A versatile custom cryostat for dynamic nuclear polarization supports multiple cryogenic magic angle spinning transmission line probes. *Journal of Magnetic Resonance* **2018,** *297*, 23-32.
60. van der Wel, P. C. A., New applications of solid-state NMR in structural biology. *Emerg Top Life Sci* **2018,** *2* (1), 57-67.
61. Opella, S. J.; Marassi, F. M., Applications of NMR to membrane proteins. *Arch Biochem Biophys* **2017,** *628*, 92-101.
62. Ladizhansky, V., Applications of solid-state NMR to membrane proteins. *Biochimica et Biophysica Acta (BBA) - Proteins and Proteomics* **2017,** *1865* (11, Part B), 1577-1586.
63. Zhao, W.; Fernando, L. D.; Kirui, A.; Deligey, F.; Wang, T., Solid-state NMR of plant and fungal cell walls: A critical review. *Solid State Nuclear Magnetic Resonance* **2020,** *107*, 101660.
64. Wang, S.; Hong, Y.-L.; Yuan, S.; Chen, W.; Zhou, W.; Li, Z.; Wang, K.; Min, X.; Konishi, T.; Miyoshi, T., Chain Trajectory, Chain Packing, and Molecular Dynamics of Semicrystalline Polymers as Studied by Solid-State NMR. *Polymers* **2018,** *10* (7).
65. Brunner, E.; Rauche, M., Solid-state NMR spectroscopy: an advancing tool to analyse the structure and properties of metal–organic frameworks. *Chemical Science* **2020,** *11* (17), 4297-4304.
66. Casabianca, L. B., Solid-state nuclear magnetic resonance studies of nanoparticles. *Solid State Nuclear Magnetic Resonance* **2020,** *107*, 101664.
67. Franssen, W. M. J.; Kentgens, A. P. M., Solid–state NMR of hybrid halide perovskites. *Solid State Nuclear Magnetic Resonance* **2019,** *100*, 36-44.
68. Andrew, E. R.; Bradbury, A.; Eades, R. G., Nuclear Magnetic Resonance Spectra from a Crystal rotated at High Speed. *Nature* **1958,** *182* (4650), 1659-1659.
69. Lowe, I. J., Free Induction Decays of Rotating Solids. *Physical Review Letters* **1959,** *2* (7), 285-287.
70. Hing, A. W.; Vega, S.; Schaefer, J., Transferred-echo double-resonance NMR. *Journal of Magnetic Resonance (1969)* **1992,** *96* (1), 205-209.
71. Bennett, A. E.; Rienstra, C. M., Homonuclear radio frequency-driven recoupling in rotating solids. *Journal of Chemical Physics* **1998,** *108* (22), 9463.

72. Chen, P.; Albert, B. J.; Gao, C.; Alaniva, N.; Price, L. E.; Scott, F. J.; Saliba, E. P.; Sesti, E. L.; Judge, P. T.; Fisher, E. W.; Barnes, A. B., Magic angle spinning spheres. *Science Advances* **2018,** *4* (9), eaau1540.
73. Gao, C.; Judge, P. T.; Sesti, E. L.; Price, L. E.; Alaniva, N.; Saliba, E. P.; Albert, B. J.; Soper, N. J.; Chen, P.-H.; Barnes, A. B., Four millimeter spherical rotors spinning at 28 kHz with double-saddle coils for cross polarization NMR. *Journal of Magnetic Resonance* **2019,** *303*, 1-6.
74. Kelz, J. I.; Kelly, J. E.; Martin, R. W., 3D-printed dissolvable inserts for efficient and customizable fabrication of NMR transceiver coils. *Journal of Magnetic Resonance* **2019,** *305*, 89-92.
75. Xie, J.; You, X.; Huang, Y.; Ni, Z.; Wang, X.; Li, X.; Yang, C.; Zhang, D.; Chen, H.; Sun, H.; Chen, Z., 3D-printed integrative probeheads for magnetic resonance. *Nature Communications* **2020,** *11* (1), 5793.
76. Lederle, F.; Meyer, F.; Kaldun, C.; Namyslo, J. C.; Hübner, E. G., Sonogashira coupling in 3D-printed NMR cuvettes: synthesis and properties of arylnaphthylalkynes. *New Journal of Chemistry* **2017,** *41* (5), 1925-1932.
77. Reese, M.; George, C.; Yang, C.; Jawla, S.; Grün, J. T.; Schwalbe, H.; Redfield, C.; Temkin, R. J.; Griffin, R. G., Modular, triple-resonance, transmission line DNP MAS probe for 500 MHz/330 GHz. *Journal of Magnetic Resonance* **2019,** *307*, 106573.
78. Takegoshi, K.; Nakamura, S.; Terao, T., 13C–1H dipolar-assisted rotational resonance in magic-angle spinning NMR. *Chemical Physics Letters* **2001,** *344* (5), 631-637.
79. Michaelis, V. K.; Keeler, E. G.; Ong, T.-C.; Craigen, K. N.; Penzel, S.; Wren, J. E. C.; Kroeker, S.; Griffin, R. G., Structural Insights into Bound Water in Crystalline Amino Acids: Experimental and Theoretical 17O NMR. *The Journal of Physical Chemistry B* **2015,** *119* (25), 8024-8036.
80. Keeler, E. G.; Michaelis, V. K.; Griffin, R. G., 17O NMR Investigation of Water Structure and Dynamics. *The Journal of Physical Chemistry B* **2016,** *120* (32), 7851-7858.
81. Colvin, M. T.; Silvers, R.; Frohm, B.; Su, Y. C.; Linse, S.; Griffin, R. G., High Resolution Structural Characterization of A beta(42) Amyloid Fibrils by Magic Angle Spinning NMR. *Journal of the American Chemical Society* **2015,** *137* (23), 7509-7518.
82. Colvin, M. T.; Silvers, R.; Ni, Q. Z.; Can, T. V.; Sergeyev, I.; Rosay, M.; Donovan, K. J.; Michael, B.; Wall, J.; Linse, S.; Griffin, R. G., Atomic Resolution Structure of Monomorphic A beta(42) Amyloid Fibrils. *Journal of the American Chemical Society* **2016,** *138* (30), 9663-9674.
83. Goedert, M., Alpha-synuclein and neurodegenerative diseases. *Nature Reviews Neuroscience* **2001,** *2* (7), 492-501.
84. Lashuel, H. A.; Overk, C. R.; Oueslati, A.; Masliah, E., The many faces of α-synuclein: from structure and toxicity to therapeutic target. *Nature Reviews Neuroscience* **2013,** *14* (1), 38-48.
85. Debelouchina, G. T.; Platt, G. W.; Bayro, M. J.; Radford, S. E.; Griffin, R. G., Intermolecular Alignment in beta(2)-Microglobulin Amyloid Fibrils. *Journal of the American Chemical Society* **2010,** *132* (48), 17077-17079.
86. Scarpioni, R.; Ricardi, M.; Albertazzi, V.; De Amicis, S.; Rastelli, F.; Zerbini, L., Dialysis-related amyloidosis: challenges and solutions. *Int J Nephrol Renovasc Dis* **2016,** *9*, 319-328.
87. Iadanza, M. G.; Silvers, R.; Boardman, J.; Smith, H. I.; Karamanos, T. K.; Debelouchina, G. T.; Su, Y.; Griffin, R. G.; Ranson, N. A.; Radford, S. E., The structure of a β2-microglobulin

fibril suggests a molecular basis for its amyloid polymorphism. *Nature Communications* **2018,** *9* (1), 4517.
88. Tycko, R., Amyloid polymorphism: structural basis and neurobiological relevance. *Neuron* **2015,** *86* (3), 632-645.
89. Nelson, R.; Sawaya, M. R.; Balbirnie, M.; Madsen, A. Ø.; Riekel, C.; Grothe, R.; Eisenberg, D., Structure of the cross-beta spine of amyloid-like fibrils. *Nature* **2005,** *435* (7043), 773-778.
90. van der Wel, P. C. A.; Lewandowski, J. R.; Griffin, R. G., Solid-State NMR Study of Amyloid Nanocrystals and Fibrils Formed by the Peptide GNNQQNY from Yeast Prion Protein Sup35p. *Journal of the American Chemical Society* **2007,** *129* (16), 5117-5130.
91. van der Wel, P. C. A.; Lewandowski, J. R.; Griffin, R. G., Structural Characterization of GNNQQNY Amyloid Fibrils by Magic Angle Spinning NMR. *Biochemistry* **2010,** *49* (44), 9457-9469.
92. Lewandowski, J. R.; van der Wel, P. C. A.; Rigney, M.; Grigorieff, N.; Griffin, R. G., Structural Complexity of a Composite Amyloid Fibril. *Journal of the American Chemical Society* **2011,** *133* (37), 14686-14698.
93. van der Wel, P. C. A.; Hu, K. N.; Lewandowski, J.; Griffin, R. G., Dynamic nuclear polarization of amyloidogenic peptide nanocrystals: GNNQQNY, a core segment of the yeast prion protein Sup35p. *Journal of the American Chemical Society* **2006,** *128* (33), 10840-10846.
94. Debelouchina, G. T.; Bayro, M. J.; van der Wel, P. C. A.; Caporini, M. A.; Barnes, A. B.; Rosay, M.; Maas, W. E.; Griffin, R. G., Dynamic nuclear polarization-enhanced solid-state NMR spectroscopy of GNNQQNY nanocrystals and amyloid fibrils. *Physical Chemistry Chemical Physics* **2010,** *12* (22), 5911-5919.
95. Achmuller, C.; Kaar, W.; Ahrer, K.; Wechner, P.; Hahn, R.; Werther, F.; Schmidinger, H.; Cserjan-Puschmann, M.; Clementschitsch, F.; Striedner, G.; Bayer, K.; Jungbauer, A.; Auer, B., Npro fusion technology to produce proteins with authentic N termini in E. coli. *Nat Meth* **2007,** *4* (12), 1037-1043.
96. Goda, N.; Matsuo, N.; Tenno, T.; Ishino, S.; Ishino, Y.; Fukuchi, S.; Ota, M.; Hiroaki, H., An optimized N(pro)-based method for the expression and purification of intrinsically disordered proteins for an NMR study. *Intrinsically Disord Proteins* **2015,** *3* (1), e1011004-e1011004.
97. Seyfried, M. S.; Lauber, B. S.; Luedtke, N. W., Multiple-Turnover Isotopic Labeling of Fmoc- and Boc-Protected Amino Acids with Oxygen Isotopes. *Organic Letters* **2010,** *12* (1), 104-106.
98. Jaroniec, C. P.; Filip, C.; Griffin, R. G., 3D TEDOR NMR Experiments for the Simultaneous Measurement of Multiple Carbon−Nitrogen Distances in Uniformly 13C,15N-Labeled Solids. *Journal of the American Chemical Society* **2002,** *124* (36), 10728-10742.
99. Jaroniec, C. P.; Tounge, B. A.; Herzfeld, J.; Griffin, R. G., Frequency Selective Heteronuclear Dipolar Recoupling in Rotating Solids: Accurate 13C−15N Distance Measurements in Uniformly 13C,15N-labeled Peptides. *Journal of the American Chemical Society* **2001,** *123* (15), 3507-3519.
100. Ramachandran, R.; Ladizhansky, V.; Bajaj, V. S.; Griffin, R. G., 13C−13C Rotational Resonance Width Distance Measurements in Uniformly 13C-Labeled Peptides. *Journal of the American Chemical Society* **2003,** *125* (50), 15623-15629.

101. Keeler, E. G.; Michaelis, V. K.; Colvin, M. T.; Hung, I.; Gor'kov, P. L.; Cross, T. A.; Gan, Z.; Griffin, R. G., 17O MAS NMR Correlation Spectroscopy at High Magnetic Fields. *Journal of the American Chemical Society* **2017,** *139* (49), 17953-17963.
102. Martins, V.; Xu, J.; Hung, I.; Gan, Z.; Gervais, C.; Bonhomme, C.; Huang, Y., 17O solid-state NMR at ultrahigh magnetic field of 35.2 T: Resolution of inequivalent oxygen sites in different phases of MOF MIL-53(Al). *Magnetic Resonance in Chemistry* **2020,** *n/a* (n/a).
103. Ashbrook, S. E.; Duer, M. J., Structural information from quadrupolar nuclei in solid state NMR. *Concepts in Magnetic Resonance Part A* **2006,** *28A* (3), 183-248.
104. Ashbrook, S. E.; Sneddon, S., New Methods and Applications in Solid-State NMR Spectroscopy of Quadrupolar Nuclei. *Journal of the American Chemical Society* **2014,** *136* (44), 15440-15456.
105. Xue, K.; Sarkar, R.; Motz, C.; Asami, S.; Decker, V.; Wegner, S.; Tosner, Z.; Reif, B., Magic-Angle Spinning Frequencies beyond 300 kHz Are Necessary To Yield Maximum Sensitivity in Selectively Methyl Protonated Protein Samples in Solid-State NMR. *J. Phys. Chem. C* **2018,** *122* (28), 16437-16442.
106. Chevelkov, V.; van Rossum, B. J.; Castellani, F.; Rehbein, K.; Diehl, A.; Hohwy, M.; Steuernagel, S.; Engelke, F.; Oschkinat, H.; Reif, B., H Detection in MAS Solid-State NMR Spectroscopy of Biomacromolecules Employing Pulsed Field Gradients for Residual Solvent Suppression. *Journal of the American Chemical Society* **2003,** *125* (26), 7788-7789.
107. Mispelter, J. l.; Lupu, M.; Briguet, A., *NMR probeheads for biophysical and biomedical experiments: theoretical principles & practical guidelines*. Second edition ed.; Imperial College Press: London, 2015; p 735.
108. Markhasin, E.; Hu, J.; Su, Y.; Herzfeld, J.; Griffin, R. G., Efficient, balanced, transmission line RF circuits by back propagation of common impedance nodes. *J Magn Reson* **2013,** *231*, 32-8.
109. Qian, C.; Brey, W. W., Impedance matching with an adjustable segmented transmission line. *Journal of Magnetic Resonance* **2009,** *199* (1), 104-110.
110. Robbins, R. F.; Ludtke, P. R., Review of static seals for cryogenic systems. *Journal of Spacecraft and Rockets* **1964,** *1* (3), 253-259.
111. Lovinger, D.; Hallock, R., Temperature dependence of helium diffusion through common epoxies. *Journal of Physics Conference Series* **2012,** *400*, 2006.
112. Lim, C. C., Indium seals for low-temperature and moderate-pressure applications. *Rev. Sci. Instrum.* **1986,** *57* (1), 108-114.
113. Stewart, M. D.; Koutroulakis, G.; Kalechofsky, N.; Mitrović, V. F., A Reusable, Low-profile, Cryogenic Wire Seal. *Cryogenics (Guildf)* **2010,** *50* (1), 50-51.
114. Ishii, Y.; Wickramasinghe, A.; Matsuda, I.; Endo, Y.; Ishii, Y.; Nishiyama, Y.; Nemoto, T.; Kamihara, T., Progress in proton-detected solid-state NMR (SSNMR): Super-fast 2D SSNMR collection for nano-mole-scale proteins. *Journal of Magnetic Resonance* **2018,** *286*, 99-109.
115. Bouleau, E.; Saint-Bonnet, P.; Mentink-Vigier, F.; Takahashi, H.; Jacquot, J. F.; Bardet, M.; Aussenac, F.; Purea, A.; Engelke, F.; Hediger, S.; Lee, D.; De Paëpe, G., Pushing NMR sensitivity limits using dynamic nuclear polarization with closed-loop cryogenic helium sample spinning. *Chemical Science* **2015,** *6* (12), 6806-6812.
116. Purea, A.; Reiter, C.; Dimitriadis, A. I.; de Rijk, E.; Aussenac, F.; Sergeyev, I.; Rosay, M.; Engelke, F., Improved waveguide coupling for 1.3 mm MAS DNP probes at 263 GHz. *Journal of Magnetic Resonance* **2019,** *302*, 43-49.

117. Wilhelm, D.; Purea, A.; Engelke, F., Fluid flow dynamics in MAS systems. *Journal of Magnetic Resonance* **2015,** *257*, 51-63.
118. Jensen, J. E.; Tuttle, W. A.; Stewart, R. B.; Brechna, H.; Prodell, A. G., Selected Cryogenic Data Notebook. Energy, D. o., Ed. 1980.
119. Matsuki, Y.; Kobayashi, T.; Fukazawa, J.; Perras, F. A.; Pruski, M.; Fujiwara, T., Efficiency analysis of helium-cooled MAS DNP: case studies of surface-modified nanoparticles and homogeneous small-molecule solutions. *Physical Chemistry Chemical Physics* **2021,** *23* (8), 4919-4926.
120. Kelly, A. E.; Ou, H. D.; Withers, R.; Dötsch, V., Low-Conductivity Buffers for High-Sensitivity NMR Measurements. *Journal of the American Chemical Society* **2002,** *124* (40), 12013-12019.
121. Hassan, A.; Quinn, C. M.; Struppe, J.; Sergeyev, I. V.; Zhang, C.; Guo, C.; Runge, B.; Theint, T.; Dao, H. H.; Jaroniec, C. P.; Berbon, M.; Lends, A.; Habenstein, B.; Loquet, A.; Kuemmerle, R.; Perrone, B.; Gronenborn, A. M.; Polenova, T., Sensitivity boosts by the CPMAS CryoProbe for challenging biological assemblies. *Journal of Magnetic Resonance* **2020,** *311*, 106680.
122. Kovacs, H.; Moskau, D.; Spraul, M., Cryogenically cooled probes—a leap in NMR technology. *Progress in Nuclear Magnetic Resonance Spectroscopy* **2005,** *46* (2), 131-155.
123. Samoson, A., H-MAS. *Journal of Magnetic Resonance* **2019,** *306*, 167-172.
124. Penzel, S.; Oss, A.; Org, M. L.; Samoson, A.; Bockmann, A.; Ernst, M.; Meier, B. H., Spinning faster: protein NMR at MAS frequencies up to 126kHz. *Journal of Biomolecular Nmr* **2019,** *73* (1-2), 19-29.
125. Thurber, K. R.; Tycko, R., Biomolecular solid state NMR with magic-angle spinning at 25K. *Journal of Magnetic Resonance* **2008,** *195* (2), 179-186.
126. Thurber, K. R.; Potapov, A.; Yau, W.-M.; Tycko, R., Solid state nuclear magnetic resonance with magic-angle spinning and dynamic nuclear polarization below 25K. *Journal of Magnetic Resonance* **2013,** *226*, 100-106.
127. Thurber, K.; Tycko, R., Low-temperature dynamic nuclear polarization with helium-cooled samples and nitrogen-driven magic-angle spinning. *Journal of magnetic resonance (San Diego, Calif. : 1997)* **2016,** *264*, 99-106.
128. Judge, P. T.; Sesti, E. L.; Saliba, E. P.; Alaniva, N.; Halbritter, T.; Sigurdsson, S. T.; Barnes, A. B., Sensitivity analysis of magic angle spinning dynamic nuclear polarization below 6 K. *Journal of Magnetic Resonance* **2019,** *305*, 51-57.
129. Sesti, E. L.; Saliba, E. P.; Alaniva, N.; Barnes, A. B., Electron decoupling with cross polarization and dynamic nuclear polarization below 6 K. *Journal of Magnetic Resonance* **2018,** *295*, 1-5.
130. Alaniva, N.; Saliba, E. P.; Sesti, E. L.; Judge, P. T.; Barnes, A. B., Electron Decoupling with Chirped Microwave Pulses for Rapid Signal Acquisition and Electron Saturation Recovery. *Angewandte Chemie International Edition* **2019,** *58* (22), 7259-7262.
131. Bouleau, E.; Lee, D.; Saint-Bonnet, P.; Hediger, S.; De Paëpe, G., Ultra-Low Temperature Nuclear Magnetic Resonance. *IOP Conference Series: Materials Science and Engineering* **2017,** *171*, 012142.
132. Lee, D.; Bouleau, E.; Saint-Bonnet, P.; Hediger, S.; De Paëpe, G., Ultra-low temperature MAS-DNP. *Journal of Magnetic Resonance* **2016,** *264*, 116-124.

133. Matsuki, Y.; Ueda, K.; Idehara, T.; Ikeda, R.; Ogawa, I.; Nakamura, S.; Toda, M.; Anai, T.; Fujiwara, T., Helium-cooling and -spinning dynamic nuclear polarization for sensitivity-enhanced solid-state NMR at 14T and 30K. *Journal of Magnetic Resonance* **2012,** *225*, 1-9.
134. Matsuki, Y.; Idehara, T.; Fukazawa, J.; Fujiwara, T., Advanced instrumentation for DNP-enhanced MAS NMR for higher magnetic fields and lower temperatures. *Journal of Magnetic Resonance* **2016,** *264* (Supplement C), 107-115.
135. Albert, B. J.; Pahng, S. H.; Alaniva, N.; Sesti, E. L.; Rand, P. W.; Saliba, E. P.; Scott, F. J.; Choi, E. J.; Barnes, A. B., Instrumentation for cryogenic magic angle spinning dynamic nuclear polarization using 90L of liquid nitrogen per day. *Journal of magnetic resonance (San Diego, Calif. : 1997)* **2017,** *283*, 71-78.
136. Penzel, S.; Oss, A.; Org, M.-L.; Samoson, A.; Böckmann, A.; Ernst, M.; Meier, B. H., Spinning faster: protein NMR at MAS frequencies up to 126 kHz. *Journal of biomolecular NMR* **2019,** *73* (1-2), 19-29.
137. Lin, Y.-L.; Cheng, Y.-S.; Ho, C.-I.; Guo, Z.-H.; Huang, S.-J.; Org, M.-L.; Oss, A.; Samoson, A.; Chan, J. C. C., Preparation of fibril nuclei of beta-amyloid peptides in reverse micelles. *Chemical Communications* **2018,** *54* (74), 10459-10462.
138. Lecoq, L.; Schledorn, M.; Wang, S.; Smith-Penzel, S.; Malär, A. A.; Callon, M.; Nassal, M.; Meier, B. H.; Böckmann, A., 100 kHz MAS Proton-Detected NMR Spectroscopy of Hepatitis B Virus Capsids. *Frontiers in Molecular Biosciences* **2019,** *6*, 58.
139. Chaudhari, S. R.; Wisser, D.; Pinon, A. C.; Berruyer, P.; Gajan, D.; Tordo, P.; Ouari, O.; Reiter, C.; Engelke, F.; Coperet, C.; Lelli, M.; Lesage, A.; Emsley, L., Dynamic Nuclear Polarization Efficiency Increased by Very Fast Magic Angle Spinning. *Journal of the American Chemical Society* **2017,** *139* (31), 10609-10612.
140. Sussmann, R. S.; Brandon, J. R.; Scarsbrook, G. A.; Sweeney, C. G.; Valentine, T. J.; Whitehead, A. J.; Wort, C. J. H., Properties of bulk polycrystalline CVD diamond. *Diamond and Related Materials* **1994,** *3* (4), 303-312.
141. Klein, C. A.; Cardinale, G. F., Young's modulus and Poisson's ratio of CVD diamond. *Diamond and Related Materials* **1993,** *2* (5), 918-923.
142. Wort, C. J. H.; Sweeney, C. G.; Cooper, M. A.; Scarsbrook, G. A.; Sussmann, R. S., Thermal properties of bulk polycrystalline CVD diamond. *Diamond and Related Materials* **1994,** *3* (9), 1158-1167.
143. Rogalin, V. E.; Kaplunov, I. A.; Kropotov, G. I., Optical Materials for the THz Range. *Optics and Spectroscopy* **2018,** *125* (6), 1053-1064.
144. Kasugai, A.; Sakamoto, K.; Takahashi, K.; Tsuneoka, M.; Kariya, T.; Imai, T.; Braz, O.; Thumm, M.; Brandon, J. R.; Sussman, R. S.; Beale, A.; Ballington, D. C., Chemical vapor deposition diamond window for high-power and long pulse millimeter wave transmission. *Rev. Sci. Instrum.* **1998,** *69* (5), 2160-2165.
145. Heidinger, R.; Dammertz, G.; Meier, A.; Thumm, M. K., CVD diamond windows studied with low- and high-power millimeter waves. *IEEE Transactions on Plasma Science* **2002,** *30* (3), 800-807.
146. Subbiah, R.; Littleton, J. E., *Rotor and Structural Dynamics of Turbomachinery: A Practical Guide for Engineers and Scientists*. 1st ed. 2018 ed.; Springer International Publishing : Imprint: Springer: Cham, 2018; p 1.
147. Genta, G., *Dynamics of rotating systems*. Springer: New York, 2005; p 658.
148. Endo, Y., Hioka, Katsuya, Yamauchi, Kazuo Sample tube and measurement method for solid-state NMR. US8436616B2, 2013.

149. Doty, F. D.; Ellis, P. D., Design of high speed cylindrical NMR sample spinners. *Rev. Sci. Instrum.* **1981,** *52* (12), 1868-1875.
150. Everson, C.; Molian, P., Fabrication of polycrystalline diamond microtool using a Q-switched Nd:YAG laser. *The International Journal of Advanced Manufacturing Technology* **2009,** *45* (5), 521.
151. Sudheer, S. K.; Mahadevan Pillai, V. P.; Nayar, V. U., Processing of Diamond for Integrated Optic Devices Using Q-Switched Nd:YAG Laser at Different Wavelengths. *Fiber and Integrated Optics* **2006,** *25* (1), 59-68.
152. Fabis, P. M., Laser machining of CVD diamond: chemical and structural alteration effects. *Surface and Coatings Technology* **1996,** *82* (3), 320-325.
153. Howe, J. Y. The oxidation of diamond. Alfred University, Alfred, NY, 2001.
154. Khmelnitsky, R. A.; Gippius, A. A., Transformation of diamond to graphite under heat treatment at low pressure. *Phase Transitions* **2014,** *87* (2), 175-192.
155. Paci, J. T.; Minton, T. K.; Schatz, G. C., Hyperthermal Oxidation of Graphite and Diamond. *Accounts of Chemical Research* **2012,** *45* (11), 1973-1981.
156. De Vita, A.; Galli, G.; Canning, A.; Car, R., A microscopic model for surface-induced diamond-to-graphite transitions. *Nature* **1996,** *379* (6565), 523-526.
157. Shpilman, Z.; Gouzman, I.; Grossman, E.; Shen, L.; Minton, T. K.; Paci, J. T.; Schatz, G. C.; Akhvlediani, R.; Hoffman, A., Oxidation and Etching of CVD Diamond by Thermal and Hyperthermal Atomic Oxygen. *The Journal of Physical Chemistry C* **2010,** *114* (44), 18996-19003.
158. Zhang, G. F.; Zhang, B.; Deng, Z. H.; Chen, J. F., An Experimental Study on Laser Cutting Mechanisms of Polycrystalline Diamond Compacts. *CIRP Annals* **2007,** *56* (1), 201-204.
159. Osswald, S.; Yushin, G.; Mochalin, V.; Kucheyev, S. O.; Gogotsi, Y., Control of sp^2/sp^3 Carbon Ratio and Surface Chemistry of Nanodiamond Powders by Selective Oxidation in Air. *Journal of the American Chemical Society* **2006,** *128* (35), 11635-11642.
160. Gloor, S.; Pimenov, S. M.; Obraztsova, E. D.; Lüthy, W.; Weber, H. P., Laser ablation of diamond films in various atmospheres. *Diamond and Related Materials* **1998,** *7* (2), 607-611.
161. Jahns, D.; Kaszemeikat, T.; Mueller, N.; Ashkenasi, D.; Dietrich, R.; Eichler, H. J., Laser Trepanning of Stainless Steel. *Physics Procedia* **2013,** *41*, 630-635.